1-30-96

SANDIA REPORT

SAND96-0105
Unlimited Release
Printed January 1996

RECEIVED
FEB 06 1996
OSTI

Fuel Dispersal in High-Speed Aircraft/Soil Impact Scenarios

Sheldon R. Tieszen, Stephen W. Attaway

Prepared by
Sandia National Laboratories
Albuquerque, New Mexico 87185 and Livermore, California 94550
for the United States Department of Energy
under Contract DE-AC04-94AL85000

Approved for public release; distribution is unlimited.

MASTER

SF2900Q(8-81)

DISTRIBUTION OF THIS DOCUMENT IS UNLIMITED

Dlc

Issued by Sandia National Laboratories, operated for the United States Department of Energy by Sandia Corporation.

Printed in the United States of America. This report has been reproduced directly from the best available copy.

Available to DOE and DOE contractors from
Office of Scientific and Technical Information
PO Box 62
Oak Ridge, TN 37831

Prices available from (615) 576-8401, FTS 626-8401

Available to the public from
National Technical Information Service
US Department of Commerce
5285 Port Royal Rd
Springfield, VA 22161

NTIS price codes
Printed copy: A06
Microfiche copy: A01

SAND96-0105
Unlimited Release
Printed January 1996

Fuel Dispersal in High-Speed Aircraft/Soil Impact Scenarios

Sheldon R. Tieszen & Stephen W. Attaway
Engineering Sciences Center 9100
Sandia National Laboratories
Albuquerque, New Mexico 87185

Abstract

The objective of this study is to determine how the jet fuel contained in aircraft wing tanks disperses on impact with a soft terrain, i.e., soils, at high impact velocities. The approach used in this study is to combine experimental and numerical methods. Tests were conducted with an approximately 1/42 linear-scale mass-model of a 1/4 span section of a C-141 wing impacting a sand/clay mixture. The test results showed that within the uncertainty of the data, the percentage of incident liquid mass remaining in the crater is the same as that qualitatively described in earlier napalm bomb development studies. Namely, the percentage of fuel in the crater ranges from near zero for grazing impacts to 25% - 50% for high angles of impact. To support a weapons system safety assessment (WSSA), the data from the current study have been reduced to correlations. The numerical model used in the current study is a unique coupling of a Smooth Particle Hydrodynamics (SPH) method with the transient dynamics finite element code PRONTO. Qualitatively, the splash, erosion, and soil compression phenomena are all numerically predicted. Quantitatively, the numerical method predicted a smaller crater cross section than was observed in the tests.

DLC

Table of Contents

List of Figures

List of Tables

Acknowledgments

The authors would like to thank Rodney Oliver who assisted in the design and was responsible for the fabrication of the gun, wing section, and test bed diagnostics, and also assisted in acquiring the data for each test. Jeffrey Wemple suggested the unique gun triggering scheme. The authors would also like to thank Jeff Swegle and Adam Slavin for their effort in developing and applying the SPH/PRONTO tool to the current problem. The soil mechanical properties characterization tests were conducted by Tim Byers, Geo-Test, Inc. Portions of this study are to appear in a journal article entitled "Transient, High-Speed, Liquid Impact into Soft Soil," in Computer Modeling and Simulation in Engineering 1:79-106, 1996. This study was sponsored by the Defense Nuclear Agency. The work was conducted at Sandia National Laboratories which is run by Lockheed Martin Corp. for the U. S. Department of Energy under Contract DE-AC04-94AL85000.

Executive Summary

The objective of this study is to determine how the jet fuel contained in aircraft wing tanks disperses on impact with a soft terrain, i.e., soils, at high impact velocity. Impact into soft terrain is expected to differ from hard terrain, i.e., concrete runways, due to the cratering process. The scope of the current study is limited to the high impact velocity regime. The boundary between the intermediate and high impact velocity regimes is defined as the point where the wing completely disintegrates on impact.

The approach used in this study is to combine experimental and numerical methods. The role of the experiments is two fold, 1) to provide data to create a response surface, and 2) to provide data to support numerical model development/validation. The intent is to provide data for a weapons system safety assessment (WSSA) and to validate a numerical model that can be used for further analyses.

Tests were conducted at Sandia National Laboratories (SNL) with an approximately 1/42 linear-scale mass-model of a 1/4 span section of a C-141 wing. The tests were conducted in the Transient Jet Impingement Characterization (TJIC) test apparatus, a specialized 4 cm diameter gas gun that was designed and constructed for this program. One soil type, a sand/clay mixture, was used to represent a generic type of natural soil that may be encountered off a runway or in a field. Two independent variables were evaluated, the impact angle and impact velocity. Eleven tests were conducted, at three impact velocities, 30, 64, and 92 m/s, and three impact angles, 22.5°, 45° and 67.5°. Three dependent variables, important for determining the initial conditions for a pool fire scenario, were measured:1) the area covered by fuel, 2) the amount of fuel in that area, and 3) the location of the fuel relative to the impact line. In addition, measurements were taken to quantify the deformation and erosion (i.e., cratering) of the soil.

The test results showed that within the uncertainty of the data, the percentage of incident liquid mass remaining in the crater is the same as that qualitatively described in earlier napalm bomb development studies. Namely, the percentage of fuel in the crater ranges from near zero for grazing impacts to 25% - 50% for high angles of impact. In general, the craters formed had a breadth on the order of the jet chord, a depth that is a fraction of the jet chord, and volume that is greater than the jet volume by up to about an order of magnitude. The crater dimensions of breadth, depth, and volume, when normalized to the appropriate jet dimensions, exceeded those in the napalm bomb development study by a factor of two to three. This difference can be partially explained by differences in soil characteristics and geometry.

From the data obtained in the current study and comparisons with napalm bomb development data, it is argued that the impact of a C141 would fall within the differences between the normalized data from the current tests and the normalized data from the napalm bomb development tests. To support a weapons system safety assessment (WSSA),

the data from the current study have been reduced to correlations. Correlations have been developed for 1) the crater area covered by fuel, 2) the equivalent fuel-layer thickness, and 3) the location of the fuel relative to the impact line. Unresolved issues are identified in the report including neglecting the effect of the wing structure in the current tests. The current study is the first of its kind to the authors knowledge, linear geometric scaling was *assumed*, and well characterized data for actual wing impacts does not exist. Larger scale test results including limited full scale testing would improve the confidence that the reasonable expectations based on the arguments presented in this report are indeed fulfilled.

Uncertainty estimates for the tests indicate that there are several parameters that can have on the order of a factor of two uncertainty. These include the area coverage, effective liquid layer thickness, the position of the crater relative to the point of impact, and the effect of non-uniform spatial distribution prior to impact and after impact on the ground. Since the duration of a pool fire is directly proportional to the depth of the liquid layer, a factor of about 2 in uncertainty will exist in the duration of the fire. The phenomenology of burning above a fuel-soaked soil surface is not addressed in the current study, but will further contribute to the uncertainty in fire duration.

The numerical model used in the current study is a unique coupling of a Smooth Particle Hydrodynamics (SPH) method with the transient dynamics finite element code PRONTO. The PRONTO/SPH code was compared to the experimental data at the center and edge points of the test matrix. Qualitatively predicted are the splash, erosion, and soil compression phenomena. Quantitatively, the numerical method predicted a smaller crater cross section than was observed in the tests.

Introduction

For the purpose of aircraft-fuel-dispersal modeling, the spectrum of accidents involving aircraft impact with the ground can be divided into three impact-velocity regimes which are defined by three corresponding fuel-tank-damage regimes (Tieszen, 1995). At low impact velocities, structural damage to the wing fuel tanks is insignificant and an insignificant amount of fuel leaks from the fuel tanks. At intermediate impact velocities, structural damage to the wing fuel tanks is significant but insufficient to cause complete structural failure of the fuel tanks. In this regime, fuel will leak from the damaged tank at a rate proportional to the amount of damage to the tank. At high impact velocities, complete structural failure of the wing fuel tanks occurs. In this regime, fuel will splash/disperse upon impact with the ground.

The objective of this study is to determine how the jet fuel contained in wing tanks disperses on impact with soft terrain at high impact velocity. This study complements a previous study on impact into a hard, flat surface, such as a runway (Tieszen, 1995). The previous hard surface study concluded that impact at high velocity into a non-cratering surface would produce atomization of the fuel at all velocities of interest. Further, test results showed that *no liquid pooling occurred* for impact velocities greater than 61 m/s independent of the angle of impact. The effect of the wing structure on the fuel dispersal characteristics in both studies is ignored.

Impact into soft terrain is expected to differ from hard terrain due to the cratering process. From napalm bomb development studies it is clear that some fuel will remain in the impact crater resulting from the impact of a fragmenting fuel tank. Edwards, 1973 attributes the following quote to a Lt. Royer on napalm bomb development tests, "Impact craters 1.5 - 5 feet (0.5 - 1.7 m) deep and 5 to 14 feet (1.7 - 4.3 m) in diameter, restricted flame fuel dissemination and ignition.... Thirty to 50% of the flame fuel from each fire bomb burned in impact craters (for 8 - 100 minutes)..." Edwards, 1973 notes that "There is a high degree of correlation between the vertical component of velocity at impact and the depth and volume of the crater gouged out at impact." Further, for shallow craters, Edwards, 1973, notes that "When fire bombs are released in the skip bomb mode, e.g., at 200 knots (100 m/s) from 100 feet (30 m) in straight and level flight, little if any unburned incendigel is likely to adhere to the sand at the point of impact. Evidently, practically all of the 100 gallons (379 l) of incendigel in the canister is thrown out immediately on impact." From these comments one can expect that the amount of fuel in the crater ranges from near zero for grazing impacts to 30% - 50% for high angles of impact.

The scope of the current study is limited to the high-impact-velocity regime. The boundary between the intermediate and high-impact-velocity regimes is defined as the point where the wing completely disintegrates on impact. The velocity at which this occurs cannot be completely specified with the existing data. Wittlin, 1987, concludes that a distributed-load wing impact (such as striking a low hill or mound with the wing) between 60 and 72 m/sec will devastate wing fuel tanks. For concentrated loads (such as a telephone pole) the velocity at which the wing tanks will be destroyed is even lower, 33 to 41 m/sec, depending on the type of obstacle.

While the term 'high impact velocity regime' is used to distinguish between accidents which involve wing tank fracture but not disintegration, the term should not be confused with hypervelocity impact that occurs in armor penetration applications. Hypervelocity impacts occur typically in the kilometer per second range, or between one and two orders of magnitude higher than the current study. In the hypervelocity impact regime, liquification of the materials occurs and the processes can be considered hydrodynamic, i.e., the strength of the materials can be ignored (See for example, Miller, 1990). In the current study, the crush characteristics of the soil are found to be very important. The velocity range of interest of the current study is closer to that of soil erosion studies which are typically on the order of a few meters per second, or about one order of magnitude less than the current study. (See for example, Bubenzer and Jones, 1971, Park, et.al., 1982, and Riezebos and Epema, 1985.) In soil erosion studies, it is found that both drop momentum and drop kinetic energy are important parameters, although the correlation coefficient between erosion and drop kinetic energy is better than that between erosion and drop momentum (Riezebos and Epema, 1985). These results differ from the current study which finds a very high correlation between jet momentum and crater volume. To the authors' knowledge the current study is the first of its kind in the velocity range of relevance to high speed aircraft impact.

The approach used in this study is to combine experimental and numerical methods. The role of the experiments is two fold, 1) to provide data to create a response surface, and 2) to provide data to support model development/validation. The intent is to provide data for a weapons system safety assessment (WSSA) and to validate a numerical model that can be used for further analyses. The numerical method used in the present study is a unique coupling of smooth particle hydrodynamics (SPH) with a finite element tool PRONTO. The tool has general applicability beyond the current study and its development is outside the scope of this report. However, the assessment of the tool using the data acquired is presented following the presentation of the experimental technique and results.

Experimental Test Plan

Like the previous experimental study (Tieszen, 1995), the confinement provided by the wing structure is ignored in the current test series. The current tests were conducted with liquid impinging directly onto the ground. The justification for ignoring the confinement of the wing is based on observation of the completeness of the disintegration of wing structures at velocities in the high impact regime (von Riesemann, et al, 1989, and Moya, 1994). This assumption is appropriate at the highest velocities of interest to the current study and becomes progressively worse as the impact velocity decreases. However, it is necessary to make this assumption because fragmentation is a very complex process which depends not only material properties but also on fabrication details such as rivet locations etc. It is very challenging, if even possible, to reproduce details such as rivets at small scale for test purposes. Even for numerical modeling, the necessity of resolving these details makes it very expensive to simulate.The current experimental study is conducted at 1/42 linear scale compared to 1/9 linear scale in the previous tests. The primary purpose for the reduction in scale is to reduce costs associated with testing.

Figure 1 defines the geometric parameters of interest for the test series. The fuel within the wing tanks of a C-141 transport is approximated as a transient, finite-length, two-dimensional, planar jet which impacts the ground at an arbitrary angle and velocity. This approximation is equivalent to assuming that the C-141 fuel tanks are a single rectangular fuel tank. The thickness of the rectangular tank, T, is assumed to be proportional to the thickness of the wing. The length of the tank, C, is assumed to be proportional the chord of the wing, and the span of the tank, S, is assumed to be proportional to the span of the wing. The idealized jet, therefore, will have a thickness, T, a length, C, and a width, S. For the tests, water was used as a simulant for JP-4/JP-8. The use of water greatly simplifies environmental and safety issues that would have to be addressed if actual jet fuels were used.

Two independent variables were evaluated, the impact angle and impact velocity. Each variable was tested at three levels. For impact angle, the levels studied were 22.5°, 45.0°, and 67.5° from the horizontal (i.e., α in Figure 1). Implicit in the geometry shown in Figure 1 is that the pitch, yaw, and roll angles of the aircraft are all zero, i.e., the aircraft is flying straight into the ground at the impact angle. For the impact velocities, the levels studied were 30, 64, and 92 m/s. A single repeat test was conducted at 45.0° and 64 m/s. For the series of tests in this report, one soil type was used to represent a generic type of natural soil that may be encountered off of a runway or in a field. The important characteristics of the soil are its density, moisture content, material composition, and grain size.

Three important parameters were measured to determine the initial conditions for a pool fire scenario:1) the area covered by fuel, 2) the amount of fuel in that area, and 3) the location of that area relative to the impact line. In addition, measurements were taken of

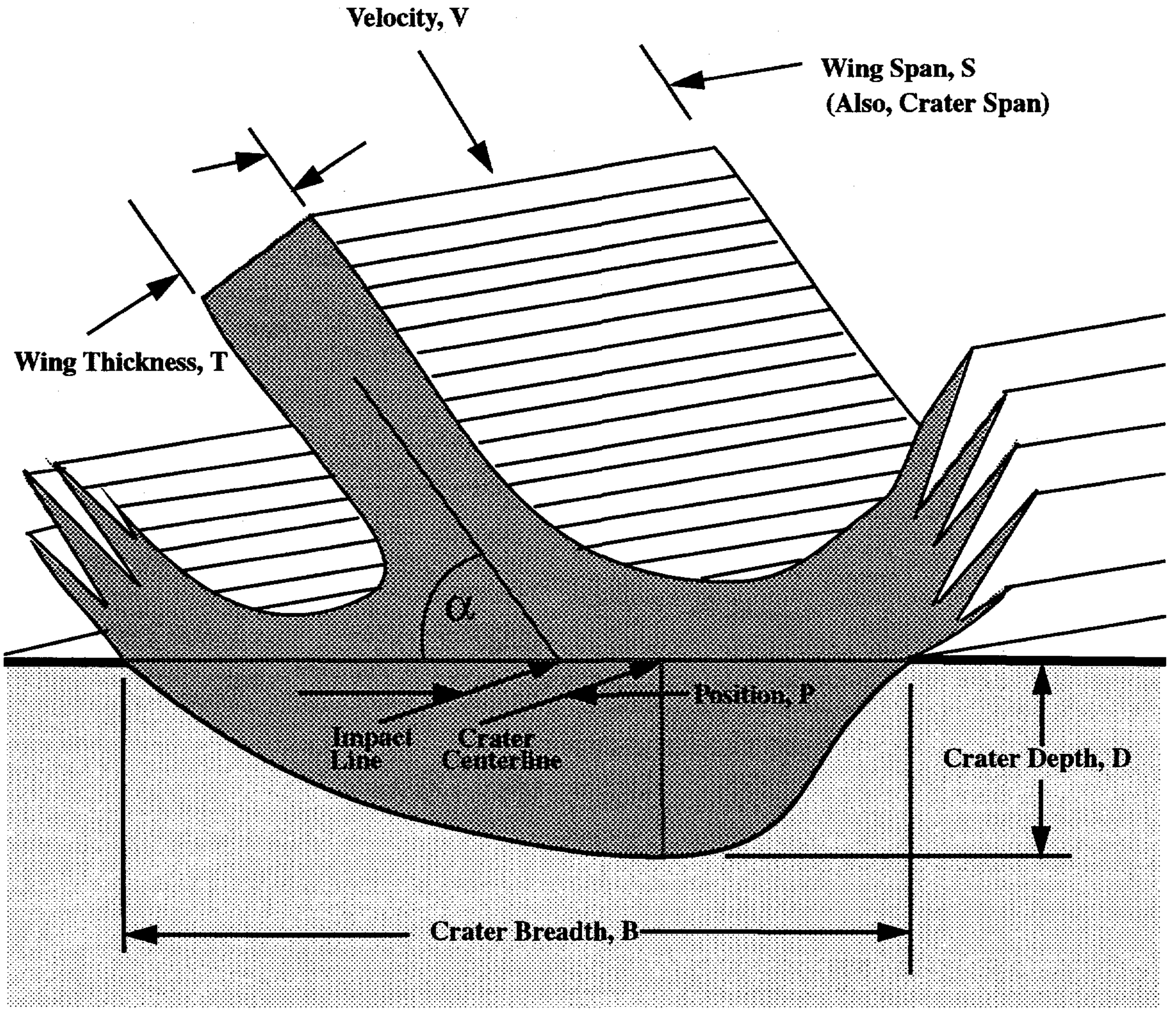

FIGURE 1. Test Parameter Definitions. Not shown is the length of the jet, C, which corresponds to the wing chord.

soil deformation and erosion (i.e., cratering) for comparison with numerical calculations using the smooth particle hydrodynamics, SPH, technique. Normal and high-speed video were used to visualize the splashing of liquid from the soil target.

Test Apparatus/Procedures

The discussion of the test apparatus will be divided into five sections, 1) the test facility, 2) the wing section, 3) the soil characteristics, 4) the diagnostics, and 5) procedures.

Test Facility

The tests were conducted at Sandia National Laboratories, Site 9920, Albuquerque, New Mexico. The tests were conducted in the Transient Jet Impingement Characterization (TJIC) test apparatus, Figure 2. The apparatus is a specialized 4 cm diameter gas gun. The

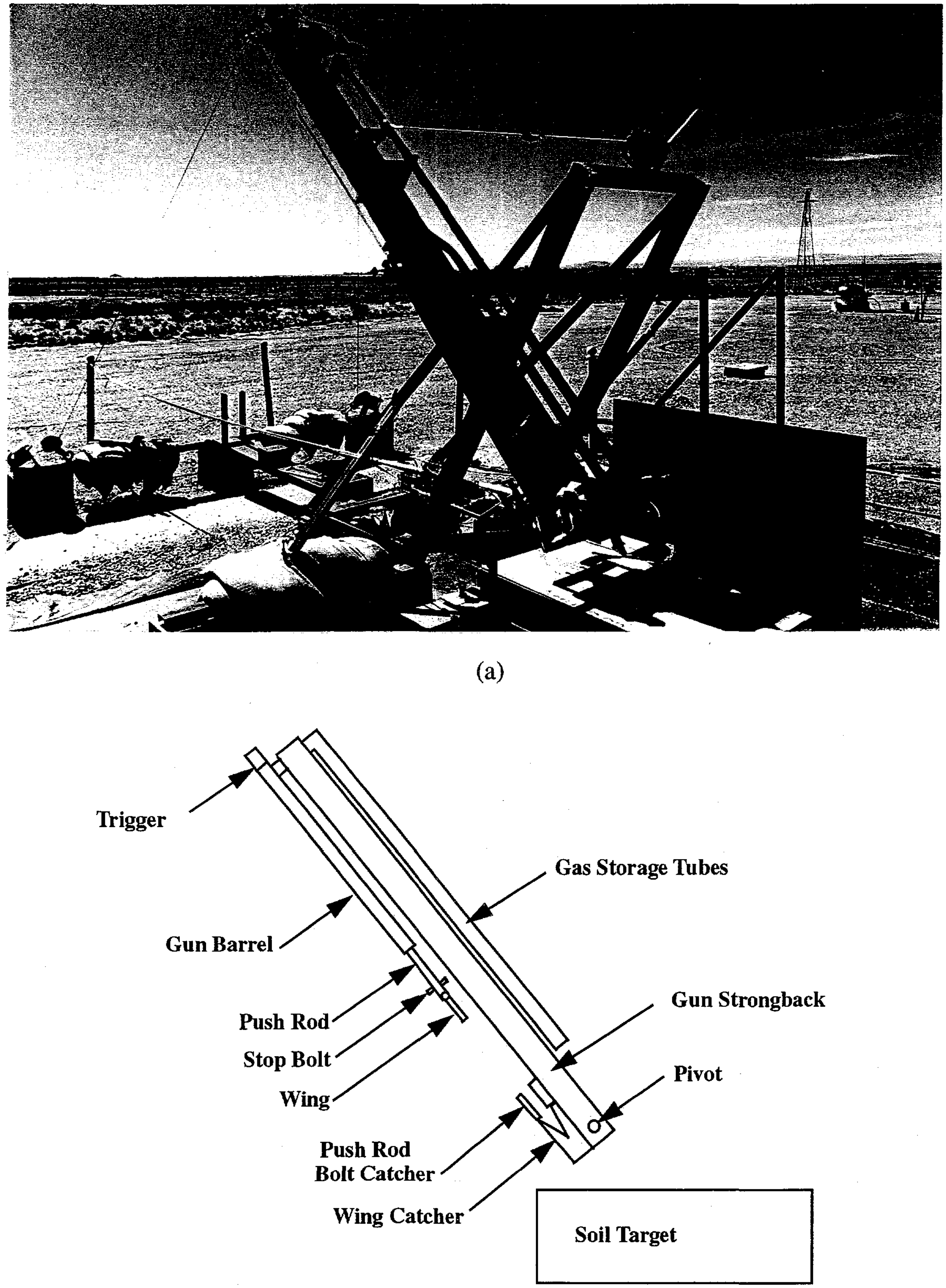

(a)

(b)

FIGURE 2. Transient Jet Impact Facility. (a) Photograph of the Facility (b) Schematic.

gas gun was designed and built for this program. The gun barrel is 1.6 m long, made from 5 cm OD stainless steel tubing. and has an operating pressure of 115 atm; thereby, yielding a work potential of about 20 kJ. This is sufficient to accelerate 2.2 kg of mass to about 100 m/s with an average acceleration of 350 g's.

The design philosophy employed in developing the gas gun was driven by programmatic needs, experience with previous intermediate-scale dispersal tests (Tieszen, 1995), and previous gas-gun experience by the author. Gas guns provide a cost effective means of accelerating projectiles to the velocity range of interest. The impact velocity is highly controllable by varying the pressure in the gas reservoir. The angle of impact is controlled by mounting the gun on a pivot as has been previously done on a large 15 cm diameter gun used for penetrator work at Sandia.

The TJIC design is unique in that the projectiles flown are not cylindrical, but wing shaped (i.e., wide, thin rectangles). This necessitates a flight path external to the cylindrical barrel. To accommodate this, the gun barrel is placed back from the pivot point a length equal to the barrel length, as shown in Figure 2. The wing is mounted external to the gun barrel and is propelled by a pusher plate/rod assembly inside the gun barrel. The wing flies between guide channels until the assembly is stopped at the pivot point and the liquid is allowed to fly freely and impact the soil target. A winch assembly is used to raise or lower the gun about the pivot point, thereby setting the angle of impact for each test.

Compressed nitrogen is used as the working fluid in the gun. It is supplied from one or two 5.7 standard cubic meters (200 standard cubic feet) gas bottles through a 6 mm diameter gas manifold. The compressed air is bled into a 7.2 m long reservoir of 4 cm ID tubing. All connections between this reservoir and the gun barrel are 4 cm ID, minimizing the pressure drop on firing the gun. The gun is fired from the reservoir pressure only; the supply bottles are isolated prior to firing. As the gun is fired, the compressed gas in the reservoirs accelerates the mass toward the soil target. The volume at full expansion of the gas is 1.2 times the initial reservoir volume. For an isentropic expansion, the final gun pressure is estimated to be about 78% of the initial pressure. Since the driving pressure remains fairly constant, the acceleration does also.

Figure 3 shows a photograph of the pusher plate/rod assembly. Starting from the left in Figure 3a, the trigger release mechanism (female part), the pusher plate (with male trigger pin), crushable honeycomb, rod centering plate, push rod (with stop bolt) and wing assembly are shown. While most gas guns use a double diaphragm mechanism for a trigger, the TJIC gun uses a mechanical release designed around a Swagelock quick-disconnect. The advantage of this approach is that pressure-rated burst diaphragms of various ranges are not required and not consumed in each test. The trigger holds back the pusher plate which contains an O-ring seal that prevents gas leaking into the barrel before and during flight. For a test, pressure is applied to the back side of the pusher plate from the pressure storage reservoirs. The male portion of the trigger is attached to the pusher plate. The female portion of the trigger remains attached to the gun barrel. Prior to release, the only portion of the assembly under load is the trigger and pusher plate. This allows lower-

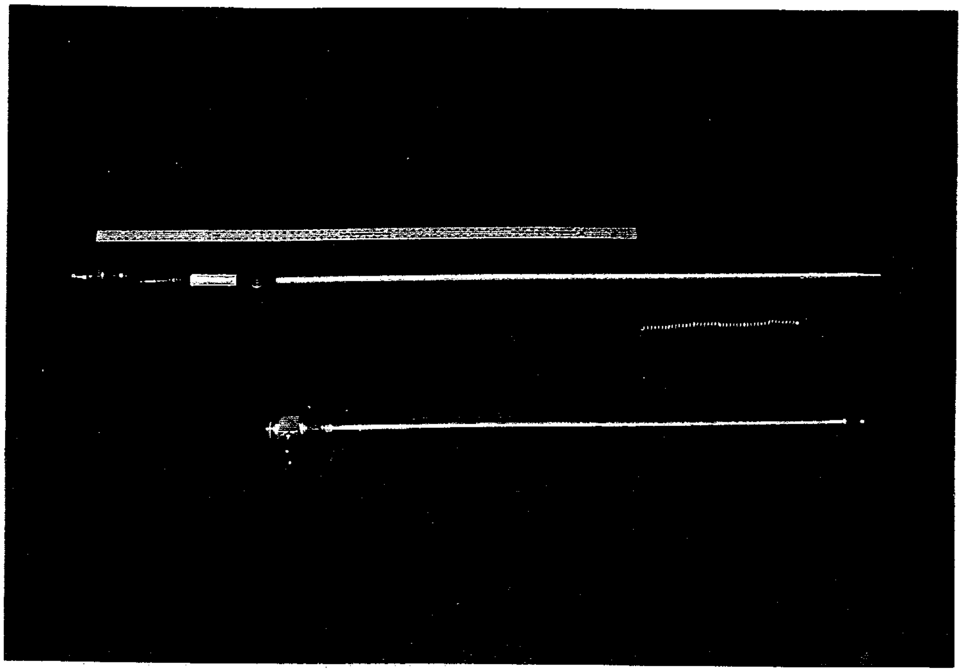

(a)

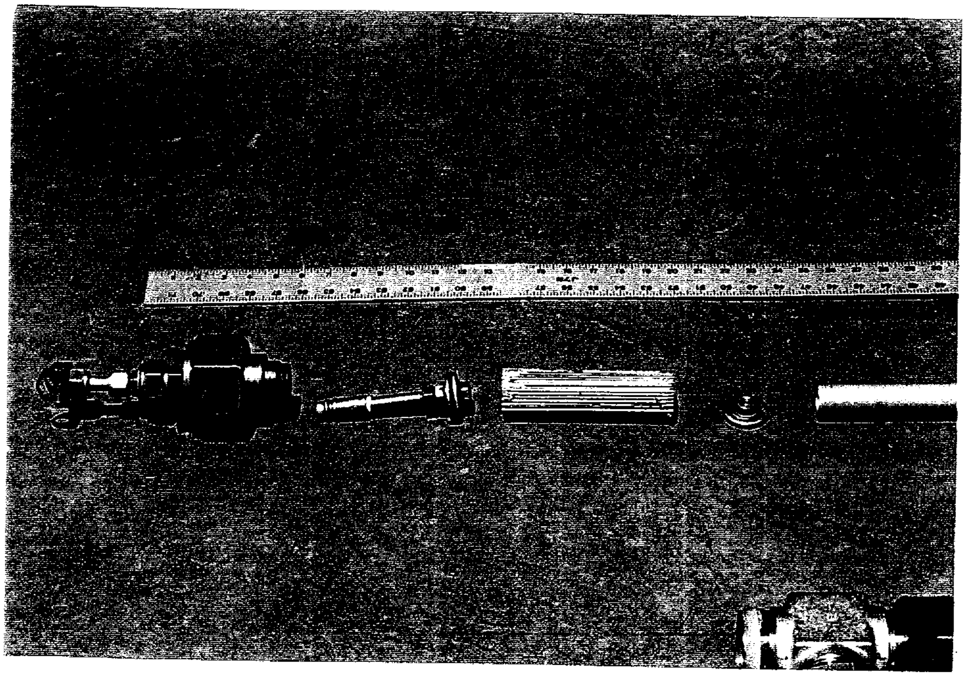

(b)

FIGURE 3. Internal Components of TJIC gun. (a) Overview showing internal components, wing assembly, stopping springs and gun barrel. Note: Ruler is 1.83m long. (b) Close-up of trigger, pusher plate, honeycomb block, and rod centering plate.

strength/lighter-weight components to be used between the pusher plate and the wing, allowing for a higher velocity.

Between the pusher plate and the rod centering plate is a 15 cm long block of 5052 aluminum alloy honeycomb, 3.18 mm cell size, with an apparent density of 98 kg/m^3. This 4 cm diameter honeycomb block became necessary because the inertial mass of the wing section at the far end of the push rod caused the push rod to collapse (buckle) at the pusher plate end on initial release. The crushable honeycomb broadened the pressure pulse to the push rod by partially collapsing on release. The honeycomb abuts the push-rod centering plate. This plate keeps the end of the rod centered in the gun barrel and helps prevent column buckling of the push rod. The push rod itself is a 2.5 cm OD diameter aluminum tube with a 2 mm thick wall. The push rod has a long slot at the wing end that is the thickness of the wing. The wing is mounted onto the push rod by positioning it in this slot.

For each test conducted, the total mass being accelerated was about 2.2 kg. The liquid mass for each test was 362 g +/-36 g, or 17% of the total accelerated mass. The remaining mass was minimized to 1) allow the highest possible speed and 2) minimize the mass which had to be stopped to prevent it from impacting the soil target and disturbing the test results. The combination of mass minimization coupled with high strength requirements to withstand the high acceleration and deceleration loads resulted in a complex design challenge.

In order to prevent the non-liquid mass from impacting the soil target, the TJIC facility has three separate stopping mechanisms. Separate stopping mechanisms were used for 1) the pusher plate + the honeycomb block + centering plate assembly which contained 12% of the accelerated mass, 2) the push rod + stopping bolt assembly which contained 42% of the accelerated mass, and 3) the wing assembly (without liquid) which contained 29% of the accelerated mass. Significant design iteration was required to stop the non-liquid mass without affecting the propagation of the liquid jet onto the soil target.

The pusher plate assembly (pusher plate + the honeycomb block + centering plate) was stopped nondestructively using springs at the end of the gun barrel. This method of stopping the pusher plate allowed 1) repeated use of the pusher plate (at a cost savings since a moderate amount of machining was required to produce this part) and 2) the pusher plate to seal the end of the gun at the end of its travel. This second item prevented gas, used in accelerating the plate, from blowing out the end of the gun and interfering with the atomizing liquid jet. The springs occupied the lower 0.5 m of the gun barrel with inner diameters a fraction of a millimeter larger than the push rod (allowing it free travel through the springs), and outer diameters a fraction of a millimeter smaller than the inner gun barrel diameter. The end of the gun barrel had an end fitting just large enough to allow free passage of the push rod but retained the springs. The fully-accelerated pusher plate assembly compressed the springs between it and the end of the gun barrel. Gas pressure in the gun was vented post-test from vent valves located away from the soil target.

The push rod + stopping bolt assembly was destructively stopped. Relatively little machining was required in this assembly and its relatively large mass required that its kinetic energy be absorbed through material deformation. This was accomplished by placing top and bottom stripping plates 0.14 m from the gun pivot along the flight path as shown in Figure 2b. The plates are placed so as to not impede the flight of the wing assembly but catch the stopping bolt in the push rod, which is located just behind the wing assembly. The stopping bolt passes vertically through the center of the push rod (perpendicular to the horizontal wing) and impacts the top and bottom stripping plates. When the bolt stops, the push rod continues along the flight path, tearing the aluminum rod along its axis. The resulting gross metal deformation dissipates the kinetic energy of push rod in a short (<0.1 m) distance. In order to ensure that the tearing occurs along the axis of the push rod (and thereby preventing deflection to one side and failure to stop the push rod), 6 mm holes were drilled in the aluminum rod along the axis behind the 12 mm stop bolt.

The wing assembly was also destructively stopped. Due to the strength requirements to withstand the acceleration loads, its mass was found to be too large to stop elastically. Elastic deceleration would have been preferred as a moderated amount of assembly was required in the preparation of each wing. The wing assembly was stopped by capturing the wing strong back (see next section) in capture wedges as shown in Figure 2b. The capture wedges were placed on each side of the wing, beyond the wingspan so as to capture the wing-strongback, but not interfere with the continued flight of the water to the soil target. As the wing assembly was propelled down the flight path, it remained in the push-rod slot until the progress of the push rod was impeded by the stop bolt. The wing continued in free flight until encountering the capture wedges about 5 cm further down the flight path. The capture wedges were filled with 0.10-0.15 m of balsa wood which crushed as the wing strong-back tubing became entrapped in the capture wedges.

The crushable balsa wood in the capture wedges spread out the loading over the duration of its crush. This pulse spreading caused several effects. First, the diaphragm on the front of the wing would break on first impact with the balsa allowing the liquid to continue its flight. The deformation loads during the balsa crushup are relatively weaker, therefore, allowing time for the liquid to clear the wing before large deformations occurred in the wing structure. The crush-up of the balsa also prevented high-peak-pressure shock loads which tended to fail the wing strong-back. After the liquid cleared the wing, large deformation of the wing strongback and wing box resulted in kinetic energy dissipation, allowing the wing to be captured, and therefore, preventing its impact with the soil target.

The Wing Section

The wing section was designed to represent the fuel in the wing tanks of a C141 transport. For these tests it is assumed that the fuel tanks of the C141 form a rectangular box with dimensions proportional to the thickness x chord x span of the actual C141 wing tanks. The baseline proportions for fully loaded wing tanks have been estimated as 0.49 m : 3.52 m : 51.0 m for thickness:chord:span (Tieszen, 1995). In terms of the thickness of the jet, T, in Figure 1,the ratio's for a fully fueled C141 are T:7.2T:104T. Or, in terms of the wing chord, C, (not shown on Figure 1), the ratio's are 0.139C:C:14.4C for thickness:chord:span, respectively. The results from this study will be nondimensionalized by the wing chord, C.

Due to limited space between the pivot supports, testing of a wing at its full wingspan would reduce the scale of the model wing unnecessarily. Therefore, only a 1/4 span section of the wing was tested. The actual as built dimensions of the model wings are 0.015 m : 0.084 m : 0.305 m. In terms of the wing chord, *C*, the ratio's are 0.179*C*:*C*:3.6*C*. Therefore, to obtain the results for a full wing span, the model results must be multiplied by 4 in the span direction.

The thickness to chord ratio for the actual model wing is somewhat larger than for the C141, 0.179 vs. 0.139, respectively. This is due to the sensitivity to errors in construction technique at small scale. If the wing thickness were 3 mm smaller, the ratio would be correct. It is not expected that the results will be overly sensitive to this construction error.

The overall linear scale factor is 1:42 between the model and the C141. For reference, the linear scale factor for the previous test series at intermediate scale for impact onto a flat non-cratering surface was 1:9.1 (Tieszen, 1995). Roughly, the current small-scale model has linear dimensions 1/5 those of the intermediate scale model.

Design of the wing section proved to be a significant design challenge and resulted in several design iterations. Figure 4a shows the construction used for the low 30 m/s impact velocity tests. This design evolved from numerous attempts to produce a wing that was stiff enough to withstand the acceleration, yet be sufficiently deformable that it could be stopped through large-scale deformation of the wing. In designs for which the materials ripped or fractured, the wing assembly usually ended up in the soil target. Since its mass is many times greater than the mass of a true wing structure at 1/42 scale, it usually dug a very deep hole. Since the acceleration distance is short, the wing assembly is subject to 30 - 40 times the acceleration loads that an actual wing would be subject to in flight, hence, its relatively high weight.

The wing box in Figure 4a is made of 0.36 mm thick 304 stainless steel sheet stock that has been folded and spot welded along the sides. Three 0.58 mm thick, 75mm long, 304 stainless steel, vertical support struts are spot welded equidistant along the span at the front the wingbox to prevent leading edge separation/collapse. The back edges of the wing box are strengthened with 0.58 mm thick, 7 cm long 304 stainless steel triangular gussets that are spot welded along the edge and the back.

A 0.46 m long, 13 mm OD tube is inserted through the rear of the box as a strong-back. The tube has a 1.7 mm wall thickness and is made of 4130 Cond-N carbon steel. The ends of the strong-back are finished with 1.6 mm thick, 51 mm diameter washers and Swagelock end-fittings that have been welded in place. In addition, a 9.5 mm diameter, 3.8 cm long hardwood dowel is press fit into each end of the strong-back. The purpose of these end fittings is to allow the wing catcher to trap the passing wing assembly and for the strong-back to survive the deceleration loads. To spread the acceleration induced inertial loads, a 20 cm long aluminum tube with a 13 mm OD and a 1.6 mm wall thickness was taped parallel with the strong back between it and the pushrod. This tube was intended as a flexible element for the starting shock in the same manner that the crushable honeycomb block was used in the pusher plate assembly. The initial acceleration is very high and the

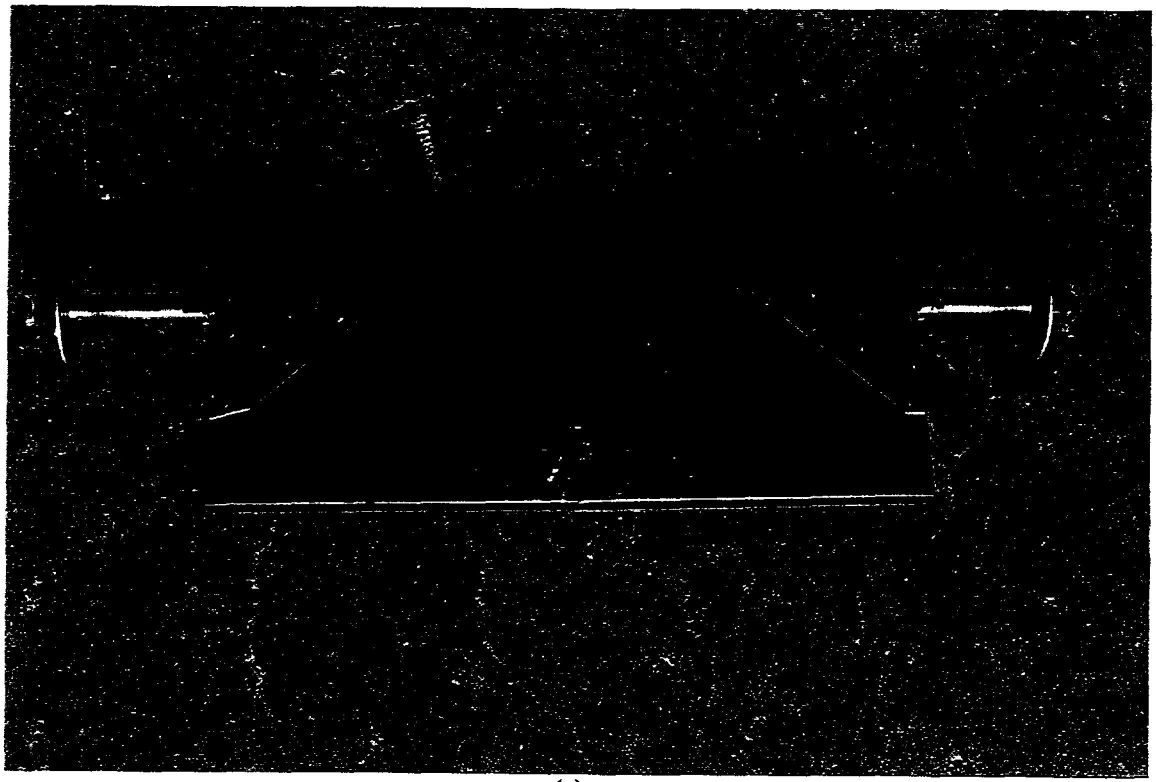

(a)

(b)

FIGURE 4. Photographs of Wing Assembly. (a) Wind design for the 30 m/s tests. (b) Wing design for the 64 m/s and 93 m/s tests.

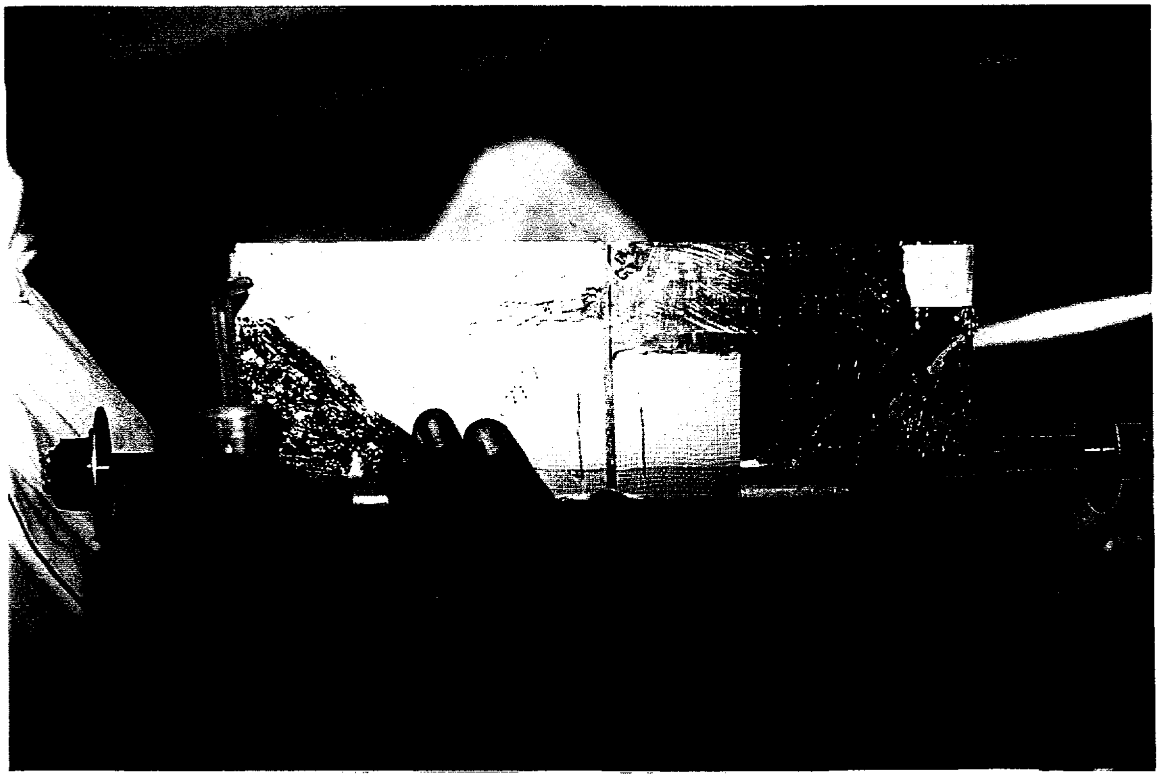

FIGURE 5. Wing Assembly Being Loaded with Liquid.

inertial loads on the wing are also high. The aluminum tube spreads loads from the push rod to the wing more uniformly to prevent the push rod from driving through the wing strong-back, i.e., bowing the wing, on start-up.

In spite of the effort to spread the loads, tests conducted with the wing configuration in Figure 4a resulted in a nonuniform distribution of the liquid jet for velocities above 30 m/s. Figure 4b shows the wing design that was used for the 64 m/s and 92 m/s tests. A second strongback consisting of a 13 mm OD 316 stainless steel tube with a 1.7 mm thick wall is bent at about 9° and welded at the ends to the straight strongback. Crushable balsawood is wedged between the strongbacks. This arrangement proved sufficient to withstand the initial acceleration loads for the higher velocity tests.

The wing assembly is finished by sealing all the spot welds and seams with silicone rubber sealant. Prior to being loaded with water, the leading edge of the wing is sealed with 13 μm (0.5 mil) thick polyethylene plastic. This material tears easily under the impact loads caused by the wing assembly impacting the balsa wood in the wing catcher, thereby allowing the water to continue its flight to the soil target. The polyethylene is held in place with epoxy along the external edges of the wing box. The wing is filled with water from a small hole near the leading edge as shown in Figure 5 . After the wing has been filled with water, the hole is sealed with 3M Scotchseal Synthetic Putty #1167.

Soil Characterization

Soil characteristics in the U. S. vary widely from sands to clays, from coarse gravels to fine silts, from saturated to bone dry. Since soil types can very greatly, we selected a representative soil that could be 'engineered' to have consistent properties. Given below are the characteristics of the soil chosen and the rationale for its choice.

The soil used for the target soil in these experiments is a sand/clay mixture. A mixture was chosen because sands and clays tend to have very different mechanical response characteristics. Sands do not have the adhesion of clays. As a result, sands typically have less volume compressibility than clays, because the sand grains can naturally settle into a near optimum compression. Further, sands do not have the shear strength of clays, because shear strength is related to the adhesion. Both volume compressibility and shear strength are important mechanical properties of a soil that determine the impact response. A mixture represents a compromise between the mechanical properties of both soil types. The soil used was a naturally occurring Albuquerque, NM soil and was well mixed.

The grain size of the soil is given in Table 1. The maximum particle size in the soil is 2.4 mm. At full scale, i.e., 42 times larger, this would represent a 10 cm (4 inch) rock. The particle size is important relative to the scale of the jet. The liquid jet has a thickness of 15 mm (ignoring drag induced spreading). This corresponds to about 6 times the maximum particle size. This is somewhat coarse but not unreasonable representation of a continuous soil.

Table 1. Soil Sieve Analysis

Sieve Size No.	Maximum Particle Size (μm)	Percent of Mass Passing Through Sieve at Given Size
8	2360	100
40	425	73
80	180	59
200	75	28

As determined by a Proctor test (ASTM D1557), the maximum dry density to which the selected soil can be compacted is 1920 kg/m^3 (120 lb/ft^3). The Proctor test was performed on soil samples by Geo-Test, Inc. The density of undisturbed soils around Albuquerque, New Mexico is typically 80% of maximum compaction (T. Byers, personal communication, July 7,1994). Uncompressed, loose fill soil is typically 50% of maximum compaction. For all tests conducted in this study, the dry density of the soil was 1390 kg/m^3 (86.6 lb/ft^3) +/- 50 kg/m^3 (3 lb/ft^3). This density is 72% of the maximum compaction density. This density was chosen because it was easily obtainable in the experiments. While it is somewhat less dense than the typical undisturbed soil densities for the Albuquerque area, it is probably denser than a fleshly plowed field.

For all tests conducted in this study the moisture mass is 6.3% +/- 0.6% of the soil mass. From the Proctor test, the moisture that results in maximum compaction is 10.3%. Typical moisture contents in the semi-arid Albuquerque area run 3-6% for soils down to a couple of meters (Byers, 1994). Below that depth, the soils become slightly drier until the water table has been reached. A moisture content of 6.3% therefore is between dry and wet soils.

The soil density and moisture content were measured for each test after the impact. The density was measured with a 15 cm diameter sand cone test (ASTM D1556-90). One cone measurement station was taken in the test bed typically 0.5 m downstream of the impact crater. The soil that was removed for the cone test was weighed wet, dried in an oven, and then reweighed to determine the moisture content.

Strength properties of the soil were measured to provide validation data for the SPH technique. In order to determine the soil yield stress as a function of pressure (constants a_0, a_1, and a_2 described in the Numerical Simulation Section), three triaxial test were preformed at 0.068 MPa, 0.137 MPa, and 0.344 MPa (10, 20 and 50 psi.) The triaxial test applied a confining pressure to the soil by wrapping a soil sample in a thin rubber bladder and hydrostatically loading the enclosed sample with oil pumped to a given pressure. A uniaxial strain was then applied to the sample with the crush force and displacement measured.

The results for each of these test are shown in Figure 6. As can be seen from these plots, the soil behavior is near perfectly plastic, with a slight softening effect after the yield. While the yield is not as well defined as is found in metals, one can identify a yield pressure. Figure 7 plots the yield stress as a function of confining pressure (mean stress). Here only a linear relation was observed, so the a_2 term was dropped. Testing at higher pressures would be required to determine a more complex relation between the yield strength and pressure.

The pressure at a given volume strain was measured by uniaxially crushing a cylindrical soil sample confined in a steel cylinder. The soil sample initial density was approximately equal to the soil target density. The results of the crush test are shown in Figure 8.The soil initially crushed under very small pressures, resulting in almost constant crush pressure as the space between the soil grains consolidated. When unloaded from a crushed state, the soil experienced very little elastic rebound. (i.e. once the soil was crushed it stayed crushed.) At high crush strains the soil ‘locked up’ and further loading did not result in more crushing. After ‘lock up’ the soil behaved as an elastic body storing energy like a spring as it deformed.

For each fuel dispersal test in the current study, the soil was placed in a steel box, 0.20 m deep, 0.61 m wide, and, 1.22 m long. The box was positioned so that the impact line occurred about 1/3 of the box length forward of the rear edge of the box, independent of the angle of impact. The size and shape of the box was made to be as large as possible to minimize finite length, i.e., edge, effects on the results and yet be small enough to be practical. For the tests conducted, no craters were formed that reached to any edge of the box.

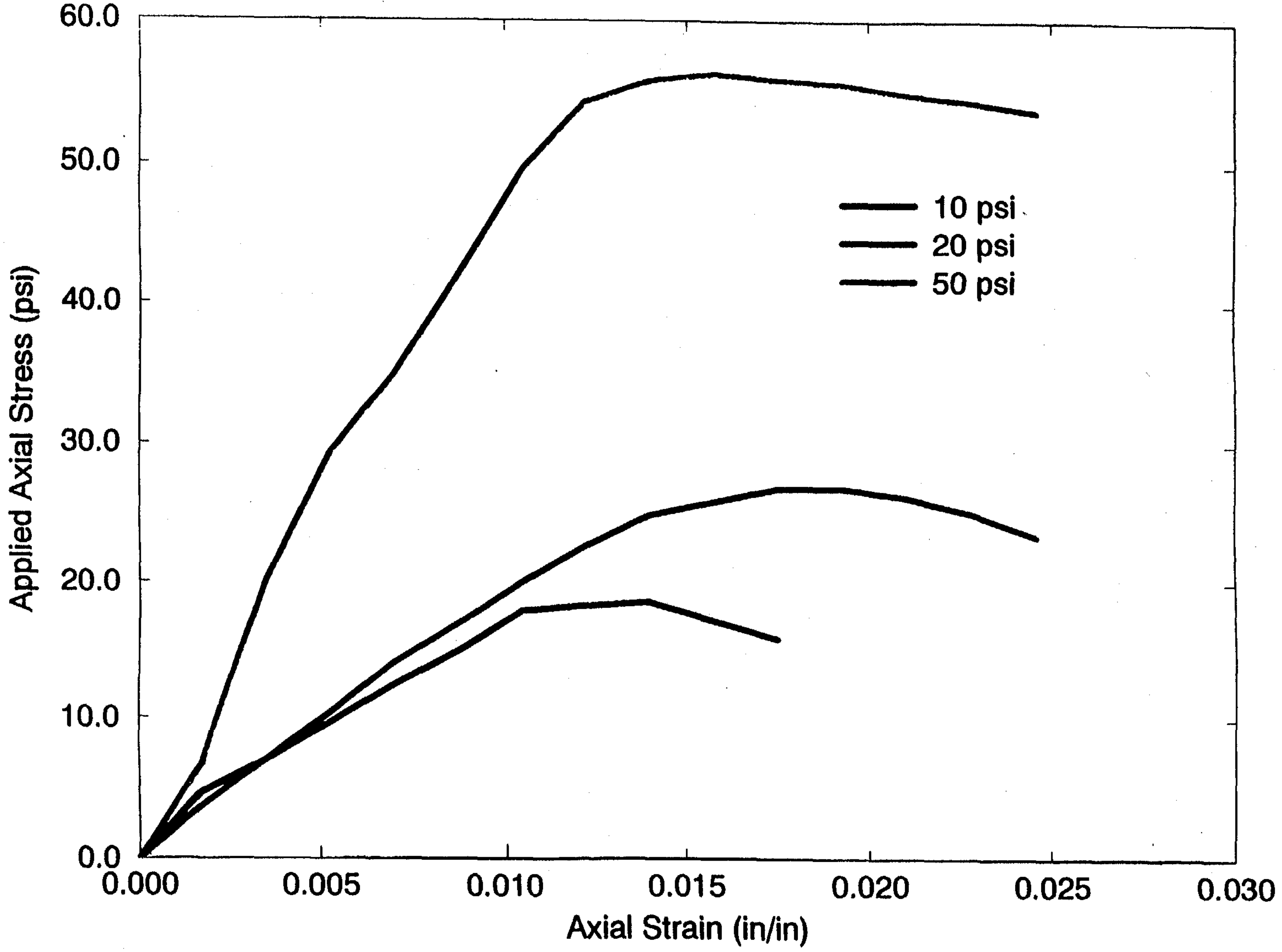

FIGURE 6. Triaxial Soil Response for 10, 20, and 50 psi Chamber Pressure. Applied axial stress versus axial strain.

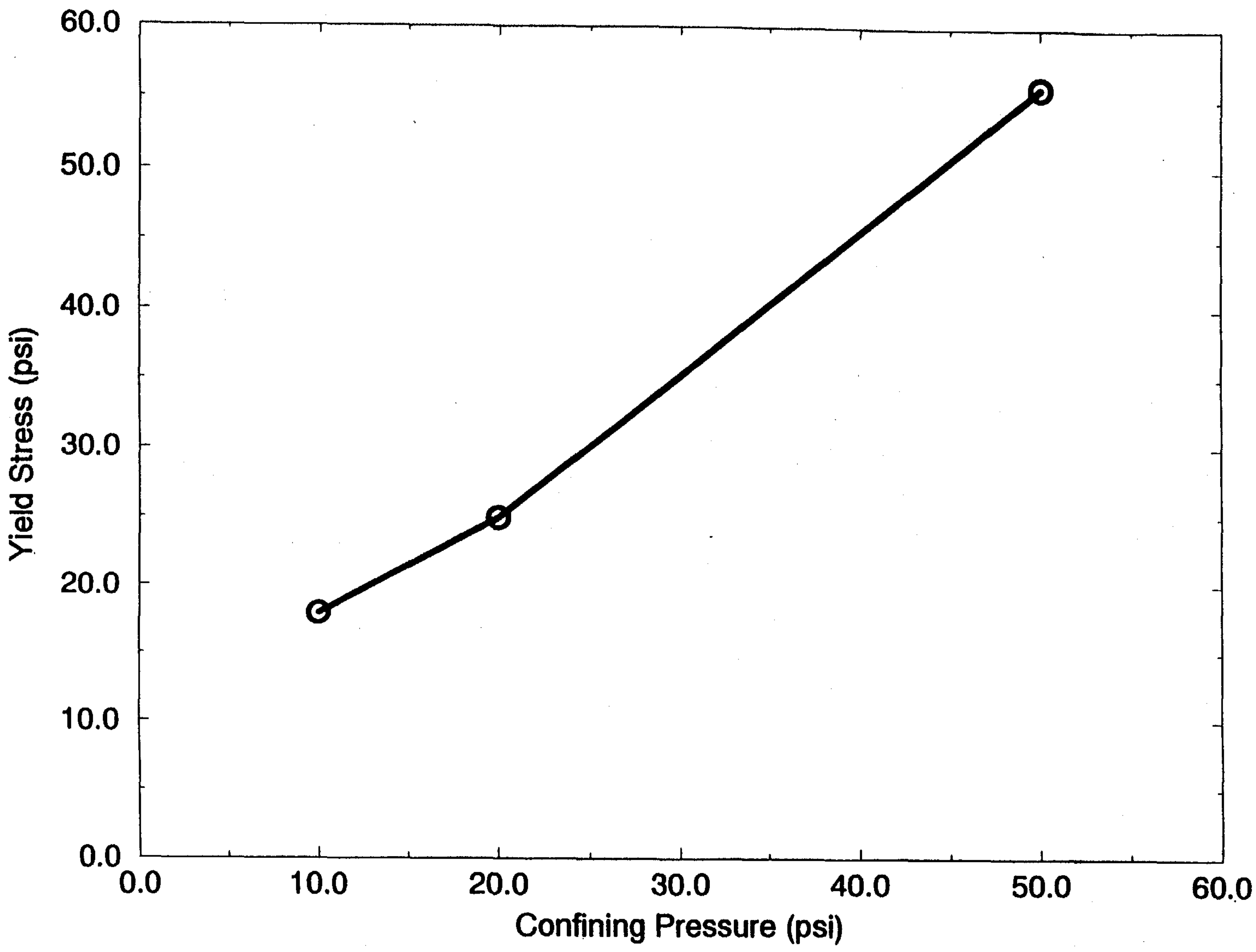

FIGURE 7. Yield Stress as a Function of Confining Pressure for Soil.

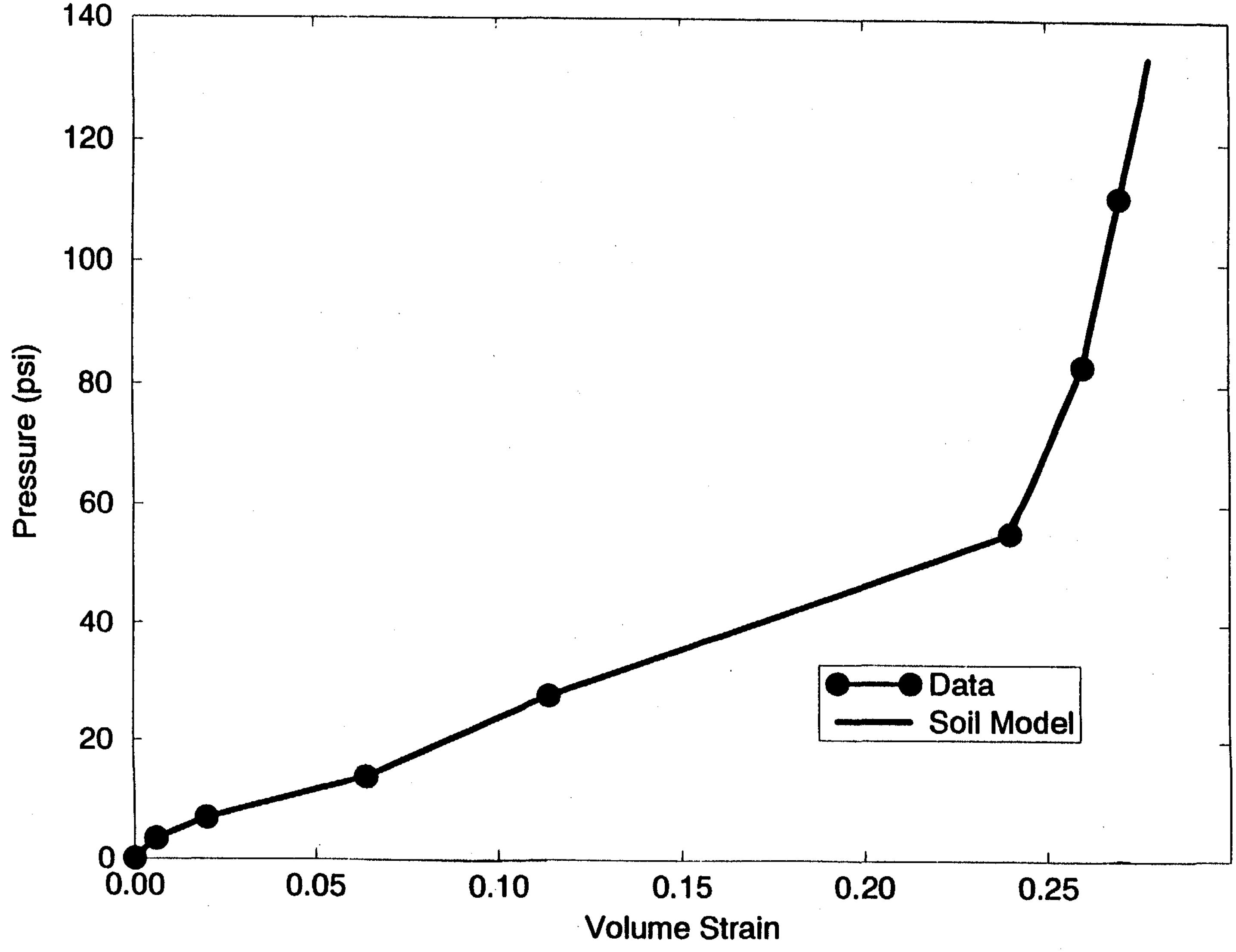

FIGURE 8. Pressure as a Function of Volume Strain for Soil.

Stringent preparation procedures were required to achieve uniform and reproducible soil densities and moisture contents. The soil for each test took approximately 5 hours to prepare and place in the box. First, the soil was sieved with the No.8 screen to assure that no particles larger than 2.4 mm was placed in the box. A sample of the sieved soil was then weighed, dried, and reweighed to determine the natural moisture content. The amount of water to be added to the soil to bring it up to its test moisture was calculated. The soil was then placed in the box in layers, or "lifts". This is standard civil engineering procedure for producing uniform soil densities. Sixteen lifts were used, approximately 1.25 cm (1/2 inch) thick after compaction. For each lift, the soil was hand distributed into the box as shown in Figures 9a and 9b. A 6.7 kg, 10.2 cm diameter, 0.305 m long, aluminum roller was then used to compact the soil as shown in Figure 9c. To increase uniformity, the roller was passed axially, then transversely, then axially for each lift. Moisture was then added to bring the soil to up to a 6.3% moisture content using a spray bottle. Finally, a thin layer of construction chalk was added between selected lifts for diagnostic purposes as shown in Figure 9d. Immediately after the soil was placed in the box, the box was tightly covered to prevent moisture loss. Typically, two hours elapsed between final box preparation and when the test was conducted.

Diagnostics

Test diagnostics include measurement of the test setup parameters, e.g., impact angle and velocity, and the test results parameters, e.g., soil cratering and liquid deposition. These will be discussed separately.

Test Setup Diagnostics

The impact angle, i.e., the acute angle from the horizontal to the line of travel of the wing, is measured with a Sears Protractor Model 939840. It is placed on the top of the gun strong-back as it is being winched to the desired angle. The accuracy is +/- 1°.

Impact velocity is inferred from time-of-arrival measurements. Measurements are made with 4 photodiodes spaced 2 cm apart with the last one placed 5 cm prior to where the acceleration of the wing is terminated by the pushrod impacting the stop-bolt catcher. The time-of-arrival signals are recorded on LeCroy 8610 transient digitizers with typically 0.5 μs resolution. For the speeds of interest, the uncertainty due to digitizing error is less than 1%. The actual impact velocity of the liquid jet may be slightly different than the velocity recorded from time-of-arrival. After passage through the time-of-arrival gage, the wing continues to accelerate for 5 cm. On the other hand, when the wing impacts the balsa wood in the wing catcher and decelerates, the liquid does not continue to travel unimpeded. It must first break the polyethylene barrier at the front of the wing, overcome the vacuum created in the closed wing as it exits, and overcome air drag between the wing assembly and the target soil. These effects are not measured; however, they are assumed to be either negligible or offsetting.

The ambient pressure, temperature, wind speed, and direction were also measured for each test. Ambient pressure was measured with a Wallace & Tiernan Model FA129 gage with

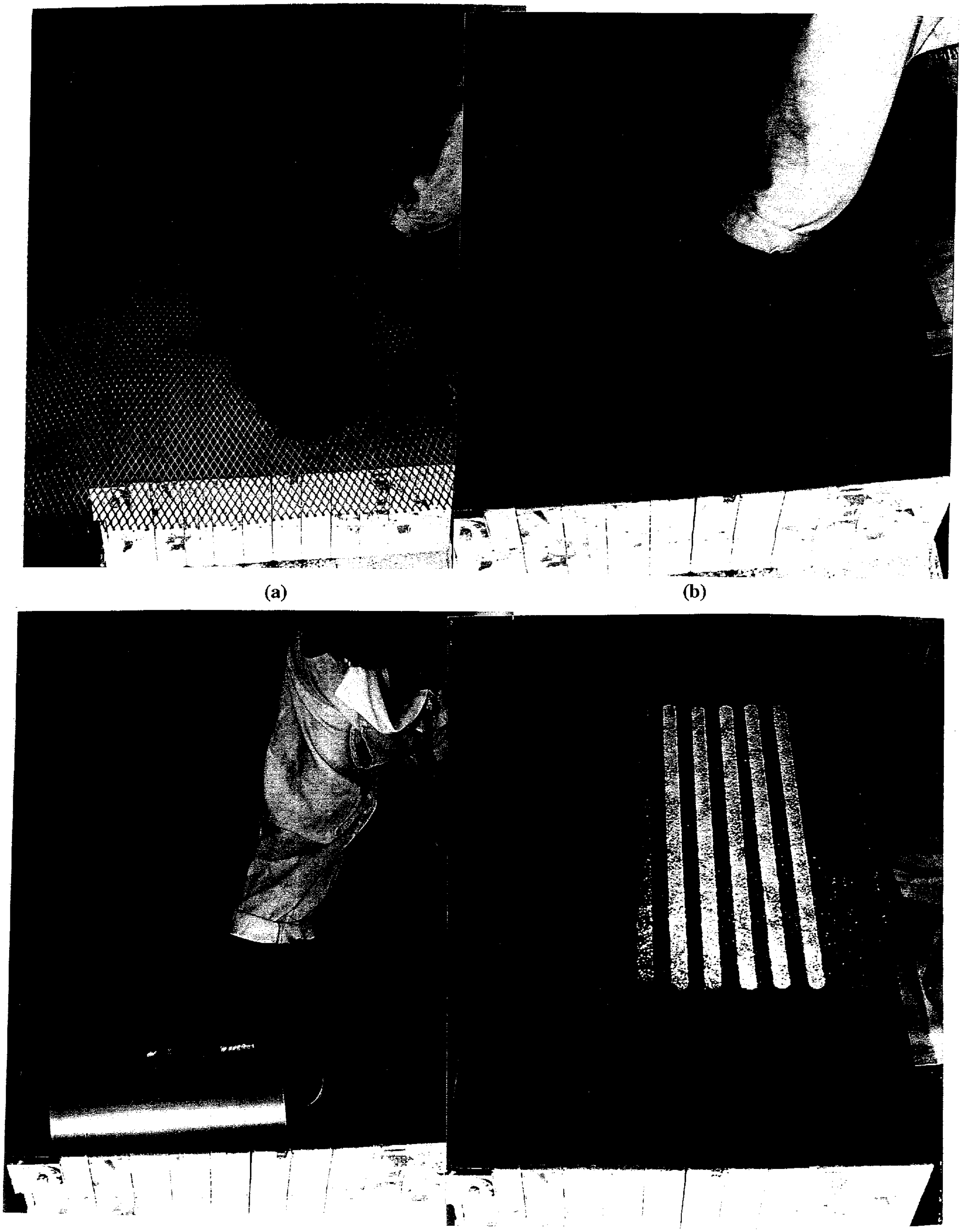

(a) (b)

(c) (d)

FIGURE 9. Soil Preparation Procedures. (a) Adding a lift to the box, (b) Distributing the soil within the box, (c) Compressing the soil, and (d) Adding chalk lines to mark soil layers.

an estimated uncertainty of less than 1kPa. The ambient temperature was measured with a K-type thermocouple with an estimated uncertainty of 2°C. The wind speed was measured with a Taylor windscope model E at about 10 meters above the gun with an estimated uncertainty of 2 m/s. The prevailing wind direction was also recorded but is not reported since the wind speeds for all tests were under 5 m/s.

The soil density and moisture content were also measured for each test and are discussed in the soil characteristics section.

Test Results Diagnostics

After a test, the impact crater was divided spanwise into two sections. One side was used for crater volume and soil deformation measurements and the other side was used for soil moisture measurements.

The crater volume measurements where made by filling one-half the crater with plaster-of-paris.The top of the plaster cast was smoothed off consistent with the upstream (negative x direction in Figure 10) rim of the crater. For the 22.5° and 45° impact angles, the upstream rim appeared to be at its undisturbed, pre-impact elevation. For the 67.5° impact tests, the upstream rim was elevated above the initial pre-impact soil elevation. The plaster cast was then removed from the soil and weighed. The volume of the crater was then determined from a reference density measurement of plaster-of-paris.

The effect of the cratering process in soil was measured by sectioning the soil after removing the plaster cast. Chalk lines placed in the soil, as the test bed was prepared, showed soil deformation due to the impact. The soil experienced compression, and in some cases tension. Five sections were made of each test and photographed with a 35 mm Minolta Maxxum 7000 camera. The first section corresponded to the centerline of the impact, $z = 0.0$ m in Figure 10. Parallel sections were cut at $z = -5.08$ cm intervals, with the fourth section corresponding to the edge of the impinging liquid jet.

The craters appear deeper in the photographs than they actually were. This occurred because the plaster cast adhered to the soil, typically removing an additional 1 cm around the cast as the cast was removed from the soil. Otherwise the soil was undisturbed by the casting process. Using these measurements, the relative contributions of soil deformation and soil erosion to the cratering process can be determined.

The amount of water remaining in the crater from the water jet impact was measured. For tests early in the test series, the soil beneath the crater was excavated as a single sample. In later tests, the soil beneath the crater was excavated in three sections, i.e., the leading edge, the bottom, and the trailing edge of the crater. In either case, one-half the impact crater was excavated leaving the other half for casting of the crater and sectioning of the soil.

The excavated soil sample(s) were weighed wet, baked dry, and then reweighed. The scale used in these tests was a Sartorious Model 3807 MP8 which is accurate to +/- 1 gram. The difference in the wet and dry weights represents the total moisture in the soil. A large

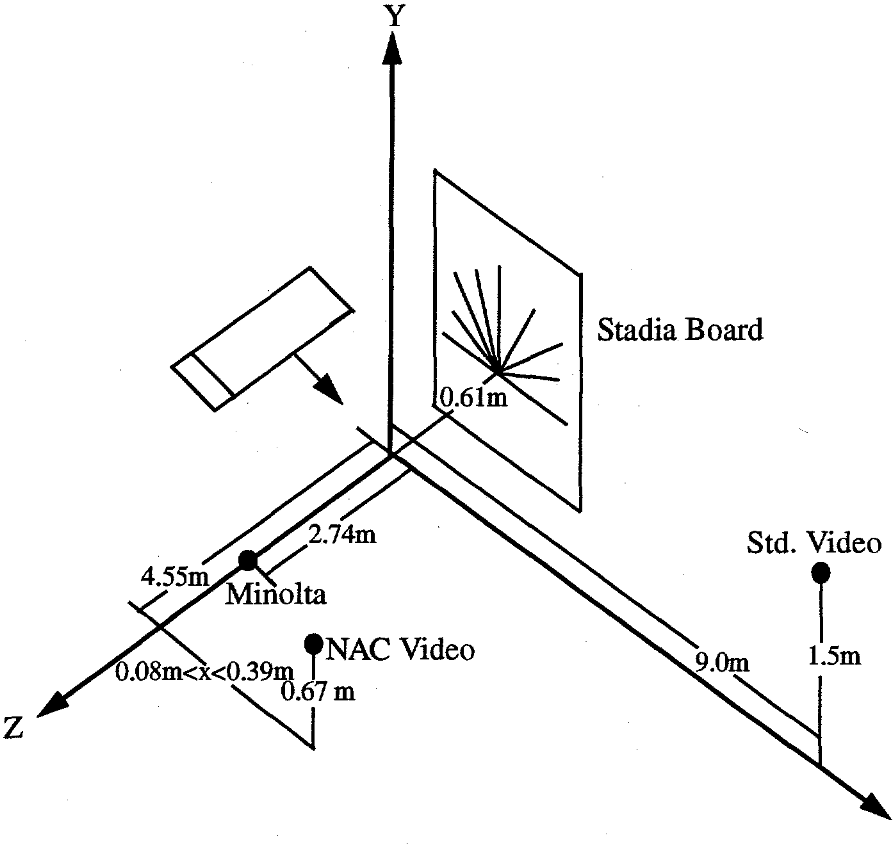

FIGURE 10. Location of Cameras (Not to scale).

fraction of this water weight is due to the pre-impact soil moisture content. The pre-impact soil moisture content for each test was determined from the sand cone measurements described in the Soil Characteristics section. Subtracting off the pre-impact soil moisture gives the amount of water remaining in the soil due to the water jet impact. Care was taken to excavate a sufficiently large amount to ensure that all the moisture introduced by the impact was collected but not too much so as to reduce the sensitivity of the measurement. The amount of soil that required excavation was apparent from the change in coloration of the soil with increased wetness. Care was also taken to minimize the error introduced by evaporation of the water from the crater surface. Immediately after a test, the crater was covered to prevent moisture loss and excavation of the soil into a sealed vessel occurred within 10 minutes after each test. Sensitivity tests conducted prior to the test series indicated that this measurement technique was good to about +/- 2 grams. For most results, this represents about a +/- 5% measurement error.

Photometrics were used to record the fluid motion as shown in Figure 10. Side views of the impact were taken with a 35 mm Minolta Maxxum 7000 camera and a NAC 1000 high-speed video operating at 500 fields/sec (250 frames/sec). The Minolta was used to record single, high-resolution images at 1/2000 sec. It used a 50 mm focal length lens and was positioned perpendicular to the line of impact at $z = 2.74$ m ($x = y = 0.0$ m). The NAC high-speed video recorded full frame images, used a 17 mm focal length lens, and was positioned at y = 0.67 m above the horizontal impact plane, z = 4.55 m, and x = 0.08 m, 0.32 m, and 0.39 m, forward of the impact line for 22.5°, 45°, and 67.5° impacts, respectively. A stadia board with angular reference marks was positioned at z = -0.61 m (x = y = 0.0 m) beyond the center of the impact line. An overall end view was recorded with standard, 30 frame/sec video. The camera was positioned approximately x = 9.0 m downstream of the impact point at an elevation of approximately z = 1.5 m.

Procedures

Test procedures were as follows. All consumable items, such as push rods and wing assemblies were manufactured in advance of the tests. The day before each test, the gun was loaded with the pusher plate and push rod assemblies. Each morning prior to the test, a soil target was prepared, the photometrics set up, and the gun elevated to the desired angle. Just prior to the test, the test bed was positioned, the wing was filled with liquid and then positioned. Up to this point in the test, the test bed had been covered to reduce moisture loss. The area was then cleared of personnel and the gun was pressurized. An Artisan Digital Event Programmer Model EPC-12653 timer was used as an automatic sequencer for triggering the transient digitizers and the 35 mm camera relative to triggering the gun. Immediately following the test, the test bed was again covered to prevent moisture loss. One-half the crater was excavated for moisture content immediately, followed by the sand cone test for soil density and pre-impact soil moisture. The other half of the crater was then cast with plaster-of-paris and allowed to dry. The cast was removed and the soil sectioned and photographed. The tests took about one-day per test to complete.

Test Results

The test matrix is given in Table 2. The test order was random with tests 9 through 12 being conducted before 1 through 6. (Results from tests 7 and 8 were not used.)

Table 2. Test Matrix Numbers for Impact Angle and Impact Velocity.

		Impact Angle (Degrees)		
		22.5	45	67.5
Impact Velocity (m/s)	30	9	10	11
	64	3	6,12	1
	92	4	5	2

Data Ranges/Uncertainties

The uncertainty in the impact angle in Table 2 is +/- 1° for all impact angles.The impact velocity levels listed in Table 2 are average values. For the 30 m/s tests, the actual impact velocities ranged from 29.4 to 29.8 m/s. For the 64 m/s tests, the actual impact velocities ranged from 60.1 to 67.4 m/s. For the 92 m/s tests, the actual impact velocities ranged from 89.4 to 93.8 m/s. Table 3 lists the parameters held constant, their values, and ranges for the test series.

Table 3. Parameters for the Test Series

Parameter	Average Value	Range
Ambient Temperature (C)	17.	4. - 37.
Ambient Pressure (kPa)	84.	84. - 85.
Ambient Wind Speed (m/s)*	2.3	0 - 4.5
Water Mass in Wing (g)	362	328 - 396
Soil Density (kg/m^3)	1389	1361 - 1435
Soil Moisture (Mass %)	6.3	5.6 - 6.8

---

*Wind direction varied substantially but is not given here because the average wind speed was so low relative to the impact velocities tested.

For all tests, water was used as a simulant for JP-4/JP-8 jet fuel. Its choice simplified the environmental and safety considerations associated with the testing. A small amount of green food coloring was used to enhance the visibility of the liquid jet for photographic purposes.

The dependent variables measured for each test were the volume of liquid in the crater, the volume of the crater, the maximum depth of the crater, the breadth of the crater at the crater surface, and the location of the maximum depth of the crater forward of the impact line. For presentation purposes, the volume measurements are normalized with the jet volume and the distance measurements are normalized with the jet chord length. (Note: scaling implications are addressed in the Discussion section of this report.) The geometry of the crater is shown in Figure 1. The uncertainty associated with each of these measurements is given in Table 4. These uncertainties are determined from repeat tests conducted at an impact velocity of 64 m/s and an impact angle of 45°. Since the repeat data is sparse, the values in Table 4 represent the largest variance of repeat test conducted with both wing designs shown in Figure 4.

Table 4. Uncertainty in Measured Dependent Variables for the Test Series.

Variable	s^* @ 64 m/s, 45°
Volume of the Liquid/Jet Volume	10%
Volume of the Crater/Jet Volume	4%
Average Crater Breadth/Wing Chord	13%
Average Crater Depth/Wing Chord	8%
Average Position of the Crater/Wing Chord	30%

---

*s= | (V2-V1)/(V2+V1) | and V1 and V2 are the value of the variables for the first test and the repeat test respectively. The uncertainty is given by +/- 2s.

The breadth, depth, and location of maximum depth of the crater given in Table 4 are spanwise averages at 4 sections. The first section corresponds to the centerline of the impact, z = 0.0 m in Figure 10. The other sections are at z = -5.08 cm intervals, with the fourth section corresponding to the spanwise edge of the impinging water jet. In general, the crater cross-sections were reasonably uniform from the centerline of the liquid jet to the edge of the liquid jet. Beyond the edge of the liquid jet, the maximum depth of the crater decreased continuously. A measure of the non-uniformity of the crater can be defined as difference between the cross-section with the maximum bottom depth and the cross-section with the minimum bottom depth, divided by the average bottom depth of the four cross-sections between the liquid jet centerline and edge. The average value of this statistic for the test matrix is 0.26, i.e., the difference in maximum depth for the four sections averaged about +/- 1/2 of the average depth.

Photometric Results

High speed video was recorded for all tests. Its primary value is in identifying the overall sequence of events. At the moment of impact, the liquid jet begins compression of the soil and a finely atomized mist can be seen as the water jet breaks up on impact. Later in time, soil erosion occurs and soil fragments can be seen following the liquid mist out of the crater. For all tests with impact velocities of 64 m/s and 92 m/s, the liquid leaving the crater was completely atomized. The end view video camera shows that the finely atomized liquid is carried up to several meters downrange before settling out on the ground. For the tests at an impact velocity of 30 m/s, the liquid jet was not finely atomized on impact. Particularly for the test with an impact angle of 22.5°, the fuel flowed along the surface as a coarse spray.

In addition to the high speed video, the impact sequence was recorded with a 35 mm still camera, acquiring a single frame for each test. Examples are shown in Figure 11 for an impact angle of 45°. Figure 11a shows the jet at the moment of impact with the soil (for an impact velocity of 92 m/s). Figure 11b shows the atomization of the jet resulting from impact (for an impact velocity of 64 m/s).

The post-test crater results were also recorded with 35 mm still photographs. Figure 12 shows an overhead view of the craters before they were casted and excavated for selected tests. Still photographs of the soil cross-sections were also taken for each section (5 per test at 5.08 cm intervals) for each test. Figure 13 shows the cross-section taken 5.08 cm from the wing centerline for selected tests. A complete set for each test is in Appendix A.

As can be seen in Figure 13, the crater depth increases with increasing impact angle and impact velocity. In each figure, the jet entered the crater from the left, nominally at the location of the vertical string. For the shallow impact angles, the chalk marks are depressed only, indicating compression of the soil due to the impact of the jet with the soil. However, for the steep impact angles, the chalk marks rise above the initial pre-impact elevation. This indicates that sections of the soil were also subject to shear forces as the liquid from the jet exited upward out of the crater.

In all cases, some of the soil is removed from the crater by erosion as the liquid jet exits the crater, as evidenced by soil downstream of the soil impact box for all tests. Erosion is somewhat difficult to discern directly from the photographs in Figure 13 since some soil immediately under the craters was removed in the plaster cast removal process. Figure 14 shows a soil section before and after removal of the plaster cast. Figure 15 shows an example of the plaster cast after it has been removed and sectioned in 5.08 cm intervals corresponding to the soil cross-sections.

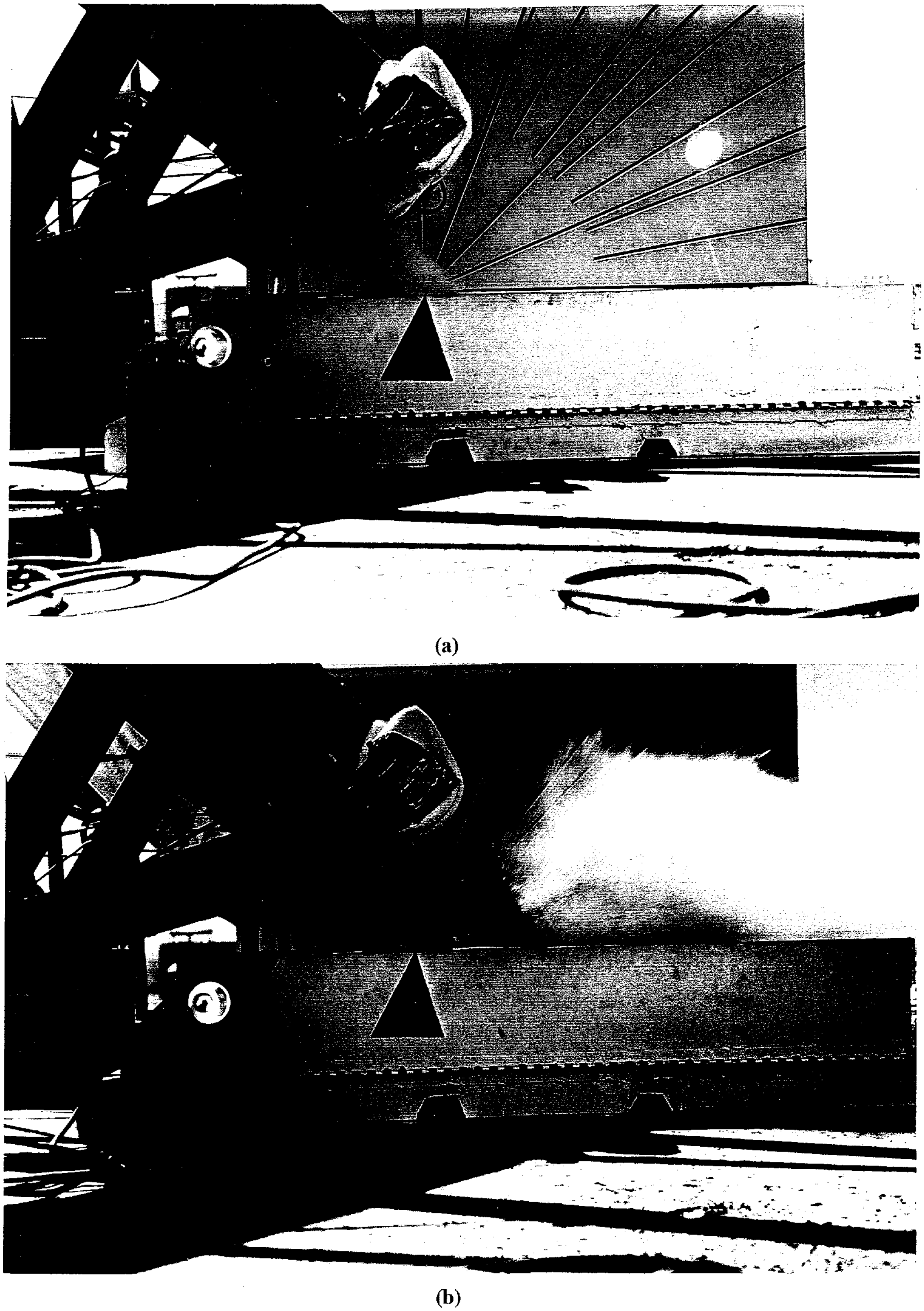

FIGURE 11. Photographs of Jet Impingement at an Impact Angle of 45°. (a) At the instant of impact. V= 92 m/s. (b) Several milliseconds after impact a finely atomized water mist followed by soil fragments can be seen leaving the crater. V=64 m/s. Exposure times = 500μs.

30 m/s at 25 degrees

30 m/s at 67.5 degrees

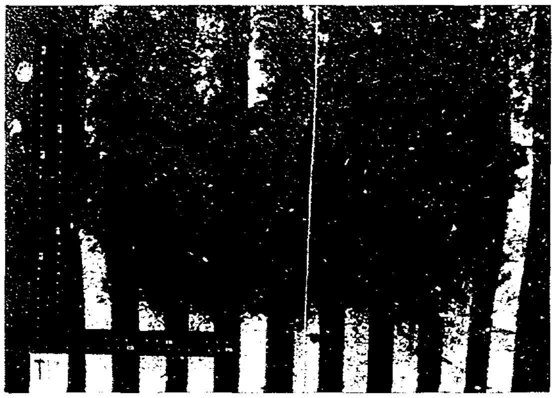

64 m/s at 45 degrees

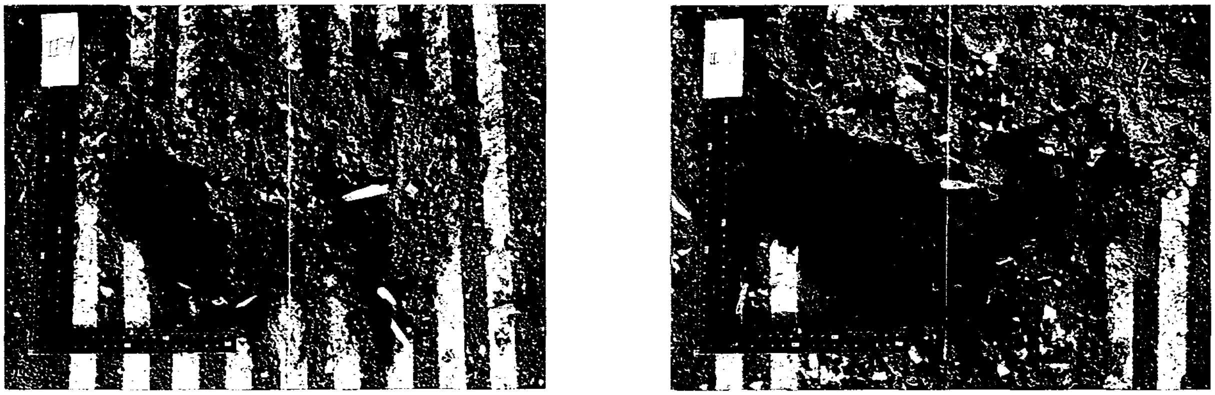

92 m/s at 22.5 degrees

92 m/s at 67.5 degrees

FIGURE 12. Overhead View of Impact Craters for Selected Tests.

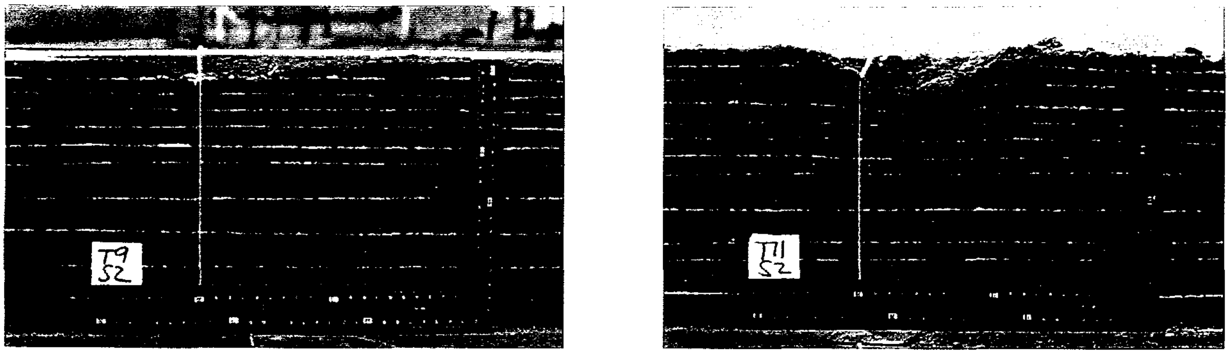

30 m/s at 25 degrees

30 m/s at 67.5 degrees

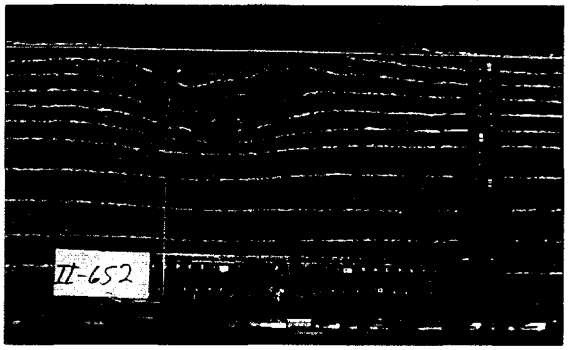

64 m/s at 45 degrees

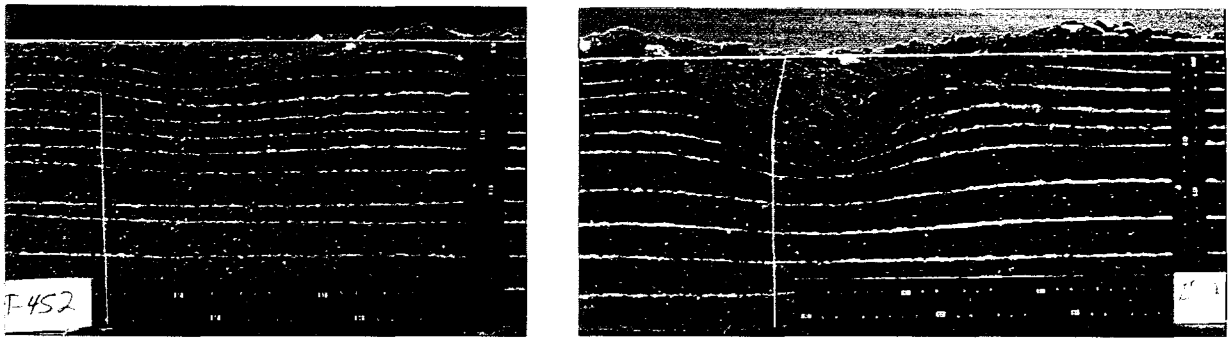

92 m/s at 22.5 degrees

92 m/s at 67.5 degrees

FIGURE 13. Soil Deformation Due to the Cratering Process. Cross-sections taken parallel to the direction of impact at 5.1 cm from the wing centerline for selected tests. Chalk lines between soil layers indicate the deformation.

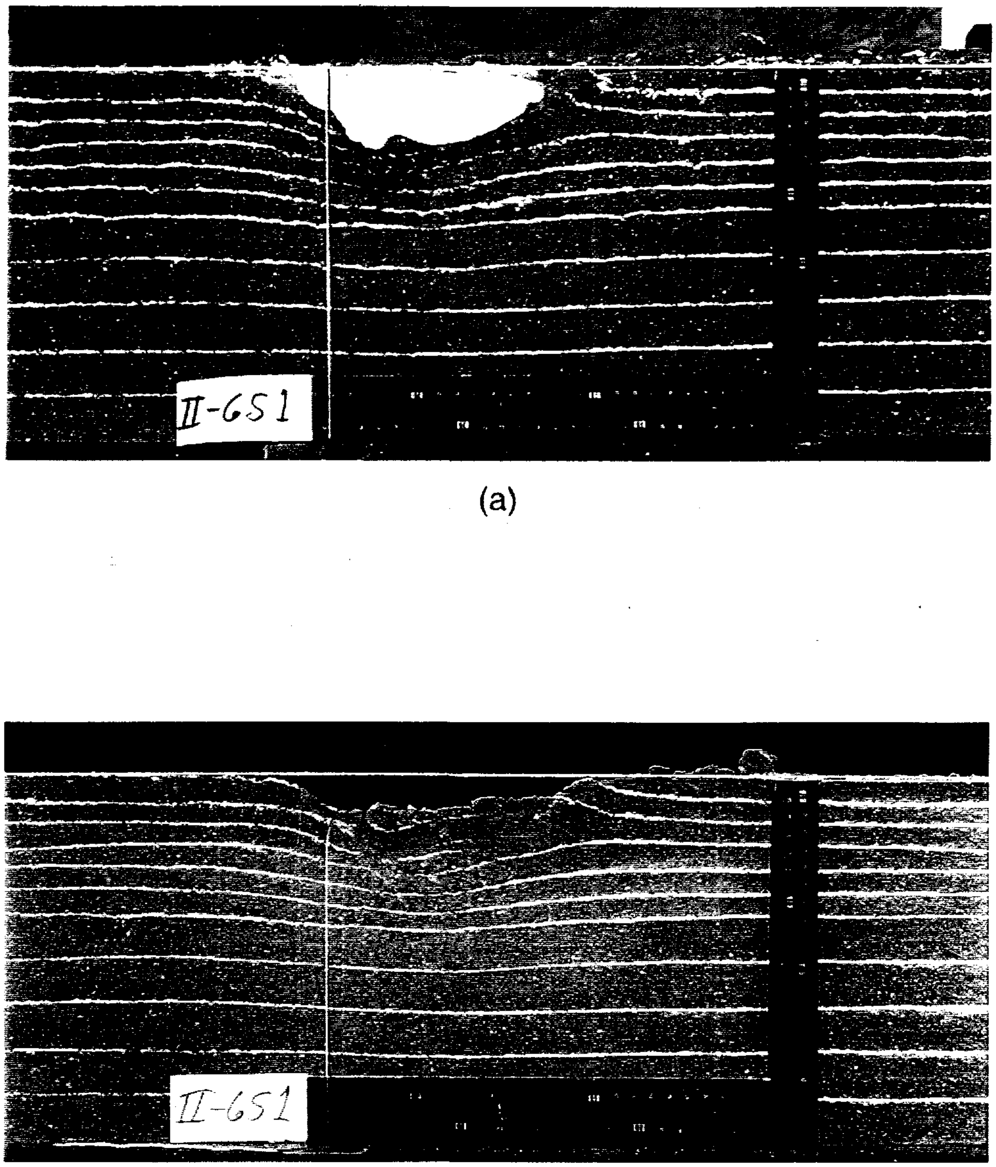

(a)

(b)

Dominguez before and after picture

FIGURE 14. Soil Cross-sections Parallel to the Direction of Impact Along the Wing Centerline for an Impact Angle of 45° and Impact Velocity of 64 m/s. (a) With the plaster cast. (b) After removal of the plaster cast.

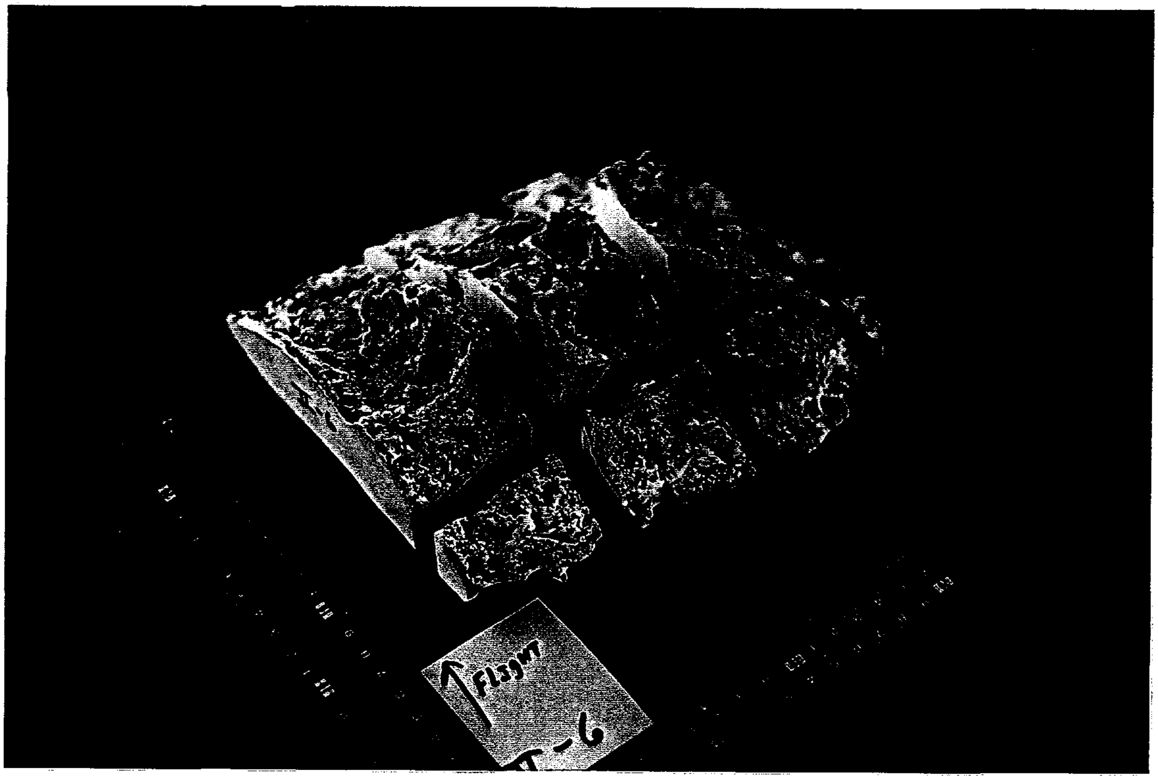

FIGURE 15. Photograph of a Plaster Cast of the Crater Formed for an Impact Angle of 45° and an Impact Velocity of 64 m/s. Only one-half the span of the impact crater was cast, the other half of the crater was excavated for moisture measurements. The casts were sectioned to compare with soil cross-sections.

Liquid Pooling Measurements

One of the primary measurements of importance for the test series is the amount of liquid remaining in the crater after the impact. Table 5 lists the results as a percent of the incident jet mass.

Table 5. Experimental Results for Percent of Initial Mass Remaining in the Crater After Impact

		Impact Angle (Degrees)		
		22.5	45	67.5
Impact Velocity (m/s)	30	18%	23%	37%
	64	14%	38%,31%	34%
	92	10%	37%	38%

In general, the percent of initial mass remaining in the crater increases with increasing impact angle, however, there is no clear trend with increasing impact velocity. For high impact angles, i.e., 45° and above, the amount of mass in the crater varies from about 25% to 40%. For low impact angles, i.e, below 45°, the percent of mass remaining in the crater is less than 20%.

The distribution of liquid within the crater is also of importance. Large differences will exist in the fire size and duration if the liquid pools only in the bottom of the crater, or is uniformly distributed throughout the crater. For tests conducted later in the test series, three measurements for liquid remaining in the soil were made, at the leading edge of the crater, at the bottom of the crater, and at the trailing edge of the crater. The fraction of the crater measured for each area varied slightly for each test. In order to give an estimate of the uniformity of the distribution of fuel throughout the crater, the following definition is made:

$$\text{FFAF} = \text{Fuel Fraction / Area Fraction} = \frac{\text{Mass in Measurement Area/Total Mass}}{\text{Measurement Area/Total Area}} \qquad (1)$$

The statistic, FFAF, is useful because its value is unity if the liquid is uniformly distributed. A value less than unity indicates that the area received less liquid than the average, e.g. a value of 0.5 indicates that the area receive 1/2 the amount it would have received if the liquid were uniformly distributed. A value greater than unity indicates that the area received more liquid than average, e.g., a value of 2 indicates that the area received twice the amount it would have received if the liquid were uniformly distributed. The statistic, FFAF, is calculated for each measurement area, i.e., leading edge, bottom, and trailing edge of the crater as listed in Table 6.

Table 6 shows that the liquid is relatively uniformly distributed. No area has more than 61% greater amount of liquid than it would have if the liquid were evenly distributed. Also no area has less than 1/4 the amount of liquid that it would have if the liquid were evenly distributed. For the above measurements, s is about 0.4, so the uncertainty is +/-0.8.

Table 6. Uniformity of Mass in the Crater. See text for statistic used. The columns L, B. T, denote that the measurement was taken at the Leading (or upstream) edge, the Bottom (or middle), and the Trailing (or downstream) edge, of the crater respectively.

		Impact Angle (Degrees)								
		22.5			45			67.5		
		L	B	T	L	B	T	L	B	T
Impact Velocity (m/s)	64				0.25	1.09	1.38	0.82	1.25	0.79
	92	1.08	0.81	1.33	1.05	1.09	0.82	0.76	1.61	0.76

Crater Volume Measurements

Crater volume measurements were taken for each test from the plaster casts such as the one shown in Figure 15. The results are listed in Table 7 as a fraction of the incident jet volume (362 cc). The crater-volume/incident-jet-volume is greater than unity except at low impact angles and low velocities. This implies that for the soil conditions tested, the crater volume generally exceeded that of the wing volume. Table 7 shows that the crater volume increases with increasing impact angle and increasing impact velocity.

Table 7. Experimental Results for Crater-Volume/Incident-Jet-Volume

		Impact Angle (Degrees)		
		22.5	45	67.5
Impact Velocity (m/s)	30	0.37	0.79	1.7
	64	2.3	4.2,4.1	6.2
	92	2.3	7.9	9.7

Maximum Crater Depth Measurements

Crater depth measurements were taken for each test. As noted earlier, maximum depth measurements were taken at four sections and the results averaged. The average maximum depth results are listed in Table 8 as a fraction of the chord length (8.4 cm) of the liquid jet. In general, the crater-depth/chord-length is less than unity. This means that for the soil conditions tested, the crater depth never exceeded the chord length of the wing. Table 8 shows that the crater depth increases with increasing impact angle and increasing impact velocity.

Table 8. Experimental Results for Crater-Depth/Wing-Chord

		Impact Angle (Degrees)		
		22.5	45	67.5
Impact Velocity (m/s)	30	0.05	0.20	0.31
	64	0.27	0.57,0.57	0.68
	92	0.29	0.79	0.94

Crater Breadth Measurements

The breadth of the crater was measured for each test. The breadth of the crater is defined as the distance between the leading and trailing edges of the crater at the crater surface. The distance between the leading and trailing edges of the crater cast was measured at four sections and the results averaged. The average crater breadths are listed in Table 9 as a fraction of the chord length (8.4 cm) of the liquid jet. In general, the crater-breadth/chord-length is about two. This means that for the soil conditions tested, the crater breadth is on the order of twice the wing chord length. Table 9 shows that the crater breadth has no clear trend with either impact angle or impact velocity.

Table 9. Experimental Results for Crater-Breadth/Wing-Chord

		Impact Angle (Degrees)		
		22.5	45	67.5
Impact Velocity (m/s)	30	2.6	1.4	1.2
	64	1.7	2.0,1.6	1.9
	92	1.70	2.3	2.7

Position of Crater Forward of the Impact Point

The position of the crater relative to the impact line was measured for each test. The position of the crater is defined as the distance between the impact line and the line of maximum depth of the crater. The distance between the impact line and maximum depth was measured at four sections and the results averaged. The average positions forward of the impact line are listed in Table 10 as a fraction of the chord length (8.4 cm) of the liquid jet. In general, the crater-position/chord-length is unity or less. Table 10 shows that the crater position forward of the impact line has no clear trend with either impact angle or impact velocity. Further, the repeat test covers a large portion of the data range.

Table 10. Experimental Results for Crater-Position/Wing-Chord

		Impact Angle (Degrees)		
		22.5	45	67.5
Impact Velocity (m/s)	30	0.66	0.57	0.33
	64	0.39	0.81,0.44	0.27
	92	0.91	0.45	0.45

Derived Quantities for Risk Assessment Compatible Model

To support risk-assessment-compatible model development for weapon-system-safety-assessment (WSSA) studies, the measurements can be reduced to three variables: 1) the area covered by the fuel, A, 2) the amount of fuel in that area as expressed as an equivalent liquid layer thickness, δ, and 3) the distance of the area from the impact line, P. These variables are needed as functions of the impact angle, α and the impact velocity, V.

Area Covered by the Fuel

In order to define an area covered by the fuel, it is necessary to reduce the data to a simplified geometry. For this purpose we will define an "Equivalent Elliptic Crater" as shown in Figure 16. For the purposes of a WSSA it is sufficient to define the fire area as the projected surface area covered by the fuel. In terms of the idealized geometry in Figure 16, the fire area is given by

$$A = SB \tag{2}$$

where S is the crater span and B is the crater breadth.

As an idealization consistent with Figure 16, the crater span, S, is taken to be span of the liquid jet. In general, the crater span was slightly larger than the wing span due to edge effects on cratering but rarely more than 30% greater. This was determined by sectioning of the soil bed beyond the span of the wing. For the test series, the span , S, is fixed at 30.5 cm.

The crater breadth, B, is taken from the data in Table 9 normalized by the wing chord, C. As noted earlier, the crater breadth shows no clear trend with either impact angle or impact velocity. However its scatter is not large. The data can be covered by

$$\frac{B}{C} = 1.9 \pm 0.95 \quad . \tag{3}$$

Equivalent Liquid Layer Thickness

For the purposes of a WSSA it is most convenient to idealize the distribution of fuel in the crater as a thin, uniform liquid layer of a given thickness, i.e, an equivalent liquid layer thickness. For a given burning rate of fuel, the equivalent liquid layer thickness can be converted to a burn time.

As noted earlier, the fuel is not uniformly distributed. However, from the uncertainty in the data, no area within the crater will have a thickness that is more than 1.8 times greater than the assumed uniform thickness. The uncertainty introduced in assuming uniformity is less

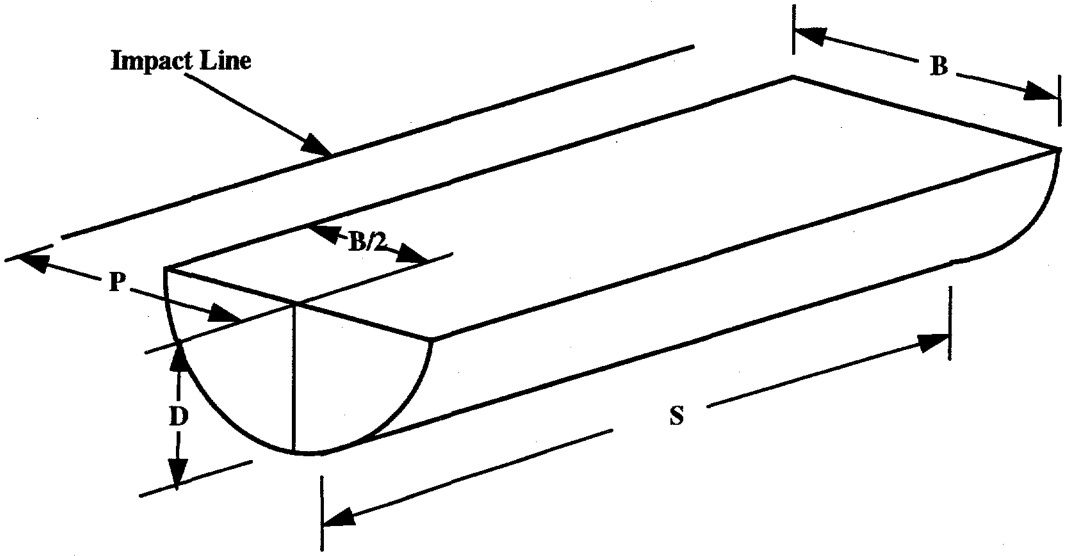

FIGURE 16. Geometry of the Equivalent Elliptic Crater. S, is the span of the crater. B is the breadth of the crater. D is the depth of the crater, and P is the position of the crater forward of the impact line.

than a factor of 2. This uncertainty is less than the uncertainty that will be introduced by assuming that the fuel in the soil beneath the crater will have the same burn rate as a liquid layer on the surface. This latter assumption is necessary since burn rates in porous media are not known.

Referring to Figure 16, the surface area of the crater for fuel impregnation is given by

$$A_{fs} = \pi S\left(\frac{B^2}{8} + \frac{D^2}{2}\right)^{1/2} . \tag{4}$$

The equivalent liquid layer thickness is then given by

$$\delta = \frac{\vartheta_{fuel}}{A_{fs}} . \tag{5}$$

The volume of fuel in Equation 5 is determined from the initial volume of fuel and the percent remaining in the crater from Table 5. The fuel surface area in Equation 5 is given by Equation 4 where *B* and *D* are determined from Tables 9 and 8, respectively, for the given wing chord.

Table 11 lists the liquid layer thickness as a fraction of the wing chord. The values of the liquid layer thickness range from about 1% to 4% of the wing chord. In general, the liquid layer thickness decreases with increasing impact velocity but increases with increasing impact angle. In other words, for a given impact velocity, the greater the normal component, the thicker the liquid layer will be. However, for a given impact angle, the higher the impact velocity, the lower the thickness.

Table 11. Fuel-Layer-Thickness/Wing-Chord Deduced from the Data.

		Impact Angle (Degrees)		
		22.5	45	67.5
Impact Velocity (m/s)	30	0.011	0.025	0.043
	64	0.012	0.027,0.024	0.020
	92	0.009	0.020	0.018

As a derived quantity, the liquid layer thickness incorporates uncertainty from the liquid volume measurements, the crater depth and volume measurements, as well as, folding in the uncertainties in defining the crater span to be a fixed value. In spite of this, the response surface appears to be relatively smooth. A correlation coefficient (R^2) of 0.75 is obtained for

$$\frac{\delta}{C} = 7.3x10^{-4} + 0.218\frac{\sin\alpha}{V^{1/2}}. \tag{6}$$

In Equation 6, the equivalent-liquid-layer-thickness/wing-chord, δ/C, is dimensionless, the impact velocity, V, is in m/s and the impact angle, α, is in degrees. Table 12 lists the predictions of Equation 6 for the conditions given in Table 11.

Table 12. Fuel-Layer-Thickness/Wing-Chord Predictions by Equation 6.

		Impact Angle (Degrees)		
		22.5	45	67.5
Impact Velocity (m/s)	30	0.016	0.029	0.038
	64	0.011	0.019	0.027
	92	0.009	0.018	0.022

Position of the Fuel Surface Forward of the Impact Line

To position the fire area relative to the impact point, Figure 16, shows the position, *P*, of the fuel surface forward of the impact line. This average position normalized by the wing chord, *C*, given in Table 10 is consistent with the idealized geometry in Figure 16. The data in Table 10 show no clear trend with either impact angle or impact velocity. However, the range of data can be covered by

$$\frac{P}{C} = 0.6 \pm 0.6 . \tag{7}$$

Numerical Simulation

Numerical Model

This present study focuses on the problem of modeling a liquid impacting into soil. However, the ultimate goal will be to model the fluid and the thin structure containing the liquid impacting into soil. This later simulation will require a numerical method capable of modeling the structural interaction of the container, liquid, and soil.

Modeling fluid-structure interaction with soil erosion presents problems for most numerical techniques. Standard Lagrangian techniques cannot be used because the material deformations become large enough to severely distort or tangle the mesh, causing the calculation to break down. In addition, the ejection of material from the crater is very difficult to model using a standard Lagrangian finite element method.

One could use an Eulerian or Arbitrary Lagrangian-Eulerian (ALE) method for modeling the fluid splash and the soil impact. In an Eulerian calculation, the grid stays fixed, and the material flows through the grid. While Eulerian methods can model the gross motion of the fluid and the soil, these methods will have difficulty modeling the thin shell container. In addition, Eulerian methods have difficulty because of their lack of a material history and because they smear and spread information (referred to here as diffusion) as the mass moves through the fixed-in-space grid.

For the present study, the Smooth Particle Hydrodynamics (SPH) method has been coupled with the transient dynamics finite element code PRONTO (Taylor and Flanagan, 1987, Taylor and Flanagan, 1989, Attaway 1990) providing a combined capability exceeding either method. This SPH-PRONTO coupling (Attaway, Heinstein and Swegle, 1994), is attractive for solving the liquid-soil impact problem, because it allows the fluid and soil to be modeled using SPH elements. The thin wing structure can be modeled with a shell-type finite element.

The goal of the present effort is to evaluate the feasibility of PRONTO/SPH for the analysis of the experimental results. A future effort will be required to focus on the confining wing structure, its break-up, and the interaction of the fuel, wing and soil. The ultimate goal is developing a method for predicting the distribution of fuel in a crash.

Introduction to Smooth Particle Hydrodynamics

SPH is a relatively new numerical technique having several unique characteristics that make it attractive for this problem (Lucy, 1977, Gingold and Monaghan, 1977, Gingold and

Monaghan, 1982, Monaghan, 1982, Monaghan and Gingold, 1983, Cloutman 1990a, Cloutman, 1990b, and Libersky and Petschek, 1990). SPH is a gridless Lagrangian method where material points are tracked with 'particles' that move with the flow. The terms 'particle' and 'hydrodynamic' are misnomers. The term 'particle' really refers to interpolation (material) points within a continuum. This method is not really hydrodynamic since strength is easily included. Another confusing SPH terminology is the label of SPH as a 'gridless' method. This method is called 'gridless', but in effect, a local grid is built for each time step after identifying the neighbors of each material point.

The governing equations of the SPH method can be derived from the same variational principles as the finite element method (Attaway, 1994). This similarity with the finite element allows SPH to be embedded within the finite element architecture as a special element type. For the PRONTO/SPH coupling, a list of neighbors is constructed using an efficient search algorithm (Swegle, Attaway, Heinstein, Mello, and Hicks, 1994). This list is then used to construct a kernel sum approximation of the velocity gradient and the stress divergence. Contact surface algorithms from the finite element method are used to couple the SPH elements with the finite element method.

Details of the SPH computational technique and details of the implementation into PRONTO can be found in Attaway, 1994, and Swegle, Attaway, Heinstein, Mello, and Hicks, 1994.

Problem Description and Assumptions

The fuel and soil directly under the impact was modeled assuming plane strain deformation. Near the ends of the fluid jet, this assumption breaks down. The uniform deformation observed in the experimental crater formation suggests that the plane strain assumption is valid.

SPH elements are computationally more expensive due to the need to redefine neighbors at each time step. For this reason, they were only used for the fuel and the soil directly under the impact point where deformations were expected to be large. Finite elements were used to model the soil surrounding the impact point where the deformations were expected to be small (strain <<1). A contact surface was used to couple the SPH elements and the soil elements.

Figure 17 shows the problem's geometry. A 7.62 cm (3.0 inch) slug of water was modeled using twelve SPH elements through the thickness and 48 elements along the length. Two variations were used to model the thickness of the jet. For no spreading of the liquid in flight, the jet thickness equaled 1.27cm (1/2 inch). To account for air-drag induced fluid spreading in an economical way, the liquid jet was also approximated as a 0.64 cm thick central core at full density surrounded by a 0.64 cm thick slabs at 1/2 normal density as shown in Figure 17. The soil was modeled with 7680 SPH elements with an average radius of 0.15 cm. The depth of soil used in the numerical model was the same as in the experimental setup.

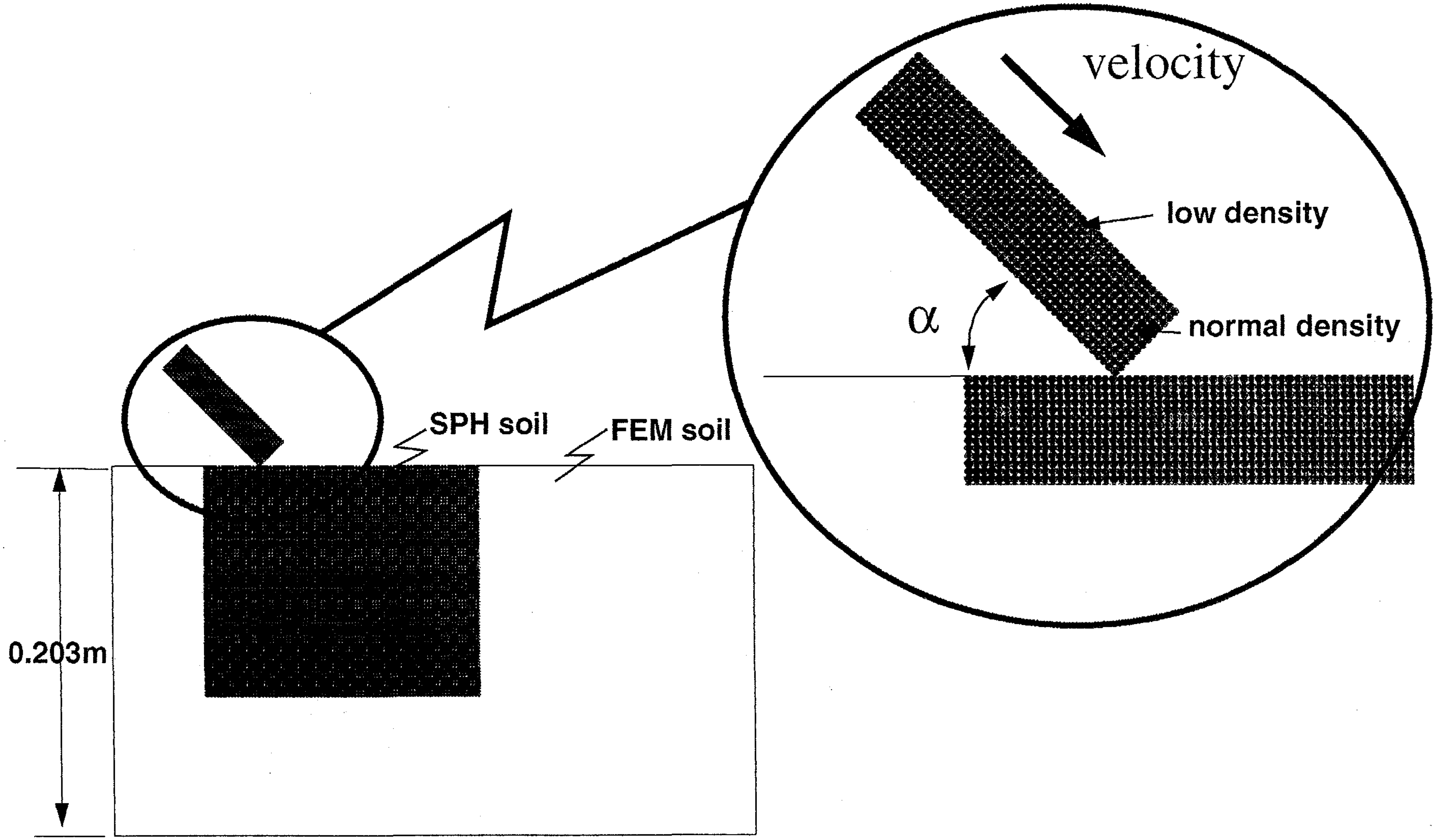

FIGURE 17. Numerical Model Geometry for Liquid Jet Impacting Soil.

The fluid was modeled with a Mie-Grueneisen equation of state with a nominal density of 1.0 g/cm^3, sound speed of 3446.7 m/s, a Grueneisen parameter, $\gamma = 1.0$, and a coefficient of linear particle velocity to shock velocity $S = 1.921$.

Because of the variability of soil, a simple constitutive relation was selected for the numerical model for soil. More complex soil models exist. However, the added complexity means added expense in determining the material parameters and in performing the simulations. Since the "true" soil target is somewhat unknown, the additional expense was not warranted. However, using a simple model does have its drawbacks. One must experimentally determine if the model includes the necessary phenomena. Verifying these simplifying assumptions generates a cycle of testing and analysis.

The numerical model uses the SOIL AND FOAM material model from PRONTO (Taylor and Flanagan, 1987). This model treats the soil as a perfectly plastic, crushable material, where the crush pressure is a function of the volume strain, and the yield strength is a function of the pressure. The model allows the user to input crush pressure as a piecewise linear function of volume strain. The soil model expresses yield stress as a function of pressure:

$$\sigma_{yd} = a_0 + a_1 P + a_2 P^2 \tag{8}$$

For all the results in the current study, the material constants used for the SOIL AND FOAM material model are listed in Tables 13 and 14 and are based on the triaxial shear and volume-pressure tests shown in Figure 6 through 8.

The numerical model simulated the soil erosion by defining a maximum tensile pressure or 'pressure cutoff' for the soil. For the soil constitutive relation, a cutoff pressure of 0.058 MPa (8.4 psi) was used. The numerical method should support this cutoff pressure at any strain; however, the SPH method can support only a limited strain before the spacing of the particles exceeds their overlap. At this point, the SPH method will no longer support tension. Thus, the numerical process of erosion is only approximate.

Table 13. Material Properties Used in the Soil Model.

Property	Value
Density	1.393 g/cc
bulk modulus	0.000193 MPa
two mu	0.000128 MPa
a0	5.51e-02 MPa
a1	0.95
a2	0.0
pressure cutoff	-5.80e-02 MPa

Because the liquid and soil are treated as continua, the fluid will not be allowed to diffuse into the soil. Thus, the liquid and soil maintain a material interface that may not be physical. At late times, the fluid could diffuse into the soil. Here, we assume that the time it takes for the fluid to diffuse significantly into the soil is much greater than the time for the impact event.

Table 14. True Strain vs. Pressure Used in the Soil Model.

True Strain	Pressure
0.0	0.0
0.006	23924Pa
0.02	47840Pa
0.064	95760Pa
0.114	190980Pa
0.2231	349560Pa
0.24	382650Pa
0.26	574330Pa
0.27	765310Pa
1.0	14858000Pa

Numerical Results

Five different impact speeds and impact angles were considered. The strategy was to try one calculation in the center of the test matrix. If the model was successful at predicting the behavior at that speed and impact angle, then the behavior at the four corners of interest would be computed and compared with the test. This method would allow testing and analysis to complement each other. The impact speeds simulated were nominal values of 30.5 m/s, 61 m/s, and 91.5 m/s which are all within the experimental scatter in the data but are slightly different from the average experimental values of 30 m/s, 64 m/s, and 92 m/s, respectively.

Comparison of preliminary computations for the $\alpha = 45°$, $v = 61$ m/s impact with test data indicated that the predicted impact cater was much narrower than the experimental results as can be seen in Figure 18. However, the maximum depth prediction for both the crater cross-section and soil deformation was good. This calculation used the 1.27 cm thick liquid jet that did not account for air drag induced spreading that is visible in Figure 11a. The air was omitted from the numerical model. The air could be modeled using SPH elements. However, modeling this detail would add greatly to the expense of the calculation because of the very fine spacial resolution required to capture the fluid-air interface. To economically account for the fluid spreading in flight, all subsequent calculations used a 0.64 cm thick central core at full density surrounded by a 0.64 cm thick slabs at 1/2 normal density as shown in Figure 17.

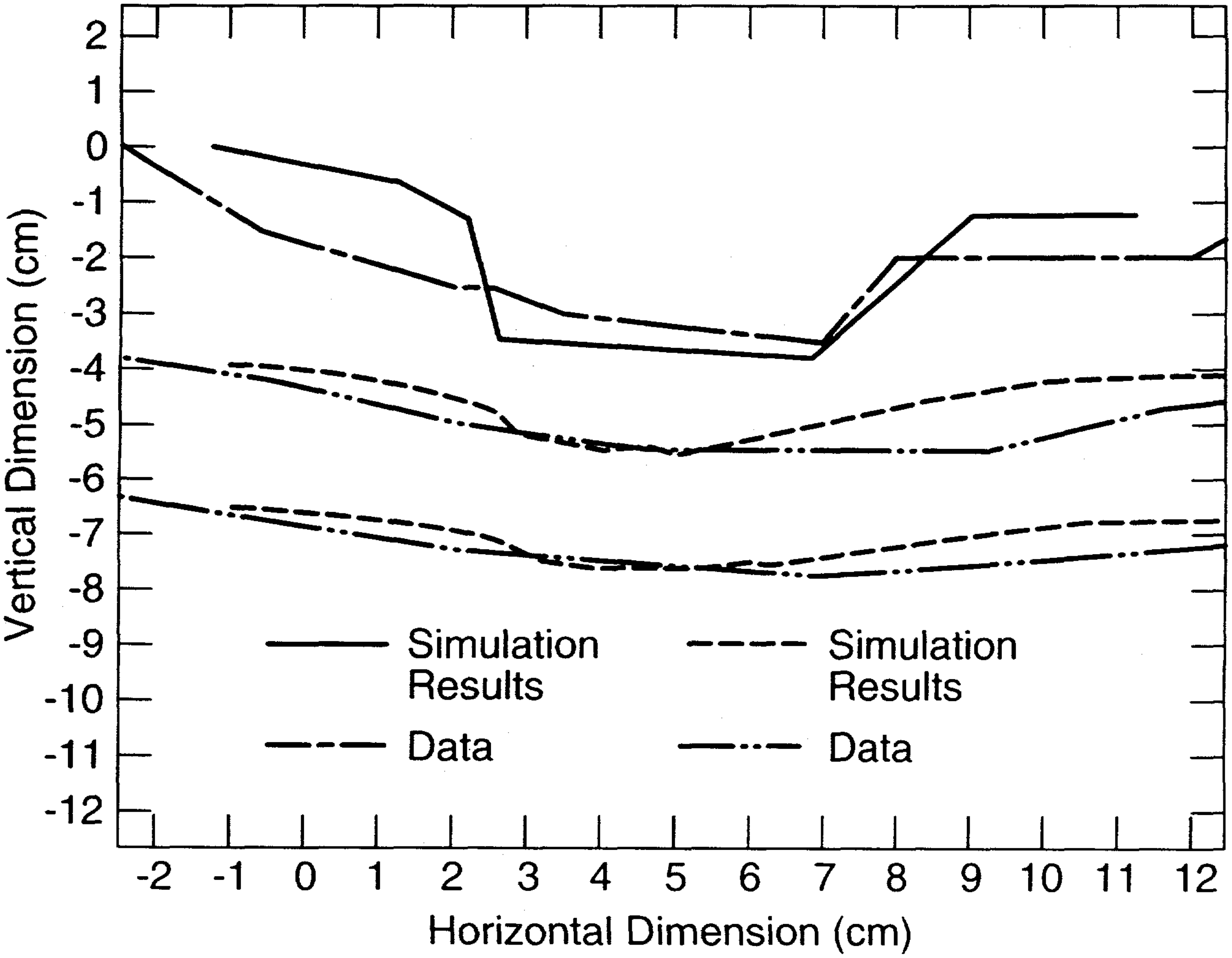

FIGURE 18. Crater Cross Section and Soil Deformation: Comparison of Test Versus Numerically Predicted Results for an Impact Angle of 45° and an Impact Velocity of 64 m/s.

A time sequence of the predicted water jet impact for the $\alpha = 45°$, $v = 61$ m/s impact is shown in Figure 19. At $t = 2$ msec the jet has impacted soil, with some of the jet rebounding. Part of the leading edge of jet has started to rebound from the soil with the trailing part of the jet still applying a crushing pressure to the soil. At $t = 4$ msec, more of the jet can be seen to be splashing out of the crater. Some soil erosion has begun.

The jet impact lasts approximately 4.0 msec. During this time, a pressure wave is transmitted through the soil, causing the soil to crush and compact. This crushing allows the liquid to penetrate into the soil, spreading as it penetrates. As the jet penetrates into the soil, a crush wave is transmitted through the soil. As the soil crushes and stiffens, the jet is deflected. This rebound causes erosion of the soil at late times. After rebound, the fluid jet becomes mixed with air and spreads, becoming a spray of fuel and soil downstream.

At late time ($t > 6$ msec), the jet momentum has changed direction. The soil crush has reached a maximum, and some elastic rebound of the soil has occurred. While the calculations could be continued to determine the motion of the soil and fluid at later times, the slow speeds of the soil and splash by-products increase the computational time required. Since the objective was to determine if the method could predict the crater size and cross-section, it was sufficient to stop the calculations at $t = 10$ msec.

Figure 20 shows a close-up of the numerically predicted water splash and crater formation for the $\alpha = 45°, v = 64$ m/s impact at $t = 1.0$ msec, $t = 5.0$ msec and $t = 10$ msec. Also shown in this figure is the distribution of volume strain. The soil directly under the impact point is the most highly crushed. The soft, unconsolidated soil is easily penetrated by the water jet. However, as the soil crushes and consolidates, the soil becomes dense and stiff and resists penetration.

The soil crush as a function of depth at different times is shown in Figure 21. Most of the crush occurs in the first few centimeters of the soil depth. The volume strain magnitude remains relatively constant until about $t = 0.5$ msec, when it drops (about 3 cm of compression).This drop corresponds to the time it takes for the fuel jet to start rebounding off the soil. After $t = 0.5$ msec, the momentum imparted to the soil is dissipated by radial expansion of the crush wave and also by soil crushing at greater depths. By $t = 3.0$ msec, the crush wave has fully dissipated. The maximum volume compaction is directly under the impact point, with the first 4 cm crushing by almost to 75% of their initial volume. The volume strain decreases linearly with depth from 4 to 12 cm, with very little crushing occurring below 12 cm.

Soil erosion was observed in the test (Figure 11b) and also observed in the numerical model (Figure 19 and 20). Soil erosion is caused by a complex process that includes: the fluid penetrating and crushing the soil; rebounding of the penetrated fluid; tensile failure of the soil; and momentum transfer from the fuel jet into the failed soil that pushes the soil downstream with the fluid. The unnatural clumping of the eroded SPH elements seen in Figure 20 is an unexplained artifact of the SPH method.

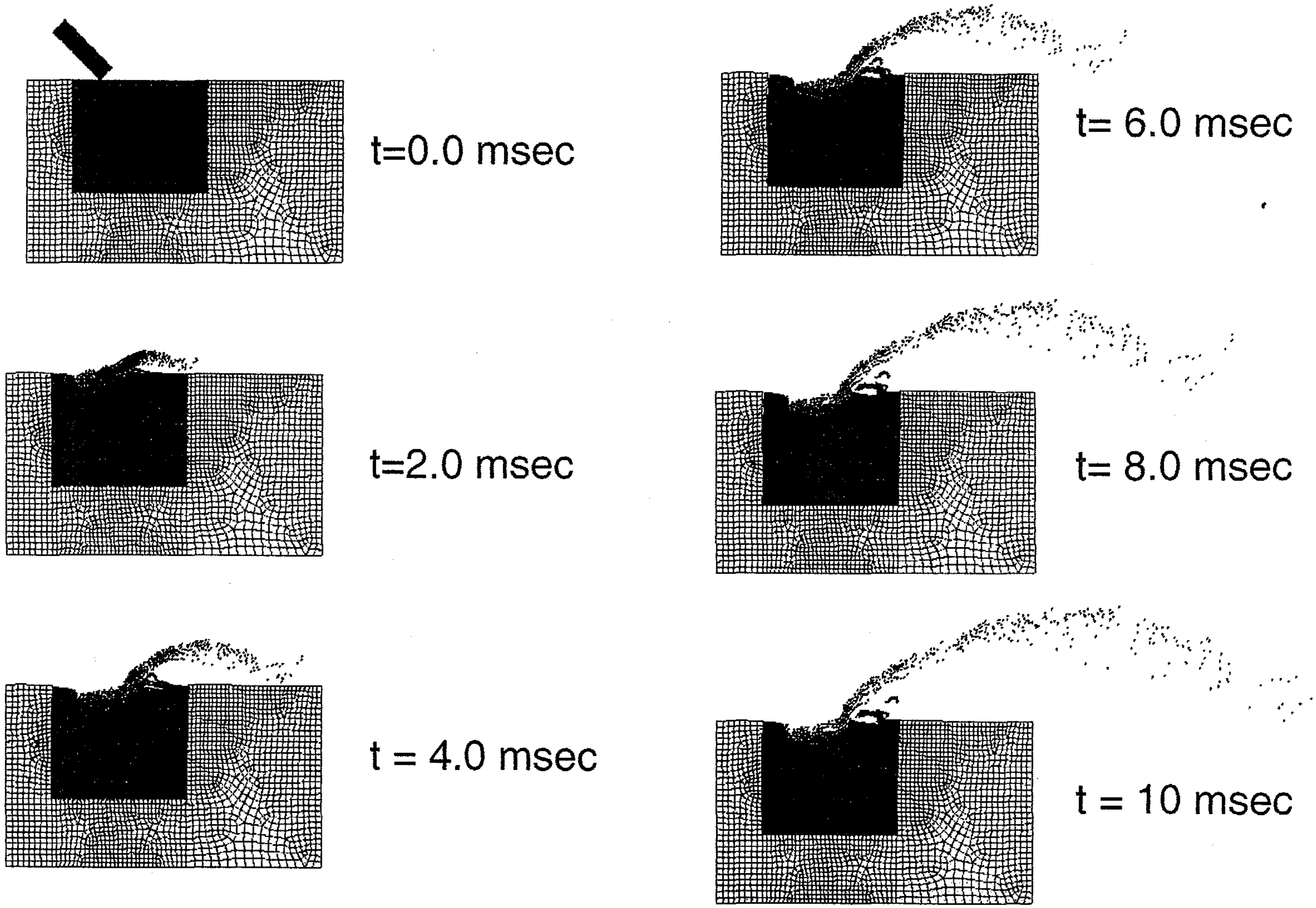

FIGURE 19. Numerically Predicted Crater Formation and Water Splash for $\alpha = 45°$ and $v = 61$ m/s

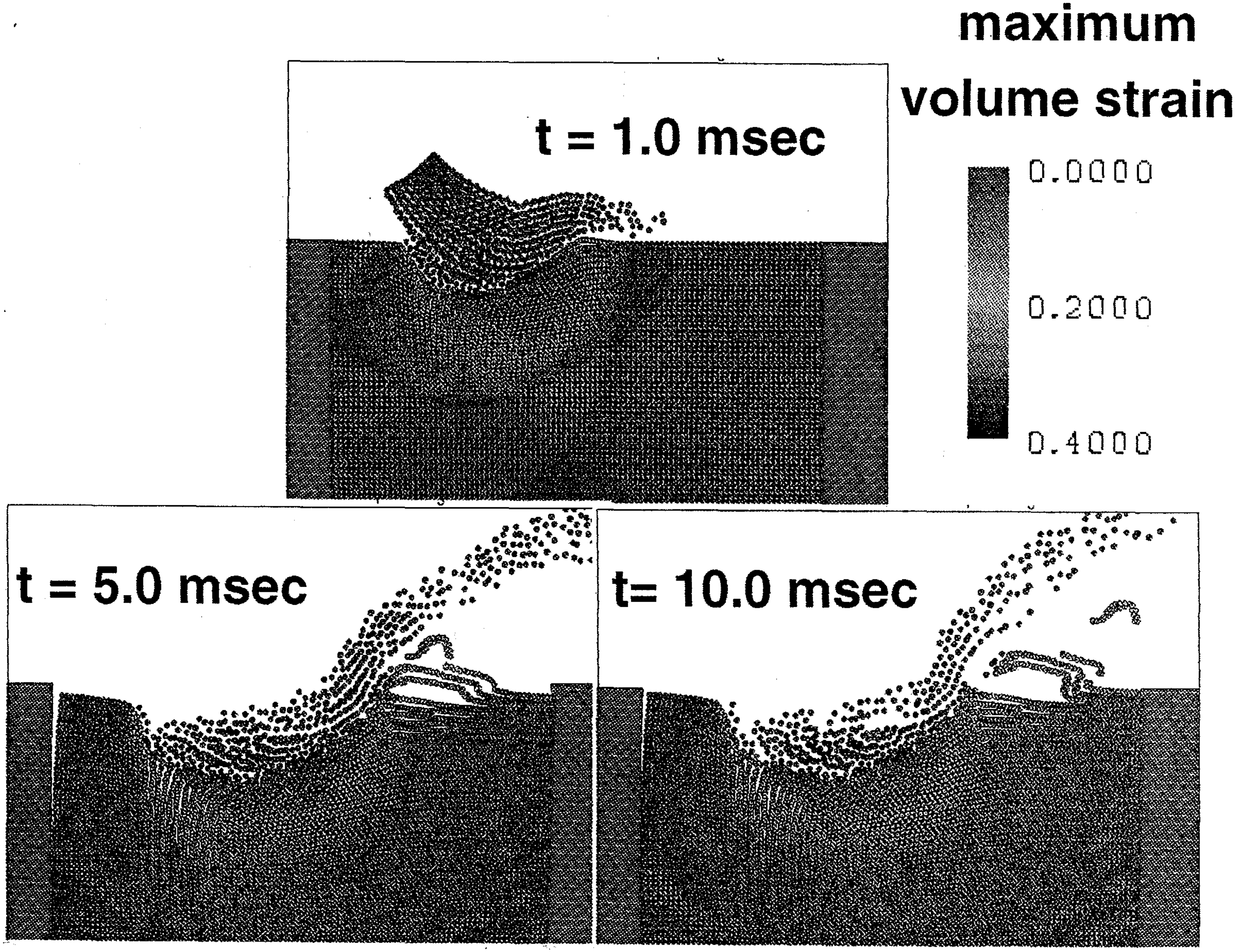

FIGURE 20. Volume Strain for $\alpha = 45°$ and $\nu = 61$ m/s.

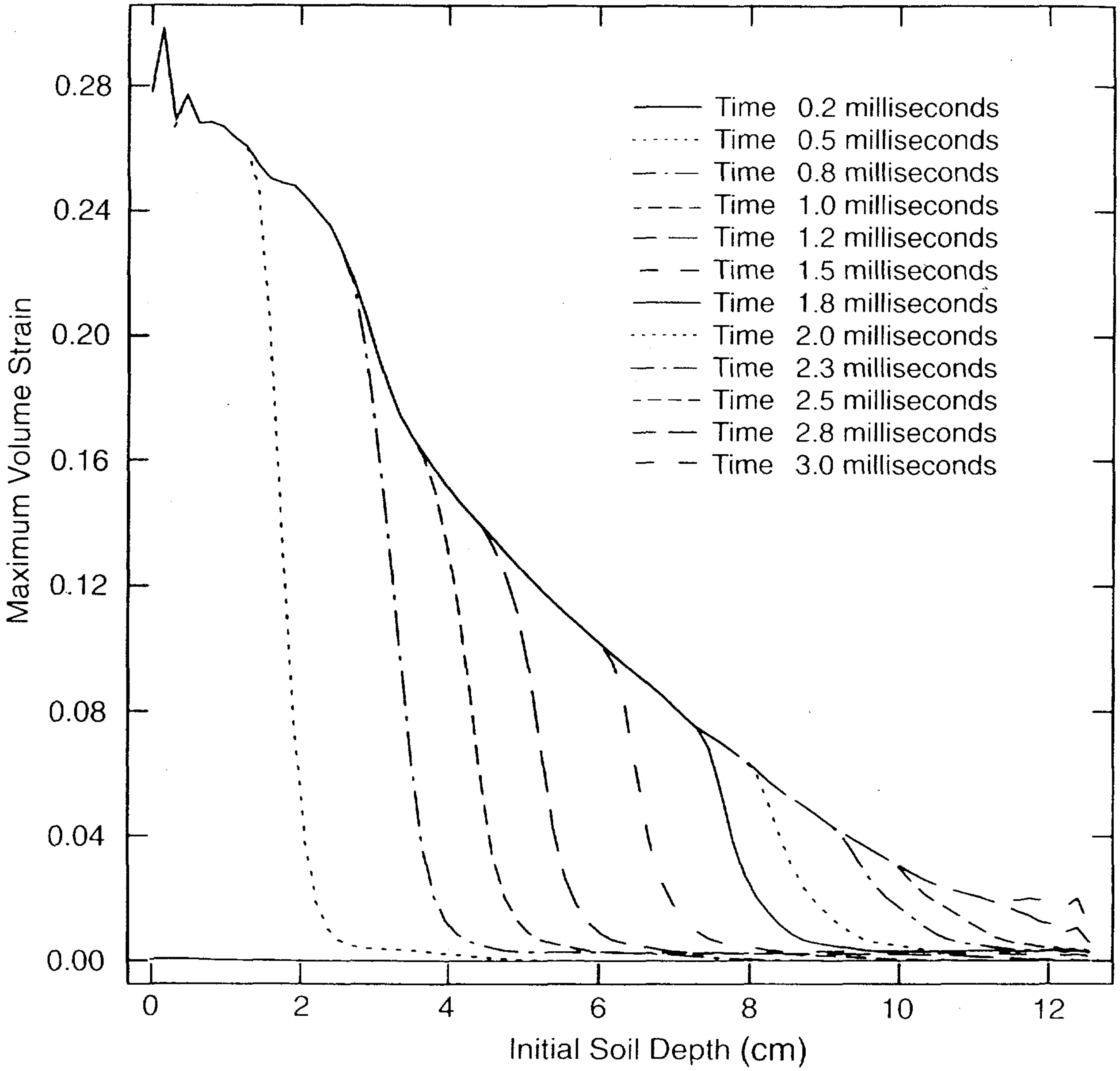

FIGURE 21. Maximum Volume Strain Plotted as Function of Initial Soil Depth for $\alpha = 45°$ and v = 61 m/s.

The water splash prediction shown in Figure 19 can be compared to the image of the liquid splash taken from the experimental setup shown in Figure 11b. While the SPH method appears to model the splash resulting from the impact, the accuracy of the results of the splash at late times is questionable because the fluid-air interactions become increasingly important. However, the average momentum neglecting the effects of air drag should be accurately modeled.

For the soil type shown here, only part of the kinetic energy is absorbed by the crushing of the soil. More energy-absorbing soils will result in more kinetic energy being removed from the fuel, causing potentially more fuel to remain in the crater. If enough energy could be absorbed by the soil, then all of the impacting fuel should remain in the crater. The volume strain required to crush a soil to lock-up is probably the greatest factor in determining the energy absorption characteristics of soil.

Predicted Crater Size.vs. Measured

The predicted crater shape and liquid splash for selected tests are shown in Figure 22. The five different combinations of impact angle and impact speed are all shown at 10 msec after impact. In each of these calculations, the fluid is still moving. The crater, however, has reach a maximum depth by this time. The $v = 90$ m/s, $\alpha = 67.5°$ impact shows the most fluid trapped in the crater at $t = 10$ msec. The $v = 30$ m/s, $\alpha = 22.5°$ impact shows almost no penetration with most of the fuel skipping off the soil surface.

The crater-cross sections are plotted in Figure 23. Each graph in Figure 23 shows the predicted crater depth as a solid line with no symbols and measured crater depth at two different cross-sections as solid lines with stars at the measurement points. Very little cratering was observed for the $v = 30$ m/s impact at $\alpha = 22°$, making crater measurement difficult. Therefore, the plots of the measured crater cross-section for this low speed impact are omitted. The measured cross-sections represent the maximum and minimum cross-section depths for the test and the difference between them is a measure of the non-two-dimensionality of the crater. The uneven profiles could be due to an edge effect of the wing, or it could be due to uneven velocity in the fuel as it impacts the soil.

In general, the numerical method predicted a penetration depth and crater width proportional to the observed crater. Higher impact velocities and higher impact angles generated deeper penetrations. However, the numerical method predicted a smaller crater cross section than was observed in the test.

Several factors could explain the differences between the test and the analysis. While every effort was made to make the soil as reproducible as possible, small variations in soil properties (moisture contact, initial density, etc.) could greatly effect its behavior. In addition, the spreading of the fuel jet as it leaves the gas gun could generate fluid density and velocity variations that were not accounted for in the analysis. The analysis were run with nominal dimensions and nominal speeds of $v = 30$ m/s, $v = 61$ m/s and $v = 92$ m/s, while in the actual experimental, the jet dimensions and impact speed varied from the

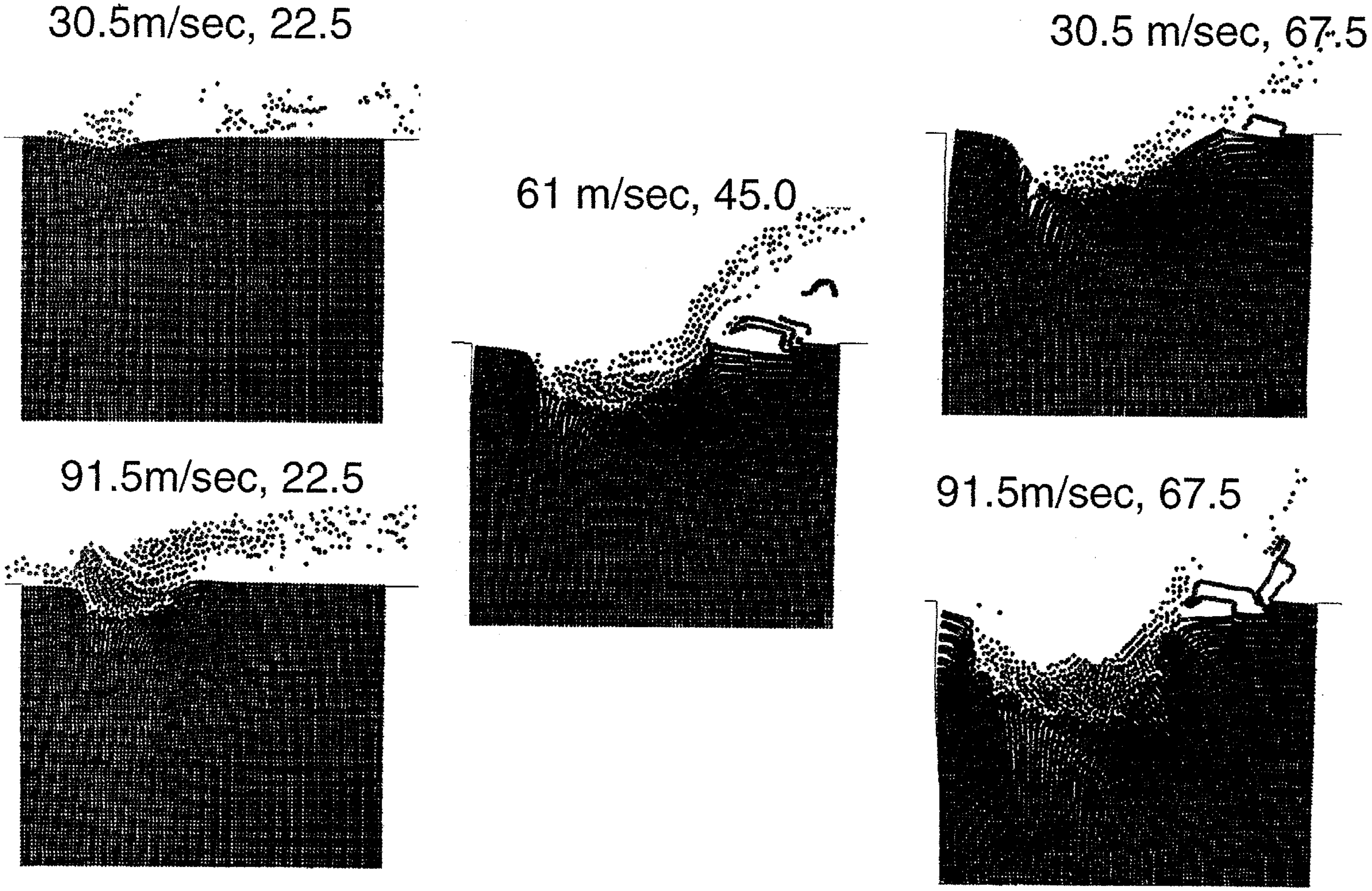

FIGURE 22. Predicted Crater Shape and Liquid Splash at 10 msec After Impact for Selected Tests.

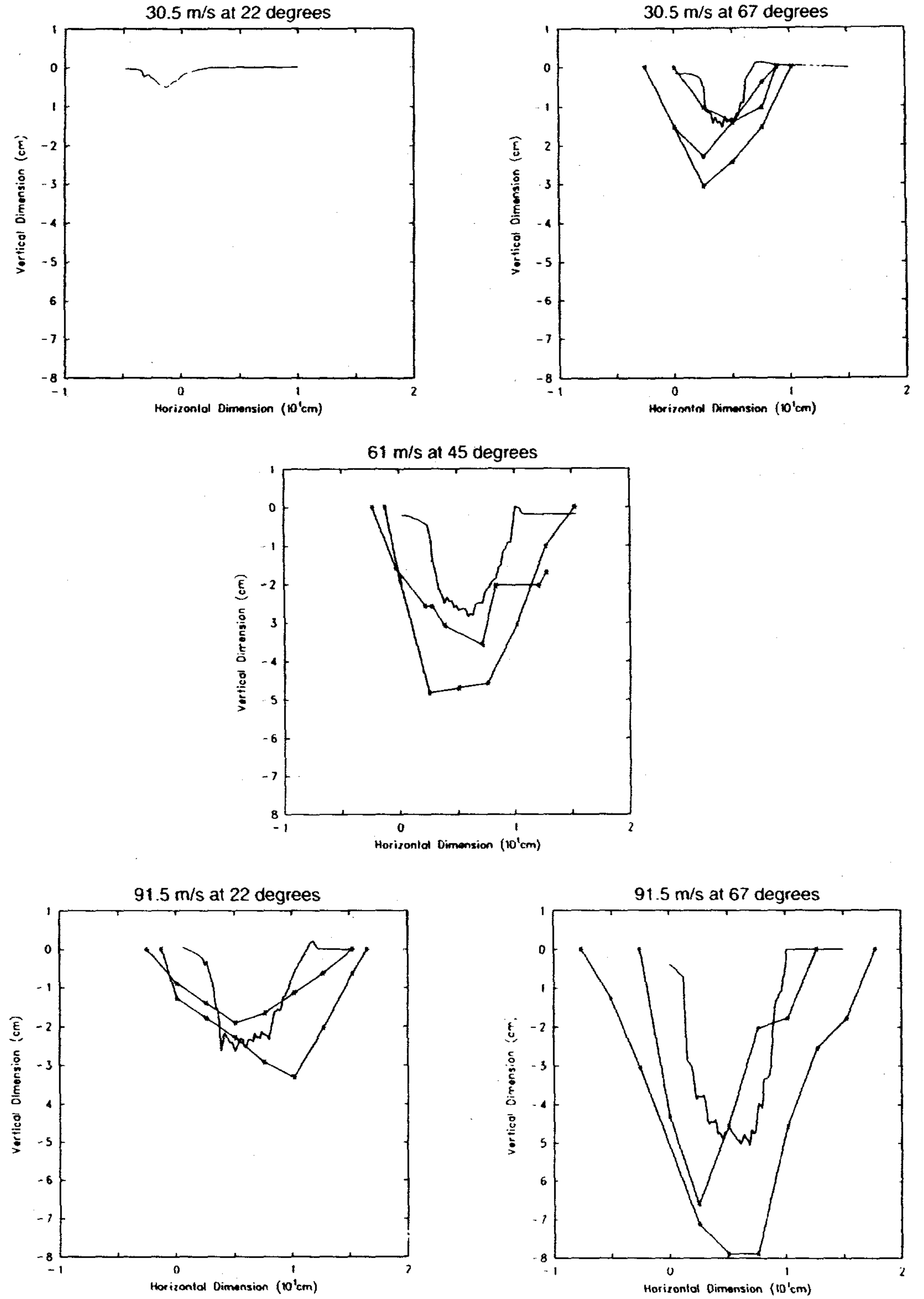

FIGURE 23. Comparison of the Predicted Crater Section Versus the Measured Crater Cross Section. ——— Prediction —✱—Data From One Cross-section (Minimum and Maximum Cross-sections Shown).

nominal. The soil model was selected based upon its computational efficiency and the economy of determining the material parameters. Other soil models that include rate effects or a better representation of the yield surface may lead to better predictive capabilities. In addition, the soil behavior was assumed to be independent of scale. Some scaling effects would be expected.

The comparison of the predicted crater sizes with the experimentally determined crater sizes illustrates that the numerical technique shows promise for being a useful tool in predicting the fuel behavior during an airplane crash. The numerical method can now be used to consider parameters, such as the effects of different soil characteristics, different fuel volumes, different fuel distributions, and the effects of the confining shell of the airplane wing.

The SPH-PRONTO coupling allows the fluid and soil to be modeled using SPH elements while the wing skin can be modeled with shell-type finite element. Figure 24 shows an example calculation using shell elements to represent a winglike container. The modeling of an actual wing structure will require a three dimensional calculation which will add considerably to the computational cost.

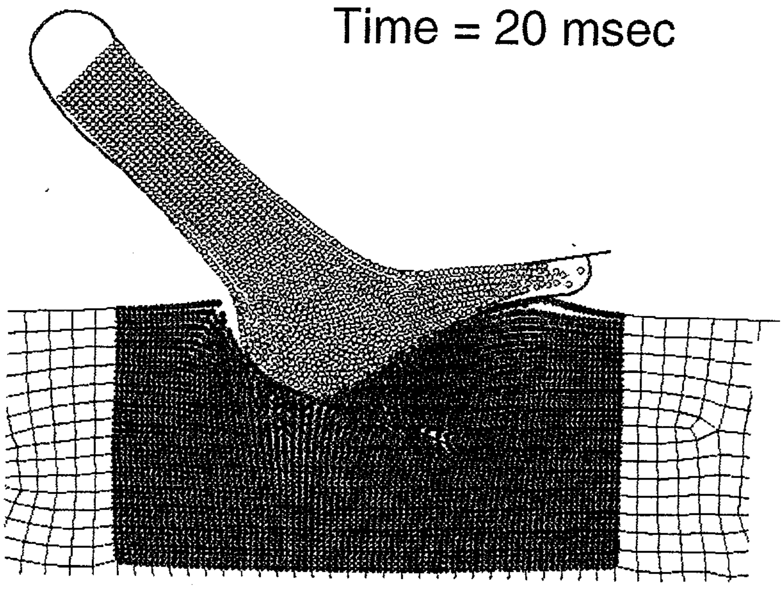

Time = 20 msec

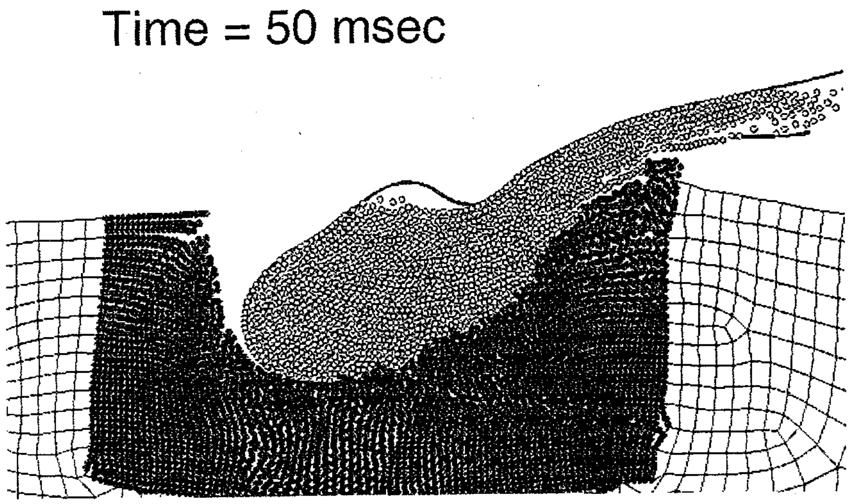

Time = 50 msec

FIGURE 24. Example Calculation at Full Scale with a Skin Modeled with Shell Elements.

Discussion

Scaling Issues

The small-scale test results from the current study indicate that there are many complicated phenomena involved in determining the size of the crater and the amount of liquid which remains in the crater. The scaling of small-scale results involving many phenomena is difficult. In the present case, the problem is aggravated by the lack of well-quantified large-scale data to use for comparison. We will attempt to use simple arguments and compare with what little data is available to obtain reasonable empirical estimates for risk assessment purposes.

Clearly, the crater size increases with increasing scale. The craters for the current set of experiments have dimensions on the order of several centimeters and impacts of aircraft can reasonably be expected to have dimensions on the order of meters. For the current tests, both the impact velocities and soil resistance characteristics of the model tests are at prototypical full scale values. Given this, and the expectation that the results from the 1/42 linear scale model would predict craters with the dimensions on the order of meters for a full scale impact, a reasonable first *assumption* is that the results will scale linearly. (There is insufficient data to support higher order assumptions in any case.) Given the complexity of the problem, this linear scaling assumption is not likely to be strictly valid. Its usefulness is based on how well it predicts full-scale data.

We are interested in comparison with data for fuel laden structures which have the same overall momentum and shape as aircraft wings. While cratering data exists for the accidental impact of large aircraft, it is unclear how much of the cratering is due to the fuselage or engines, and how much is due to the wing tanks themselves. The authors are unaware of any well characterized data for the impact of fuel laden wings into the ground.

However, while impact data does not exist for fuel laden wings, data does exist for droppable fuel tanks, e.g., napalm bomb data. In particular, the report by Edwards, 1973, contains both data and correlations for cratering due to napalm bomb drops. The bombs studied in Edward's report are 0.47 m (18 inches) in diameter and 3.3 m (10.8 ft) long. They have aluminum skins between 1.25 mm and 1.50 mm (0.05 to 0.06 inch) thick. They are loaded with 379 liters (100 gallons) of fuel. The empty weight is 40 kg (88 lbs) and the full weight is about 395 kg (870 lbs).

For comparison, the baseline proportions for fully loaded wing tanks on the C141 have been estimated as 0.49 m : 3.52 m : 51.0 m for thickness:chord:span (Tieszen, 1995). The length and diameter of the bombs are virtually identical to the average wing chord and thickness for the C141 fuel tanks. The primary difference between the bombs and the C141 aircraft wing tanks is that the bombs are essentially axisymmetric cylindrical bodies while the wing tanks are essentially two-dimensional planar bodies.

The craters formed by an impacting cylindrical jet and an impacting planar jet will be different in the spanwise direction of the planar jet. However, at the center of each jet, the differences in the crater formed along the line of impact between the two jets will not necessarily be large. In general, one would expect that the two-dimensional planar jet would produce a slightly deeper crater because spanwise momentum is not lost by the planar jet except near the edges.

The soil conditions in Edward's 1973 report are also characterized. The napalm bomb tests were conducted at Range 52 of Eglin AFB. The soil is described as "sandy" with a dry density of 1590 kg/m^3 (100 lb/ft^3). The moisture content of the soil was not recorded but it was noted that rain was fairly frequent at the range and the moisture content would be expected to vary widely. The variation in moisture content is noted as a probable cause in the scatter of the crater formation data from the napalm bomb drops.

As noted earlier, the soil for the current study is a sand/clay mixture. It has a dry density of 1390 kg/m^3 (86.6 lb/ft^3) and a moisture content of 6.3%. The differences between the soil in the Eglin tests and the current tests indicate that the Eglin soil is "harder". The soil compressibility decreases for sandy soils, higher dry soil densities, and for higher moisture contents. The craters formed by the Eglin tests therefore are expected to be smaller than would be predicted by the data from the current series of tests.

The napalm bomb tests reported in Edwards, 1973, were carried out at impact velocities between 110 m/s and 250 m/s for impact angles between 7° and 55°. Twelve data points are available for unfinned bombs and 57 data points are available for finned bombs. The data available for each test include estimates of the impact angle, impact velocity, crater breadth (length along impact axis), crater width, crater depth, and an estimate of crater volume. Comparison will be made with the finned data only. These were noted as being less likely to have entered the ground tumbling and have generally deeper craters.

Crater Breadth

By nondimensionalizing the crater breadth in the napalm bomb data with the length of the weapon (3.3 m), the data from the current study (Table 9) and the napalm bomb data can be directly compared. The results are shown in Figure 25 as a function of the normal impact velocity, V_{normal} (m/s), (= $V \sin\alpha$ where V is the impact velocity and α is the impact angle).

Also shown in Figure 25 are the mean values of the data from the current study (Equation 3) and the napalm bomb data. The mean of the napalm bomb data is given by

$$\frac{B}{C} = 0.9 \pm 0.5 \quad . \tag{9}$$

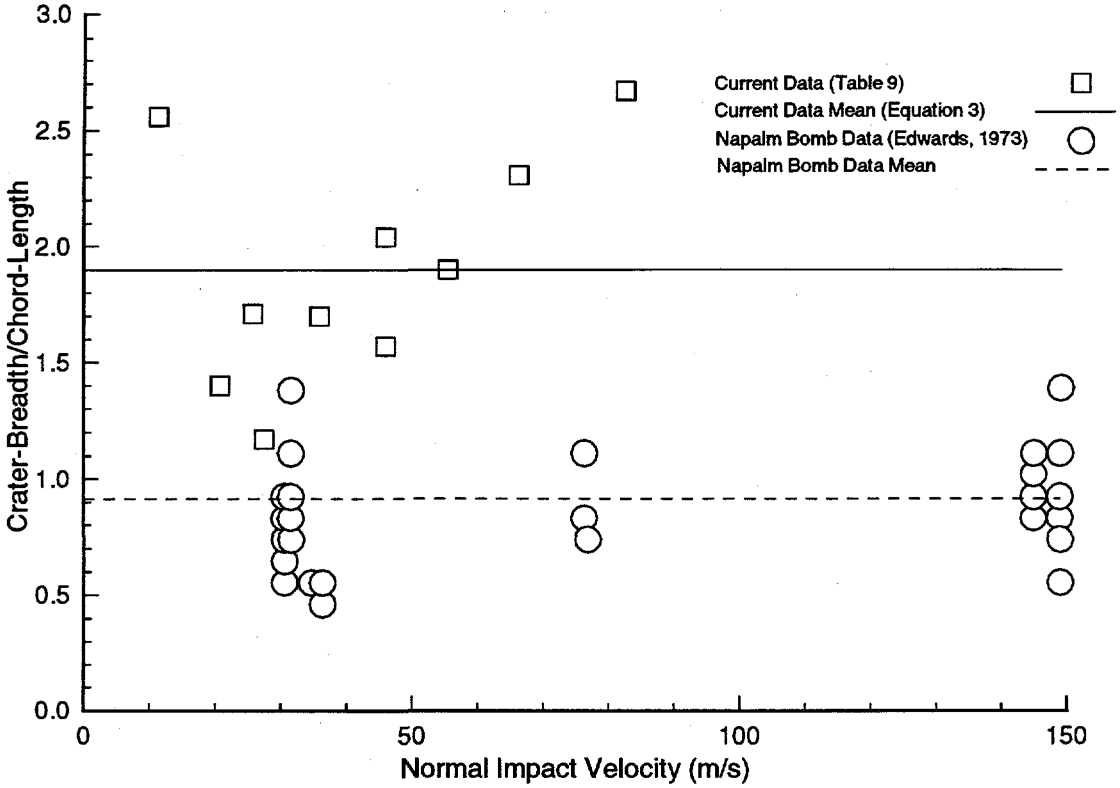

FIGURE 25. Comparison of the Data From This Study with the Napalm Bomb Data of Edwards, 1973, for Crater Breadth. For the current study, Chord-Length equals the wing chord (8.4 cm). For the napalm bomb study, Chord-Length equals the weapon length (3.3 m).

The mean of the current data is about 2.1 times the mean of the napalm bomb data, and therefore, the use of Equation 3 would overpredict the napalm data by a factor of 2.1. This is anticipated since the soil conditions for the napalm bomb study will result in smaller cratering for a given impact than the soil conditions in the current study. Further, the napalm bomb is cylindrical rather than planar. The difference may also be due to drag induced spreading of the liquid jet in the current study due to lack of confinement which did not occur in the napalm bomb tests. Since the soil at Eglin is relatively "hard" and the soil in the current tests is relatively "soft", it can reasonably be expected that the crater breadth for a C141 wing-tank impact would fall within the bounds of the two studies.

Crater Depth

By nondimensionalizing the crater depth in the napalm bomb data with the length of the weapon (3.3 m), the data from the current study (Table 8) and the napalm bomb data can be directly compared. The results are shown in Figure 26 as a function of the normal impact velocity, V_{normal} (m/s).

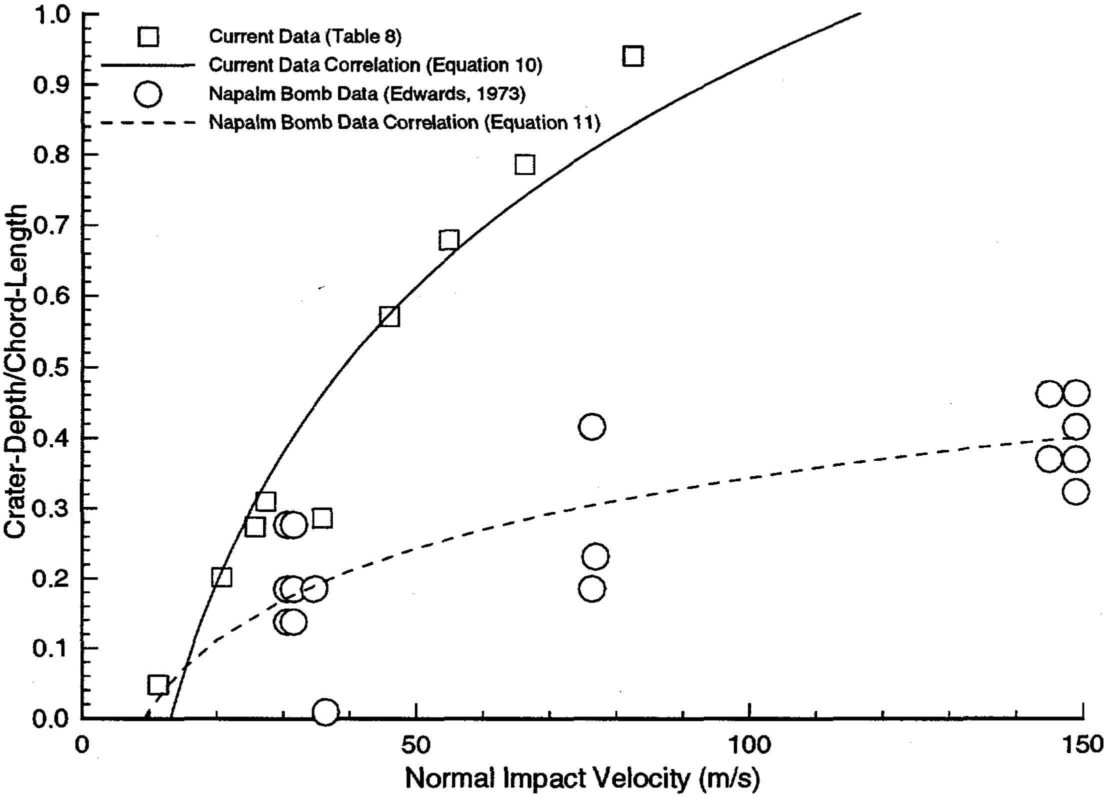

FIGURE 26. Comparison of the Data From This Study with the Napalm Bomb Data of Edwards, 1973, for Crater Depth. For the current study, Chord-Length equals the wing chord (8.4 cm). For the napalm bomb study, Chord-Length equals the weapon length (3.3 m).

Also shown in Figure 26 are correlations from the current study and the napalm bomb study. For the current study, a correlation of the crater depth data gives a correlation coefficient (R^2) of 0.92 for the form

$$\frac{D}{C} = -1.18 + 0.458 ln(V \sin\alpha) . \qquad (10)$$

The crater-depth/wing-chord, *D/C,* in Equation 10 is dimensionless, the impact velocity, *V*, is in m/s, and the impact angle, α, is in degrees. For the napalm bomb study, a correlation of the crater depth data gives a correlation coefficient (R^2) of 0.80 for the form

$$\frac{D}{C} = -0.32 + 0.144 ln(V \sin\alpha) . \qquad (11)$$

The crater-depth/wing-chord, *D/C,* in Equation 11 is dimensionless, the impact velocity, *V*, is in m/s, and the impact angle, α, is in degrees.

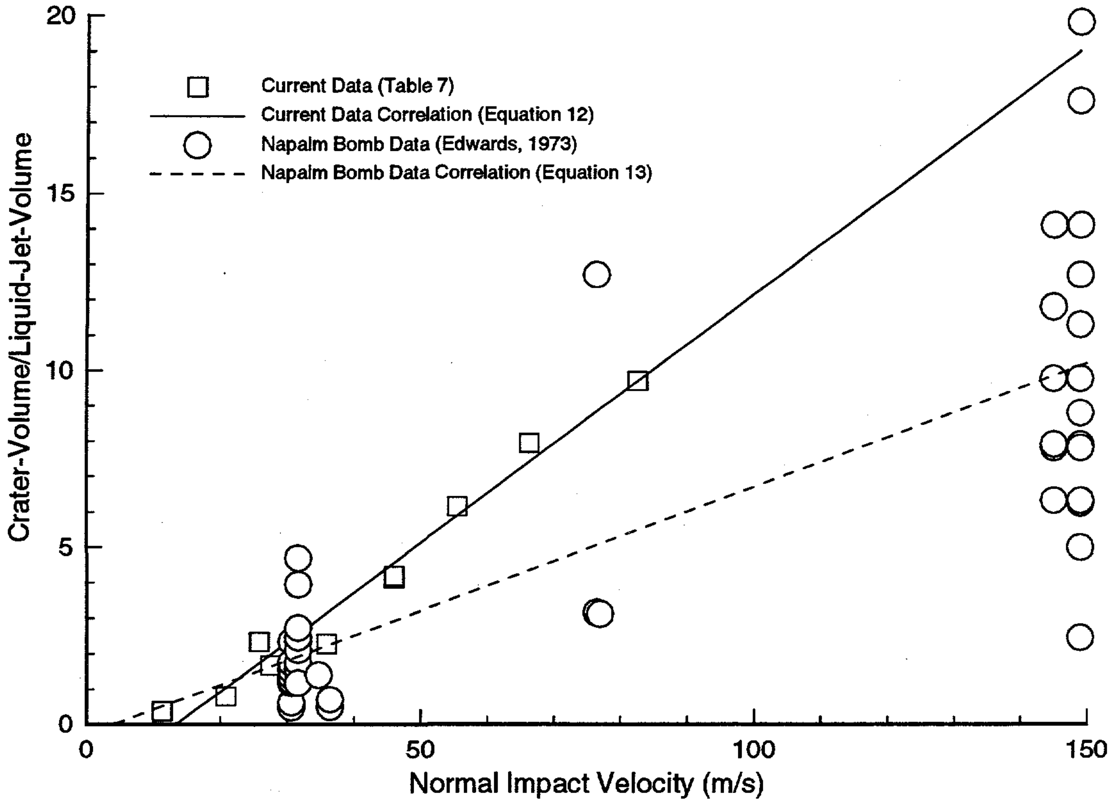

FIGURE 27. Comparison of the Data From This Study with the Napalm Bomb Data of Edwards, 1973, for Crater Volume. For the current study, Liquid Jet Volume equals the wing volume (380 cc). For the napalm bomb study, Liquid Jet Volume equals the weapon volume (0.408 m^3).

As with the crater breadth data, the crater depth for the napalm tests would also be overpredicted by the current data and Equation 10. The largest uncertainty is at the highest normal impact velocities and is about a factor of 3 at those velocities. It can be expected that the crater depth for a C141 wing-tank impact would fall within the bounds of the two studies.

Crater Volume

By nondimensionalizing the crater volume in the napalm bomb data with the volume of the weapon, the data from the current study (Table 7) and the napalm bomb data can be directly compared. The volume of fuel in the napalm bombs was given in Edwards, 1973, as 0.379 m^3. The data sets are compared in Figure 27 as a function of the normal impact velocity, V_{normal} (m/s).

Also shown in Figure 27 are the correlations for the current data and the napalm bomb data. For the current study, a correlation of the crater volume data gives a correlation coefficient (R^2) of 0.97 for the form

$$\frac{\vartheta_{crater}}{\vartheta_{jet}} = -1.88 + 0.140 V \sin\alpha . \tag{12}$$

In Equation 12, the crater-volume/incident-jet-volume,$\vartheta_{crater}/\vartheta_{jet,}$ is dimensionless, the impact velocity, V, is in m/s, and the impact angle, α, is in degrees. For the napalm bomb study, a correlation of the crater depth data gives a correlation coefficient (R^2) of 0.55 for the form

$$\frac{\vartheta_{crater}}{\vartheta_{jet}} = -0.25 + 0.0649 V \sin\alpha . \tag{13}$$

The crater-volume/incident-jet-volume,$\vartheta_{crater}/\vartheta_{jet,}$, in Equation 13 is dimensionless, the impact velocity, V, is in m/s, and the impact angle, α, is in degrees.

The average crater volume for the napalm tests would be overpredicted by using the data from the current study. The largest uncertainty is at the highest normal impact velocities and is about a factor of 2 for the average crater volume at those velocities. By a simple product of crater breadth and crater depth, one would expect the crater volume of the napalm bomb tests to be substantially overpredicted by the current data since crater breadth is overpredicted by a factor of two and crater depth by a factor of three. The reason that the crater volume is off by only a factor of two is that the spanwise width of the crater changes significantly in the napalm bomb studies while it is relatively constant in the current study. This difference is due to the difference between the cylindrical geometry of the napalm study and the planar geometry of the current study.

It is interesting to note that the correlation coefficient for Equation 12 is very high (0.97) for a linear correlation with normal impact velocity. Edwards, 1973, also noted a high correlation with respect to normal impact velocity. (His correlation coefficient is lower,0.55, due to the scatter of the napalm bomb data which he attributes to varying soil conditions.) The linear dependence on velocity indicates that the crater formation processes of material compression and erosion are momentum dominated. This is not necessarily intuitive since a kinetic-energy/work relationship would yield a depth that was dependent on the square of the normal impact velocity.

Since the current data fall within the scatter of the napalm bomb data, and the current data represents "soft" soil conditions while the napalm bomb data represents "hard" soil conditions, it is reasonable to expect that the crater volume for a C141 wing-tank impact would fall within the bounds of the napalm bomb study.

Liquid Pooling Fraction

Quantitative data for the amount of fuel remaining in the crater from napalm bomb impact tests is not available. However, qualitative descriptions in Edwards, 1973, compare very favorably with the data from the current study given in Table 6. As noted in the introduction section of this report, Edwards, 1973 attributes the following quote to a Lt. Royer on napalm bomb development tests, "Impact craters 1.5 - 5 feet (0.5 - 1.7 m) deep and 5 to 14 feet (1.7 - 4.3 m) in diameter, restricted flame fuel dissemination and ignition.... Thirty to 50% of the flame fuel from each fire bomb burned in impact craters (for 8 - 100 minutes)..." Further, for shallow craters, Edwards, 1973, notes that "When fire bombs are released in the skip bomb mode, e.g., at 200 knots (100 m/s) from 100 feet (30 m) in straight and level flight, little if any unburned incendigel is likely to adhere to the sand at the point of impact. Evidently, practically all of the 100 gallons (379 l) of incendigel in the canister is thrown out immediately on impact."

The percent pooling data in Table 5 can be empirically curve fit. A correlation of the percent pooling data gives a correlation coefficient (R^2) of 0.77 for the form

$$PP = -0.01 + 0.43\sin\alpha . \tag{14}$$

PP is the percent pooling as given in Table 5. Table 15 gives the predictions of Equation 14 for the conditions in Table 5.

Table 15. Equation 14 Predictions for Percent of Initial Mass Remaining in the Crater After Impact

		Impact Angle (Degrees)		
		22.5	45	67.5
Impact Velocity (m/s)	30	16%	29%	39%
	64	16%	29%	39%
	92	16%	29%	39%

Since qualitative comments concerning the napalm bomb data match the results from the current study, it can be reasonably expected that the percent pooling that would result from a C141 wing-tank impact would fall within the bounds of the current study. Since the equivalent liquid layer thickness is also dependent on the crater width and breadth, and the crater breadth may be overpredicted by a factor of two, then the equivalent liquid layer thickness may be underpredicted by a similar factor.

Scaling Summary

The parameters of interest to a weapons safety assessment, namely the size of the pool, the location relative to the impact point, and the amount of fuel in the pool, can reasonably be expected to fall within the current data and the napalm bomb data, with an uncertainty of about a factor of two to three. However, it should be kept in mind that *proof* has not been demonstrated. The current study is the first of its kind to the authors knowledge, linear geometric scaling was *assumed*, and well characterized data for wing impacts does not exist. Larger scale test results including limited full scale testing would improve the confidence that the reasonable expectations based on the arguments presented here are indeed fulfilled.

Fuel Distribution in Wing Tanks

At the outset it was assumed that the fuel distribution in the wing tanks of the aircraft prior to impact would have little or no impact on the fuel dispersal parameters of interest. For convenience, the fuel distribution was assumed uniform and rectangular. While it was never a design goal of the experiments to test this assumption, sufficient data was taken during the development of the test apparatus that the assumption can be.

The wing design in Figure 4a was tested at the 30 m/s, 64 m/s, and 92 m/s levels. At 30 m/s, it performed well but at the higher velocities, it was discovered that the strongback failed on initial acceleration. The craters formed by this wing design were not uniform as shown in Table 16. The variability for the wing design in Figure 4a was not random, but the craters formed were much deeper at the edges than at the center. This pattern suggests that the leading edge of the wing collapsed in the center on initial acceleration and the liquid primarily emerged from the wing edges. Somewhat fortuitously, this represents a likely distribution of fuel in flight in a C141 aircraft. The extended range tanks are between the main tanks and the auxiliary tanks, and are less often used.

Table 16. Variation in Maximum Crater Depth Between Wing Designs in Figure 4a&b. Depth variability is given by +/- 2s, where s= (Dmax-Dmin)/2(Dave). Dave, Dmin and Dmax are the 4 section average, minimum and maximum crater depths, respectively. Average is over 64 m/s and 92 m/s data.

Wing Design	s
Figure 4a	51%
Figure 4b	22%

In spite of the differences in uniformity of the liquid jet impinging on the ground, the percent of liquid remaining in the crater and the overall volume of the crater were not strongly affected except at the shallowest impact angle and lowest impact velocity. These results are given in Tables 17 and 18 respectively

Table 17. Comparison Percent of Fuel Remaining in the Crater for Uniform and Nonuniform Jets.

			Impact Angle (Degrees)		
			22.5	45	67.5
Impact Velocity (m/s)	64	Uniform	14%	38%, 31%	34%
		Nonuniform	7%	35%	35
	92	Uniform	10%	37%	38%
		Nonuniform	8%	31%, 34%	49%

Table 18. Comparison of the Crater-Volume/Jet-Volume for Uniform and Nonuniform Jets.

			Impact Angle (Degrees)		
			22.5	45	67.5
Impact Velocity (m/s)	64	Uniform	2.3	4.2, 4.1	6.2
		Nonuniform	1.1	3.8	5.6
	92	Uniform	2.3	7.9	9.7
		Nonuniform	2.5	6.5	8.6

The worst case comparisons are about a factor of two at the lowest velocity and impact angle. The average difference is much less for both the liquid remaining and the crater volume. These results indicate the actual fuel distribution in the wing at impact will not strongly affect the variables of interest to a weapon-system-safety-assessment (WSSA).

Unresolved Issues

The effect of different soil types has not been resolved. In the current study, a single soil type was tested. While comparison with the napalm bomb study indicated that the effect of soil characteristics could be reasonably be bounded, the critical soil characteristics controlling the crater formation or liquid hold-up were not identified. For comparison with the napalm data, it was *assumed* in all the empirical correlations that linear geometric scaling was valid and is represented by the left-hand side of each correlation as a ratio of geometric scales, i.e., length/length or volume/volume. The right-hand side of the equations have been left in their dimensional form. This has been done because the physical mechanisms associated with cratering have only been qualitatively defined by this study.

Quantitative descriptions of soil compression versus soil erosion were recorded for each test in Appendix A, but the mechanisms were not quantified in terms of the soil properties. The smooth particle hydrodynamics technique has permitted us some understanding of the processes, but a simple quantitative description was not derived. The volume strain required to crush a soil to lock-up is probably the greatest factor in determining the energy absorption characteristics of soil. However, the fact that the crater volume is proportional to normal impact velocity rather than normal impact kinetic energy indicates that a simple work-kinetic energy balance is not likely to be sufficient to describe the role of the soil properties in determining the impact characteristics. Further simulation with the SPH/ PRONTO model and validation by experiments with different soil characteristics would be required to fully understand the effect of soil properties.

The soil used in the current study was not compacted to the naturally occurring soil density. In this sense it is somewhat conservative, especially in comparison to the wet sandy soil used in the napalm bomb studies. However, it does not represent a bounding case. It is possible to have an aircraft impact into a soil which has been disturbed and has a soil density less than that tested. In this case, the crater will likely be bigger. Without a quantitative description of how the soil characteristics affect cratering, it is not possible to quantitatively bound the resulting crater size.

The effect of the wing structure has not been resolved. In the current study, the wing structure has been ignored. The wing structure introduces three effects not considered: confinement, strength, and additional momentum. The lack of confinement in the current study may be one reason that the crater breadth overpredicts the napalm results by as much as a factor of two. Without confinement, the liquid jet begins to broaden due to aerodynamic drag. This effect has be minimized in the current study by stopping the wing as close as possible to the soil surface. Still, the edge of the jet has broadened by a factor of two to three at impact, spreading the impact over a larger breadth than if confined.

The current study also ignores the structural strength of a C141 wing. In general, this assumption is made by necessity, as it is difficult to create a small-scale structural model of the wing that can survive the acceleration loads. Accident data, including the B52 crash at Fairchild (Moya, 1994), indicate that aerostructures are relatively weak compared to solid surfaces such as the ground and will fragment quite readily. The napalm bomb tests also confirm this observation. However, the quantitative impact of the structural strength of the wing on the cratering and the fuel dispersal processes is not known. It is *assumed* to be small.

In the current study, the momentum (or kinetic energy) is due to the mass of the water alone. In a C141 impact, there will also be momentum due the mass of the wing structure. This added momentum can be expected to assist in the cratering process. In the case of the napalm bomb data, the dry bomb mass was about 10% greater than the mass of fuel. Because of its low mass relative to the fuel, the mass of the bomb was ignored for comparisons in the last section. For a C141, the mass of the wing structure (minus the engines and pylons, which will dig their own craters) may need to be taken into account, particularly for small fuel loads.

The effect of not considering the wing mass is partially offset by using water as a fuel simulant in the tests. Water is about 20% denser than jet fuel. Therefore, for a given jet volume, the water jet will have a 20% greater momentum on impact. It follows that the prediction based on the current data would overpredict the cratering of a fuel jet only. In the napalm bomb tests, if the dry bomb mass is converted to an additional fuel volume for cratering purposes, then average density of the bomb will be essentially that of water. The result would be a decrease in the napalm bomb data and correlation of about 10%. If the dominant physical mechanism for cratering and fuel dispersal is momentum, then the only fluid property of importance is the density and other property differences between water and fuel such as surface tension can be ignored.

The effect of a partial fuel load on the aircraft at impact has not been resolved. The current study also assumes that the C141 wings are fully loaded. In general, it is desirable to extrapolate the current results to any fractional fuel load. With a full fuel load, the average chord to thickness ratio is fixed at a value of about 7. At impact if the fuel is assumed to slosh forward prior to wing failure, then the chord to thickness ratio will decrease with decreasing fuel load. The effect of a change in chord to thickness ratio has not been studied. The napalm bomb data has nearly an identical ratio as a C141 wing tank.

If it is *assumed* that changes in jet geometry for a given mass are relatively small, then partial fuel loads can be handled by defining the appropriate chord length. For example, if the chord to thickness ratio at full load is 7, then the same ratio is 3.5 at a 50% fuel load. The resultant crater depth, breadth, and volume will then be predicted by the empirical correlations in this report to also be 50% of the full fuel load values. The uncertainty in these predictions cannot be determined from the current data, but the trend will be correct. Clearly, a half-full wing will not produce a crater as large as a full wing for a given impact velocity and impact angle.

The effect of non-zero pitch, yaw, and roll angles at impact has not been resolved. The current study assumes that the pitch, yaw, and roll angles of the aircraft are all zero at impact. The wing is assumed to hit the ground with the leading edge forward. If the wing impacts such that the bottom of the wing hits first, then geometry of the impact is quite different than that assumed. In the current context, it would be a 'jet' with a thickness that is 5.6 times its chord length, rather than a jet with a chord length 5.6 times its thickness as in the current study.

The purpose of the current study in the context of the weapon safety assessment program is to determine the initial conditions for the pool fire scenario. The primary variable of interest to a WSSA program is the time-integrated heat-flux on a weapon system due to the resultant pool fire. The uncertainties in each of these processes needs to be addressed. In the current study, there are several parameters that can have on the order of a factor of two uncertainty. These include the area coverage, effective liquid layer thickness, the position of the crater relative to the point of impact, and the effect of non-uniform spatial distribution prior to impact and after impact on the ground.

The uncertainty in the duration of a dirt fire may equal or exceed the uncertainties in the initial conditions identified in this study. The principal reason for this uncertainty is the effective burn rate of a dirt fire could potentially be more than an order of magnitude less than predicted by a pool fire on water. For a large pool fire on water, the average burn rate is about 6 mm/min. This is not necessarily the minimum flow rate to sustain combustion. In fact there is evidence to suggest a large vapor dome is created because the evaporation rate is so high. In contrast, a dirt fire may have a lower evaporation rate which will result in a longer fire. Due to the porosity of the soil, some of the fuel will be lost into the ground and will not be available for combustion. However, under the right conditions, the soil can act as a wick (as on a candle), and draw a significant portion of the fuel back out of the ground. The resulting duration of the fire could be more than an order of magnitude longer than expected from current pool fire tests. Evidence from tests conducted at the Naval Air Warfare Center at China Lake for the Defense Nuclear Agency program indicate that this may indeed be the case. Container tests C1 & C2 (7/31/94 & 8/23/94, respectively) had sand boxes that continued to burn for about 3 hours on nominally 18 minute pool fires (Gritzo, 1994).

Conclusions

Tests results show that the percent of fuel in the crater ranges from near zero for grazing impacts to 25% - 50% for high angles of impact. The resultant crater breadth is approximately twice the wing chord, its span is approximately the wing span, and the resultant crater depth is a fraction of the wing chord. The specific crater dimensions depend on the impact velocity and impact angle. The equivalent liquid layer thickness is from 1% to 4% of the wing chord in depth depending on the impact velocity and impact angle. The position of the maximum depth of the crater forward of the wing impact line is a fraction of the wing chord.

For the soil type tested, only part of the kinetic energy is absorbed by the crushing of the soil. More energy-absorbing soils will result in more kinetic energy being removed from the fuel, causing potentially more fuel to remain in the crater. If enough energy could be absorbed by the soil, then all of the impacting fuel should remain in the crater. The volume strain required to crush a soil to lock-up is probably the greatest factor in determining the energy absorption characteristics of soil.

The current test results and napalm bomb data that have been normalized by the appropriate weapon dimensions are found to be similar. The percent fuel in the crater is found to compare favorably, but the crater dimensions are overpredicted by a factor of two to three. This result can be explained by the differences in jet geometry and soil characteristics between the napalm bombs and the current study. All factors favor larger craters in the current study. Since the napalm bombs used for comparison have nearly the same chord and thickness as the C141 wing, it is reasonable to expect that a C141 wing tank impact would fall within or between the data sets.

Unresolved issues are identified in the report. The current study is the first of its kind to the authors knowledge, linear geometric scaling was *assumed*, and well characterized data for wing impacts does not exist. Larger scale test results including limited full scale testing would improve the confidence that the reasonable expectations based on the arguments presented in the report are indeed fulfilled.

Uncertainty estimates for the tests indicate that there are several parameters that can have on the order of a factor of two uncertainty. These include the area coverage, effective liquid layer thickness, the position of the crater relative to the point of impact, and the effect of non-uniform spatial distribution prior to impact and after impact on the ground. Since, the duration of a pool fire is directly proportional to the depth of the liquid layer, a factor of about 2 in uncertainty will exist in the duration of the fire. Not addressed in the current study, but also contributing to the uncertainty in the duration of a pool fire is the phenomenology of burning above a fuel-soaked soil surface. Uncertainties from a lack of understanding of the extent to which wicking of the fuel occurs could exceed the uncertainties identified in the current study.

The comparison of the predicted crater sizes using PRONTO/SPH with the experimentally determined crater sizes illustrates that the numerical technique shows promise for being a useful tool in predicting the fuel behavior during an airplane crash. Qualitatively, the splash, erosion, and soil compression phenomena are all predicted. Quantitatively, the numerical method predicted a smaller crater cross section than was observed in the tests.

References

Attaway, S.W., 1990, "Update of PRONTO 2D and PRONTO 3D Transient Solid Dynamics Program," SAND90-0102, Sandia National Laboratories, Albuquerque, NM

Attaway, S. W.; Heinstein, M. W. and Swegle, J. W., 1994, "Coupling of Smooth Particle Hydrodynamics with the Finite Element Method," *Nuclear Engineering and Design*, Vol. 150, pp. 199-205.

Bubenzer, G. D. and Jones, B. A., Jr., 1971, "Drop Size and Impact Velocity Effects on the Detachment of Soils Under Simulated Rainfall," *Transactions of the American Society of Agricultural Engineers*, Vol. 14 No. 4, pp. 625-628.

Cloutman, L.D., 1990, "Basics of Smoothed Particle Hydrodynamics," Lawrence Livermore National Laboratory, Livermore, CA, report UCRL-ID-103698.

Cloutman, L.D., 1990. "An Evaluation of Smoothed Particle Hydrodynamics," Proceedings of The NEXT Free-Lagrange Conference, Jackson Lake Lodge, Moran, WY, June 3-7

Edwards, T. I., 1973, "On the Terminal Effects of Napalm B and Other Incendigels and the Principal Physical and Chemical Processes That Produce Them," Rand Corporation, Santa Monica, CA, R-1260-PR (AD-528098), June.

Gingold, R. A. and Monaghan, J. J., 1977, "Smoothed Particle Hydrodynamics: Theory and Application to Non-Spherical Stars," *Monthly Notices Royal Astronomy Society*, Vol. 181, pp. 375-389.

Gingold, R.A. and Monaghan, J.J., 1982, "Kernel Estimates as a Basis for General Particle Methods in Hydrodynamics," *Journal Computational Physics*, Vol. 46, pp. 429-453.

Gritzo, L. A., 1994, Memo on the NAWC tests, (Personal Communication).

Libersky L. D. and Petschek, A. G., 1990, "Smooth Particle Hydrodynamics with Strength of Materials," *Advances in the Free Lagrange Method*, Lecture Nodes in Physics 395, pp. 248-257.

Lucy, L. B., 1977, "A Numerical Approach to the Testing of Fusion Process," T*he Astronomical Journal*, Vol. 88, December, pp 1013-1024.

Miller, C. W., 1990, "Two-Dimensional Model of Jet Penetration," *Proceedings of the 12th International Symposium on Ballistics*, Vol. III, Held Oct. 30-Nov. 1, Municipal Auditorium, San Antonio, Texas, pp. 8-21.

Monaghan, J.J., 1982, "Why Particle Methods Work," *SIAM Journal Scientific Statistical Computing*, Vol. 3, pp. 422-433

Monaghan, J.J. and Gingold, R.A., 1983, "Shock Simulation by the Particle Method SPH," *Journal of Computational Physics*, Vol. 52, pp. 374-389.

Moya, J. L., 1994, Memo on the Fairchild Accident, (Personal Communication).

Park, S. W., Mitchell, J. K., Bubenzer, G. D., 1982, "Splash Erosion Modeling: Physical Analyses," *Transactions of the American Society of Agricultural Engineers*, Vol. 25 No. 2, pp. 357-361.

Riezebos, H., Th. and Epema, G. F., 1985, "Drop Shape and Erosivity Part II: Splash Detachment, Transport, and Erosivity Indices", *Earth Processes and Landforms*, Vol. 10, pp. 69-74.

Swegle, J. W.; Attaway, S. W.; Heinstein, M. W.; Mello, F. J; and Hicks, D. L.; 1994, "An Analysis of Smoothed Particle Hydrodynamics," SAND93-2513, Sandia National Laboratories, Albuquerque, NM.

Taylor, L.M. and Flanagan, D.P., 1987. "PRONTO 2D: A Two Dimensional Transient Solid Dynamics Program," SAND86-0594, Sandia National Laboratories, Albuquerque, NM.

Taylor, L.M. and Flanagan, D.P., 1989. "PRONTO 3D: A Three Dimensional Transient Solid Dynamics Program," SAND 87-1912, Sandia National Laboratories, Albuquerque, NM

Tieszen, S. R., 1995, "Fuel Dispersal Modeling for Aircraft-Runway Impact Scenarios," SAND95-2529, Sandia National Laboratories, Albuquerque NM.

von Riesemann, W. A., Parrish, R. L., Bickel, D. C., Heffelfinger, S. R., Muto, K., Sugano, T., Tsubota, H., Koshika, N., Suzuki, M., Ohrui, S., 1989, "Full-Scale Aircraft Impact Test for Evaluation of Impact Forces Part 1: Test Plan, Test Method, and Test Results," *Transactions of the 10th International Conference on Structural Mechanics in Reactor Technology*, Vol. J (Ed. Hadjian, A. H.), American Association for Structural Mechanics, Los Angeles, CA, pp. 285-293.

Wittlin, G., 1987, "Fuel Containment Concepts - Transportation Category Airplanes," Lockheed-California Company, Burbank, CA, FAA Report DOT/FAA/CT-87/18, November.

Appendix A

Crater overhead views, soil cross-sections, and crater cross-sections were made for each test and are shown in this Appendix. The test matrix is given in Table A1. The test order was random with tests 9 through 12 being conducted before 1 through 6.The results are listed in numerical order in this appendix. Crater overhead views and soil cross-sections are shown together followed by the crater cross-sections. Note that test numbers 7 and 8 are developmental and not included in the data set. Table A1 gives the nominal test conditions.

Table A1. Test Matrix Numbers for Impact Angle and Impact Velocity.

		Impact Angle (Degrees)		
		22.5	45	67.5
Impact Velocity (m/s)	30	9	10	11
	64	3	6,12	1
	92	4	5	2

One overhead view and five sections are given as shown schematically in Figure A1.

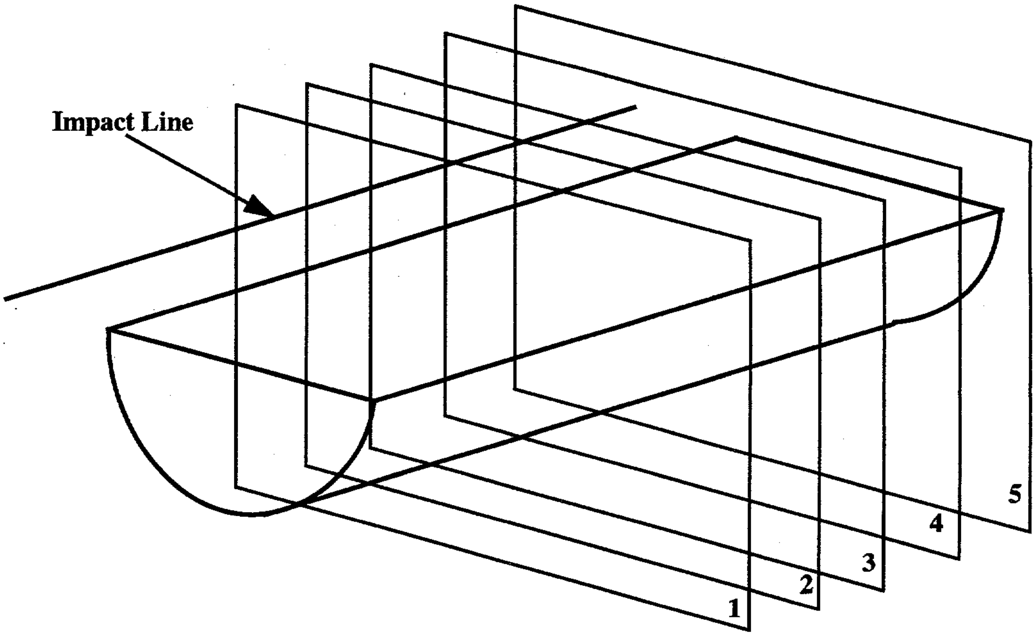

FIGURE A1. Schematic Showing Sectional Views of Crater for Each Test.

The sections are sliced along the axis of impact. Section 1 corresponds to the mid-wing impact plane. Section 2 corresponds to the 1/3 span impact plane. Section 3 corresponds to the 2/3 span. Section 4 corresponds to the edge of the wing (full span) impact plane, and section 5 corresponds to 4/3 span impact plane.

In all figures, the liquid jet impinged from the left and splashed to the right. The ruler in all the figures has millimeter tick marks and numbers every centimeter. In the Figures with crater cross-sections, Section 1 is at the bottom of each figure. Section 2 is above section 1, etc.

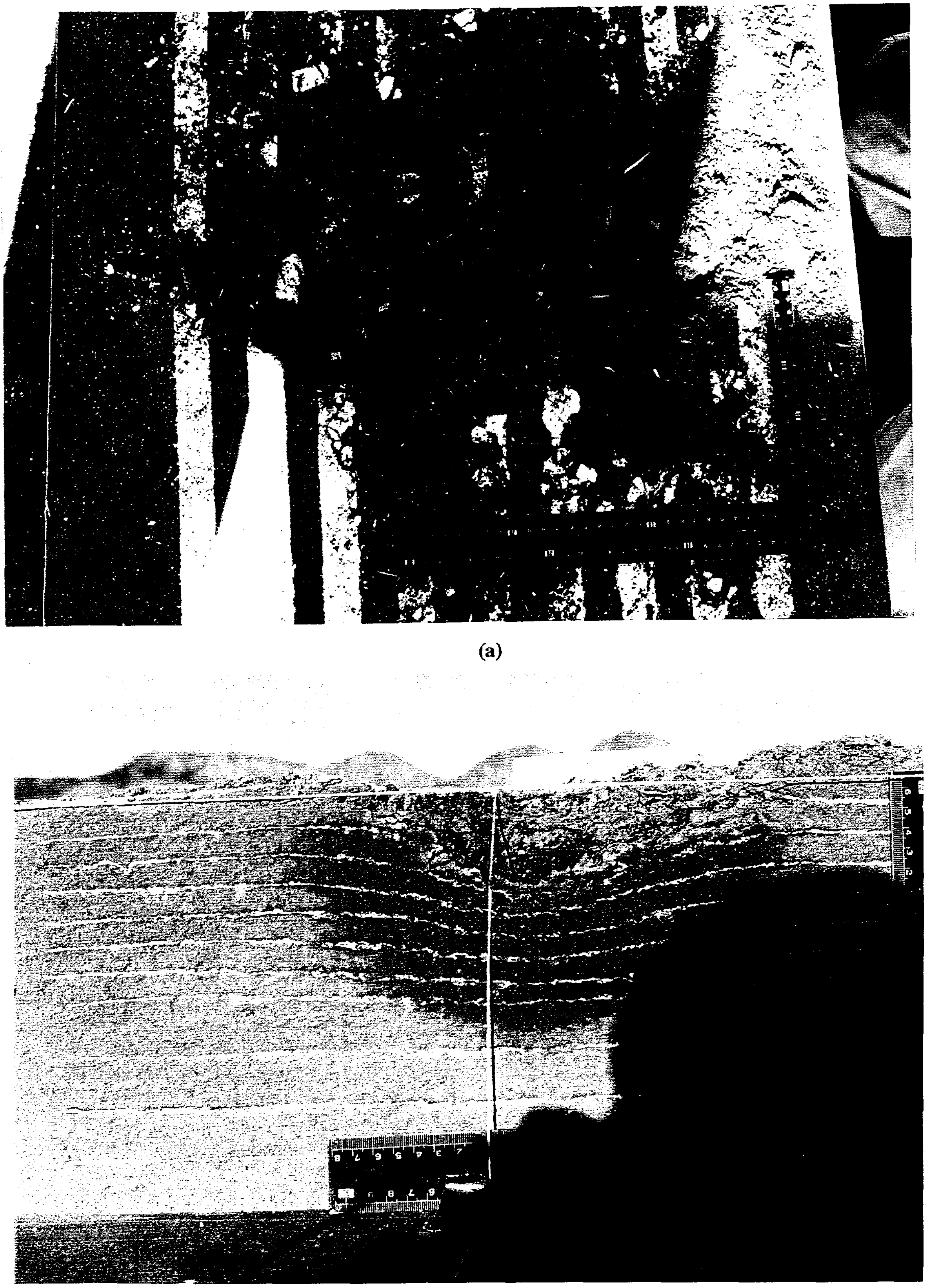

(a)

(b)

FIGURE A2. Views of Soil Sections for Test #1. (a)Overhead. (b)Section 1.

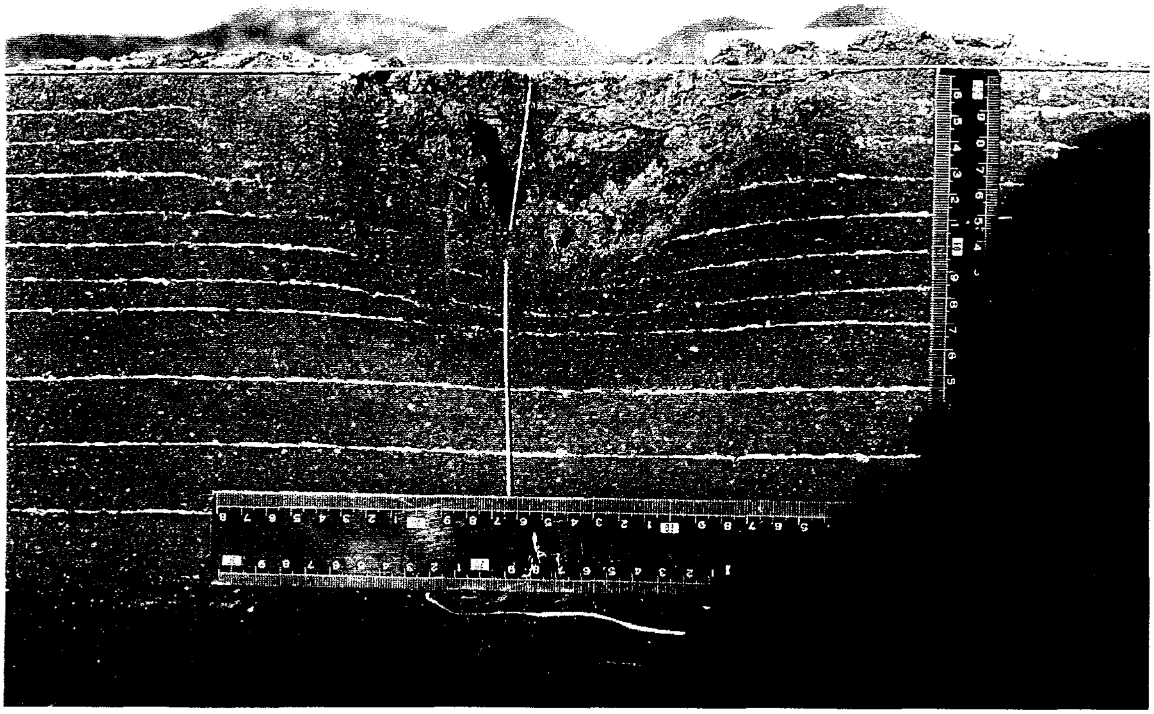

(c)

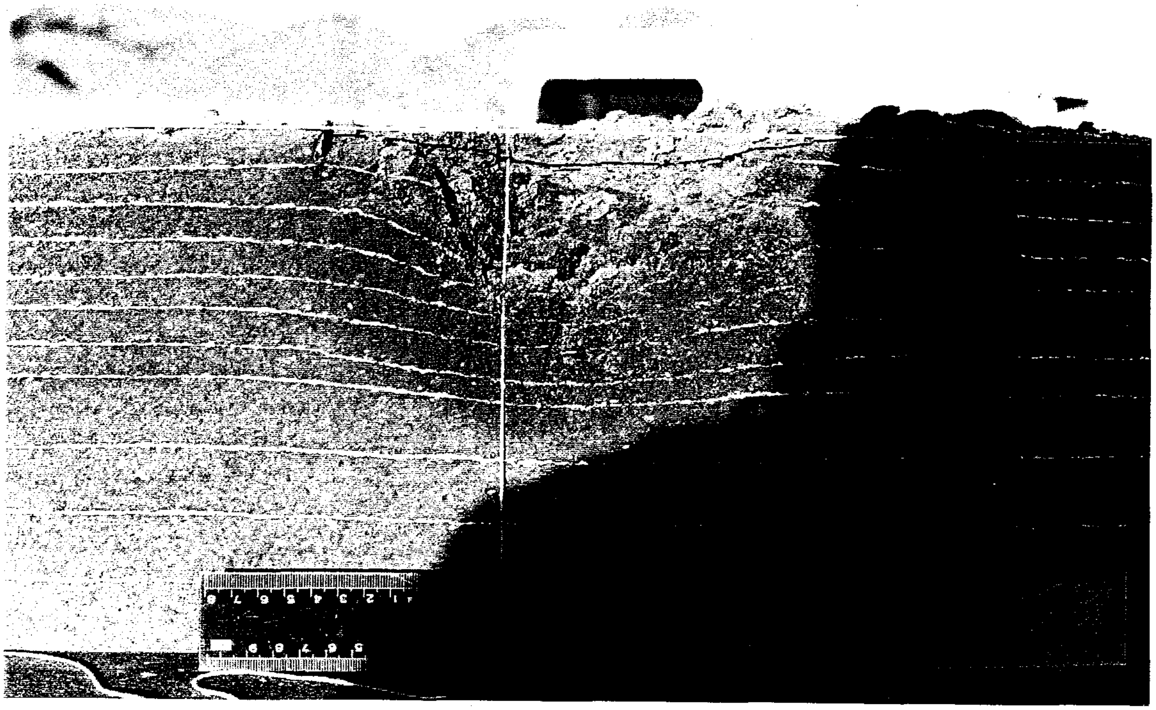

(d)

FIGURE A2(Cont). Views of Soil Sections for Test #1. (c)Section 2. (d)Section 3.

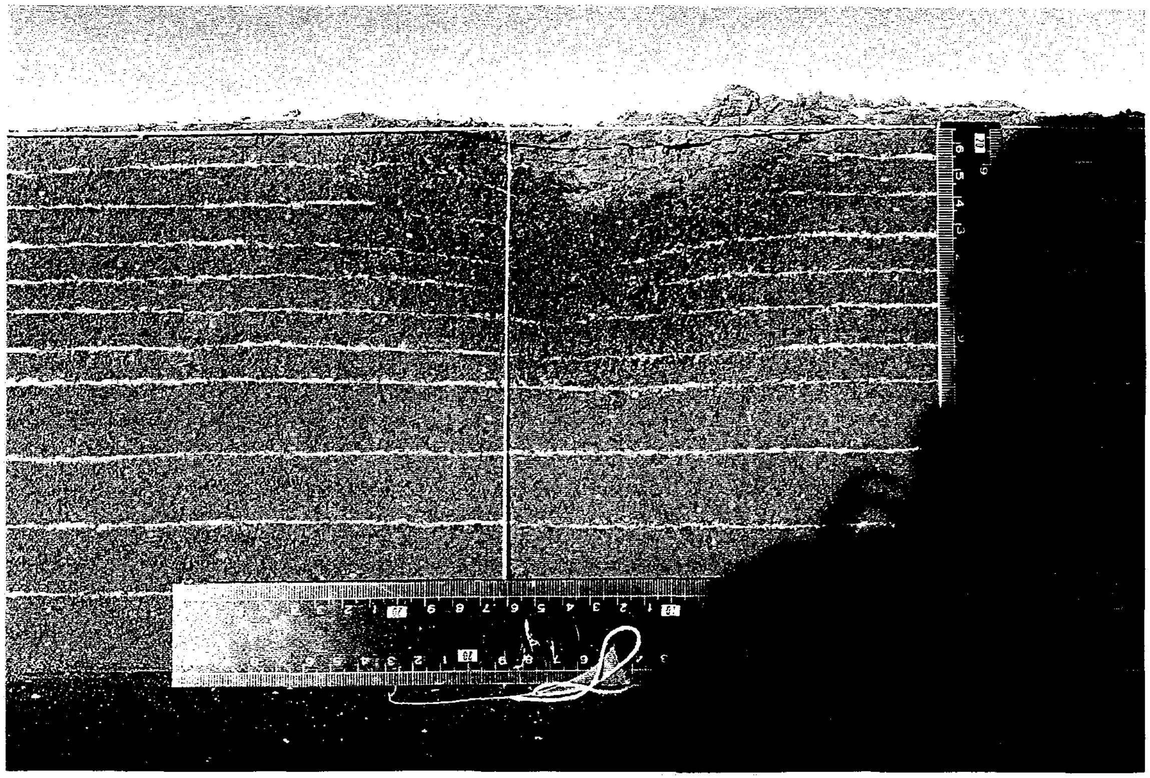

(e)

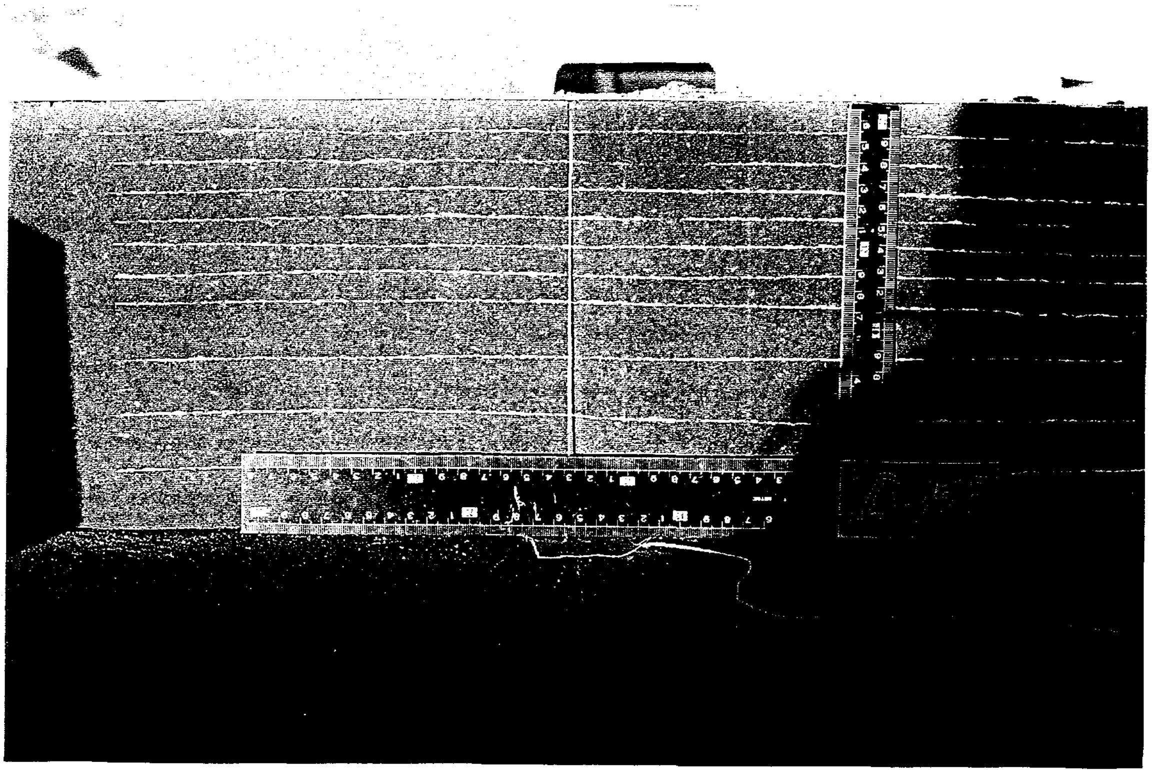

(f)

FIGURE A2(Cont). Views of Soil Sections for Test #1. (e)Section 4. (f)Section 5.

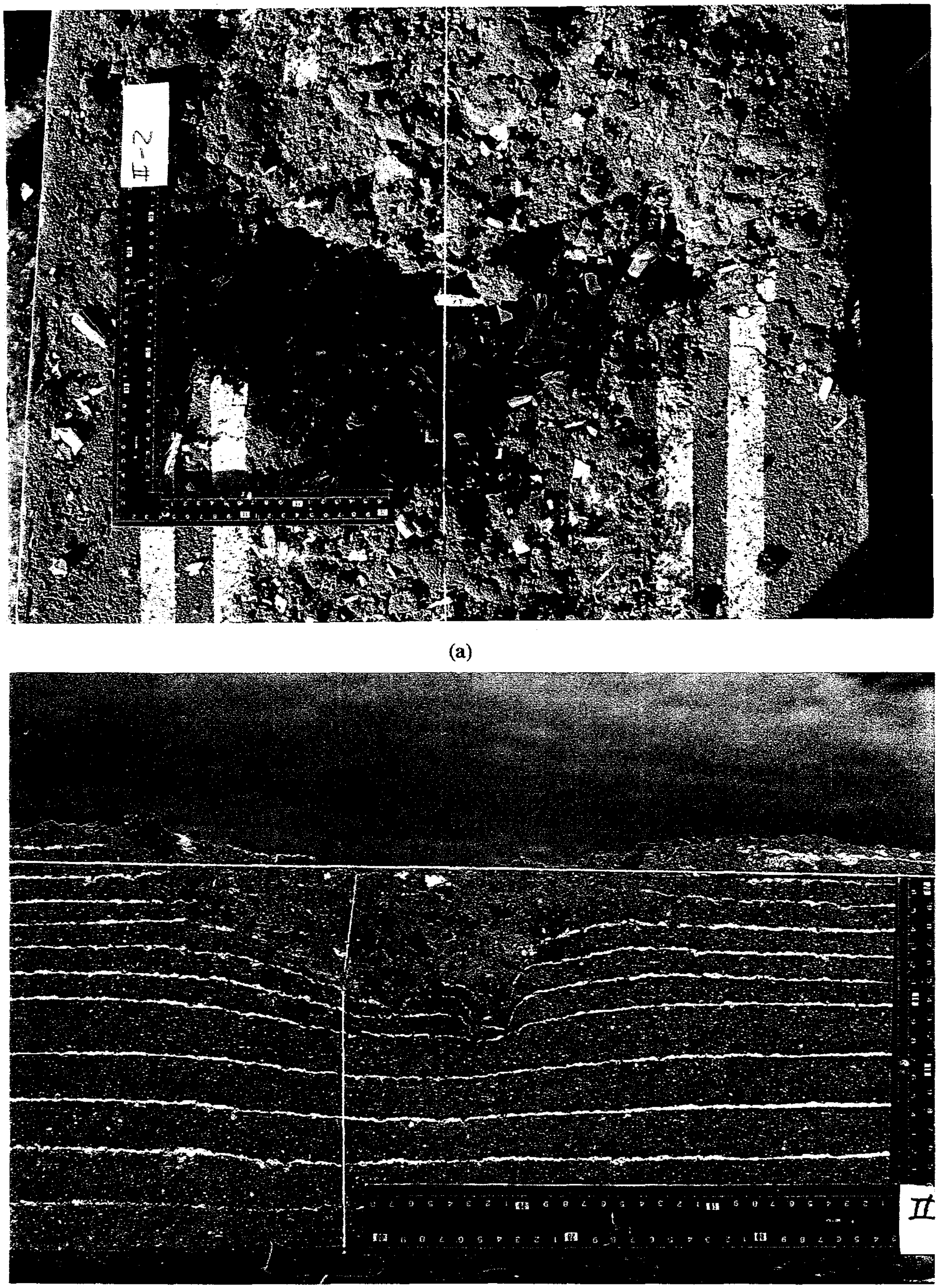

(a)

(b)

FIGURE A3. Views of Soil Sections for Test #2. (a)Overhead. (b)Section 1.

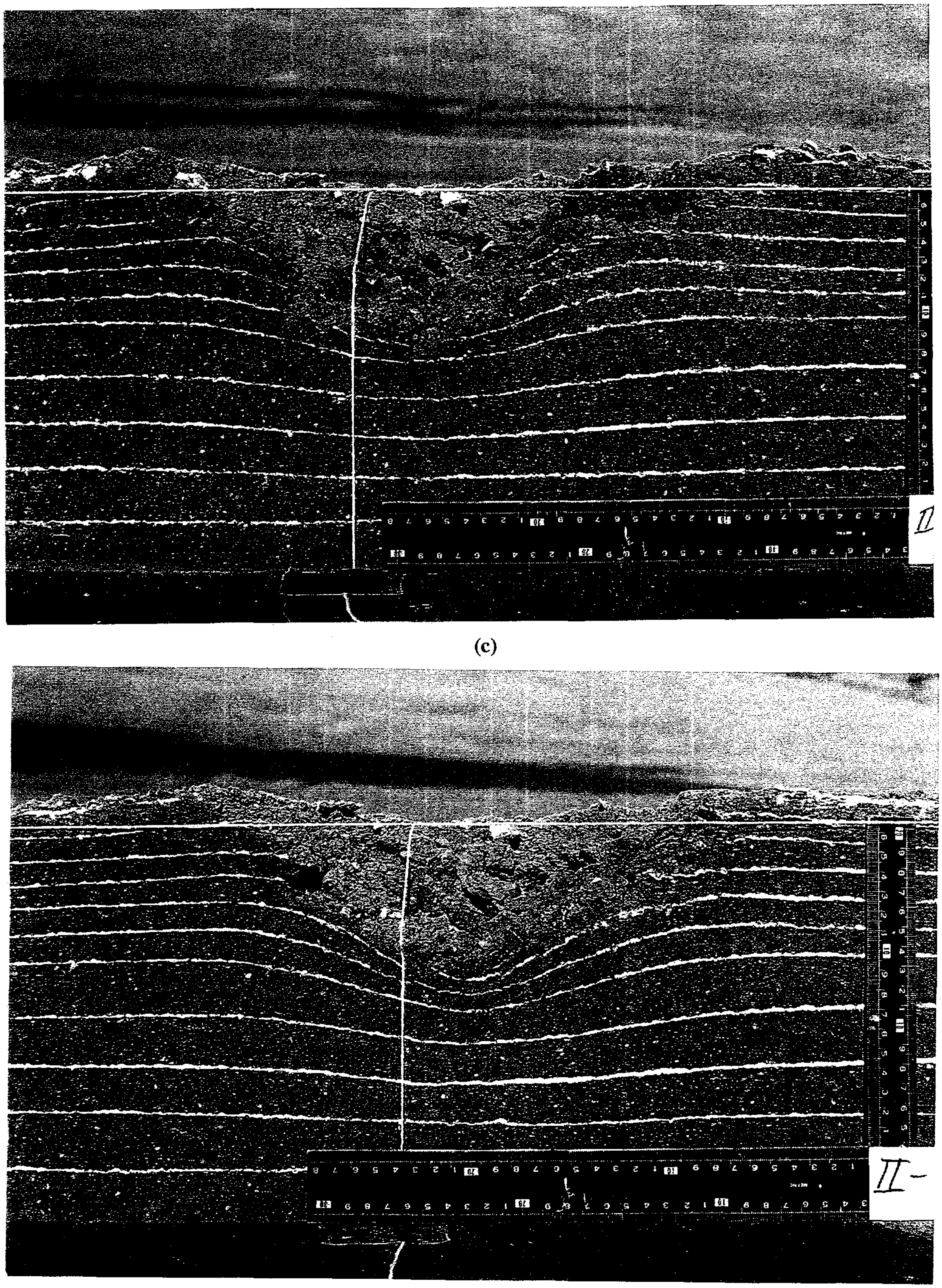

(c)

(d)

FIGURE A3(Cont). Views of Soil Sections for Test #2. (c)Section 2. (d)Section 3.

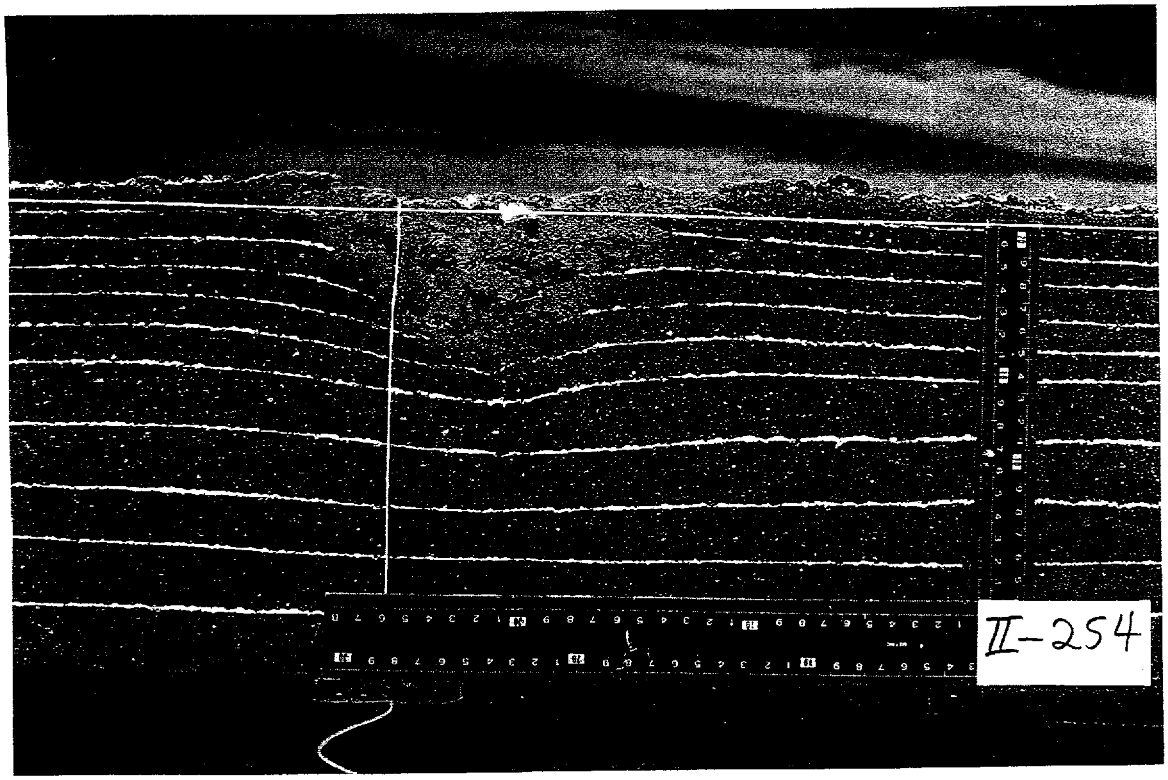

(e)

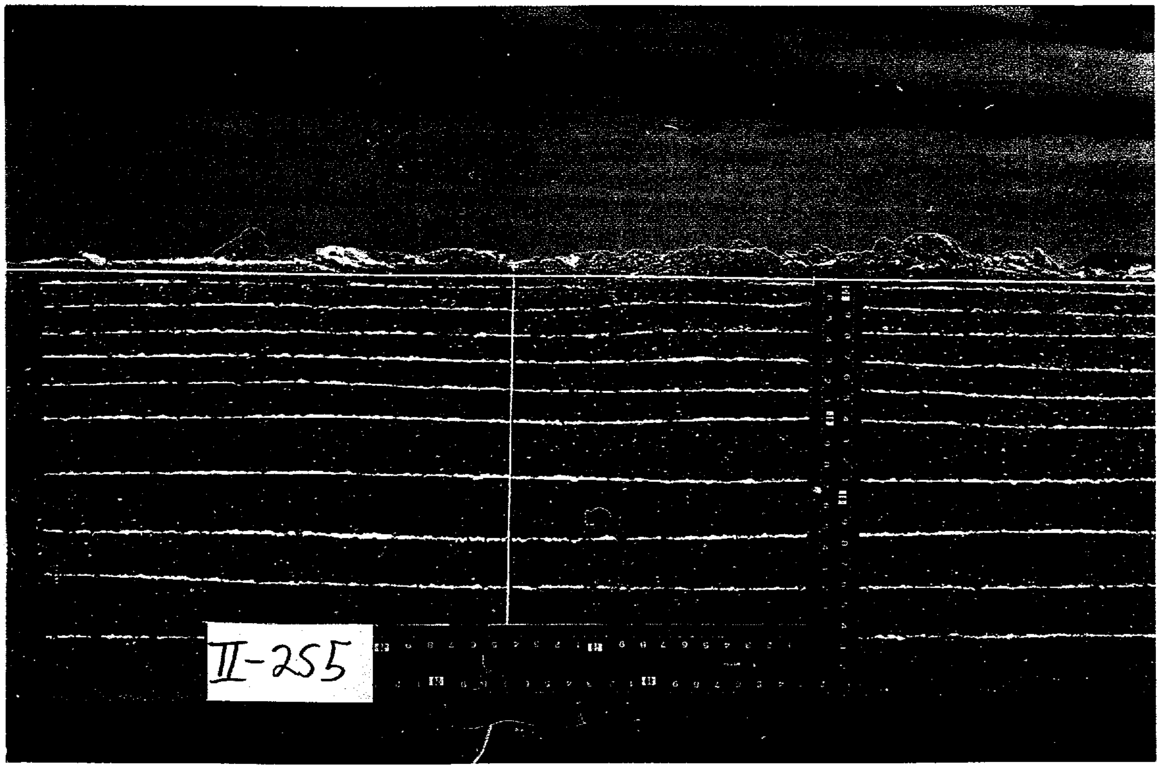

(f)

FIGURE A3(Cont). Views of Soil Sections for Test #2. (e)Section 4. (f)Section 5.

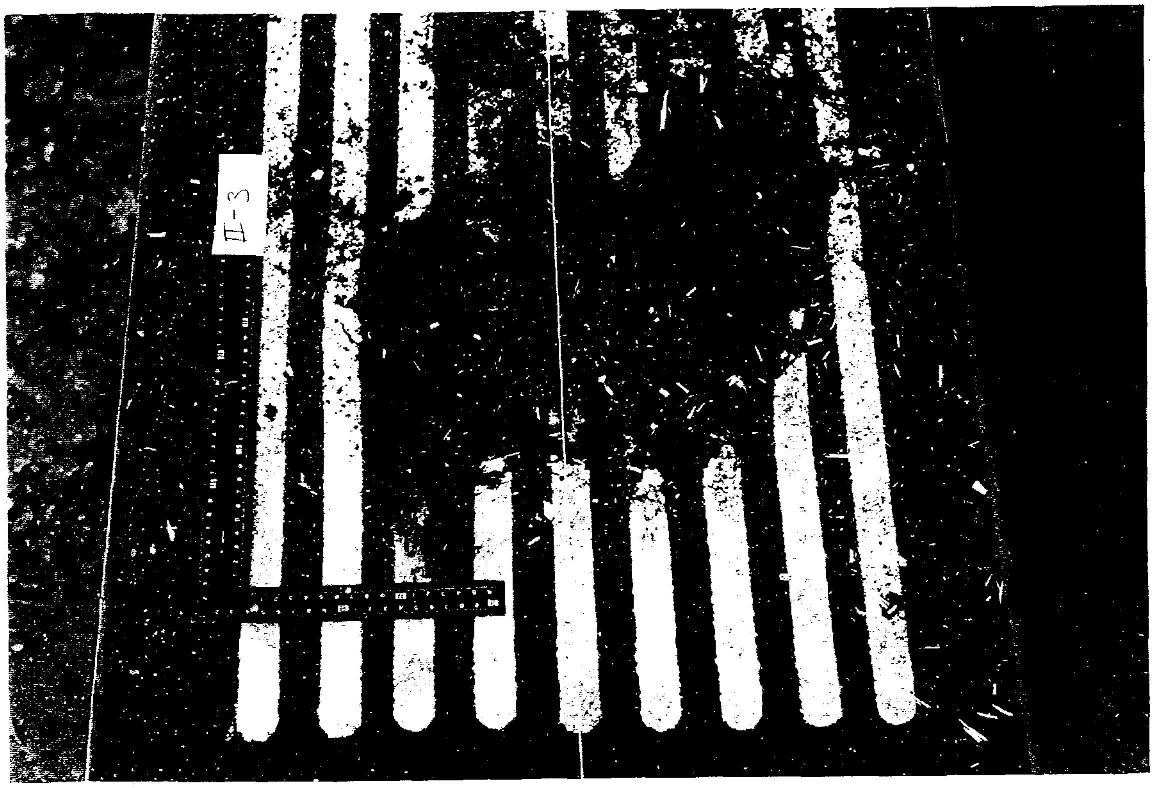

(a)

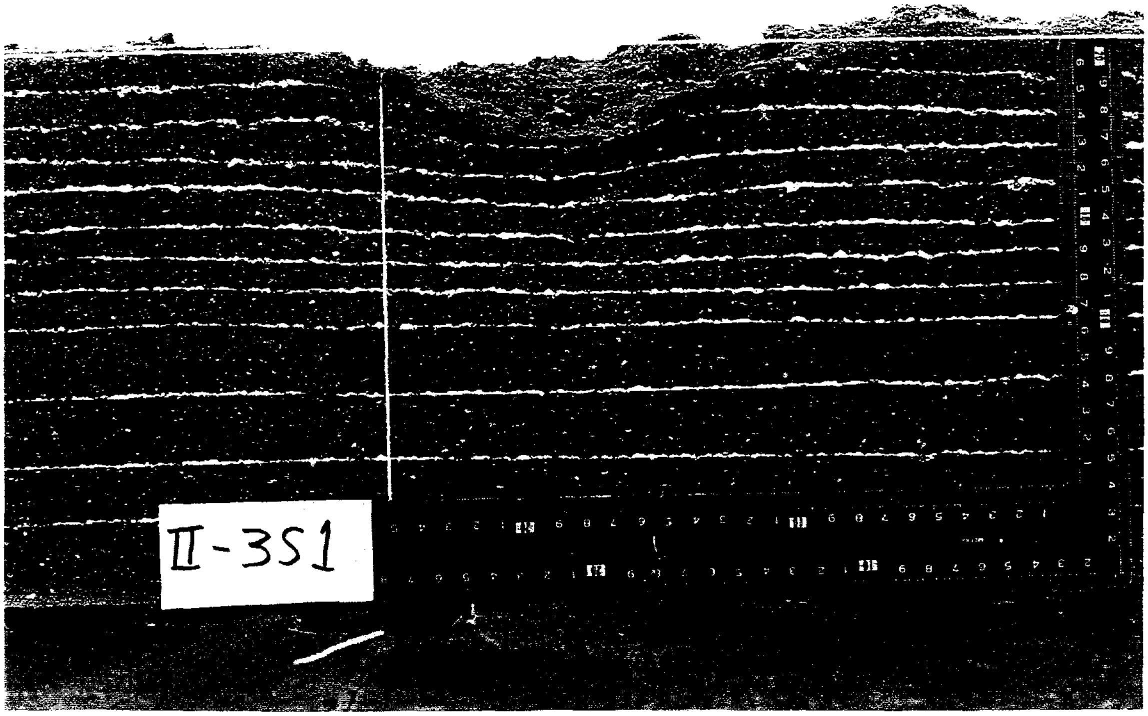

(b)

FIGURE A4. Views of Soil Sections for Test #3. (a)Overhead. (b)Section 1.

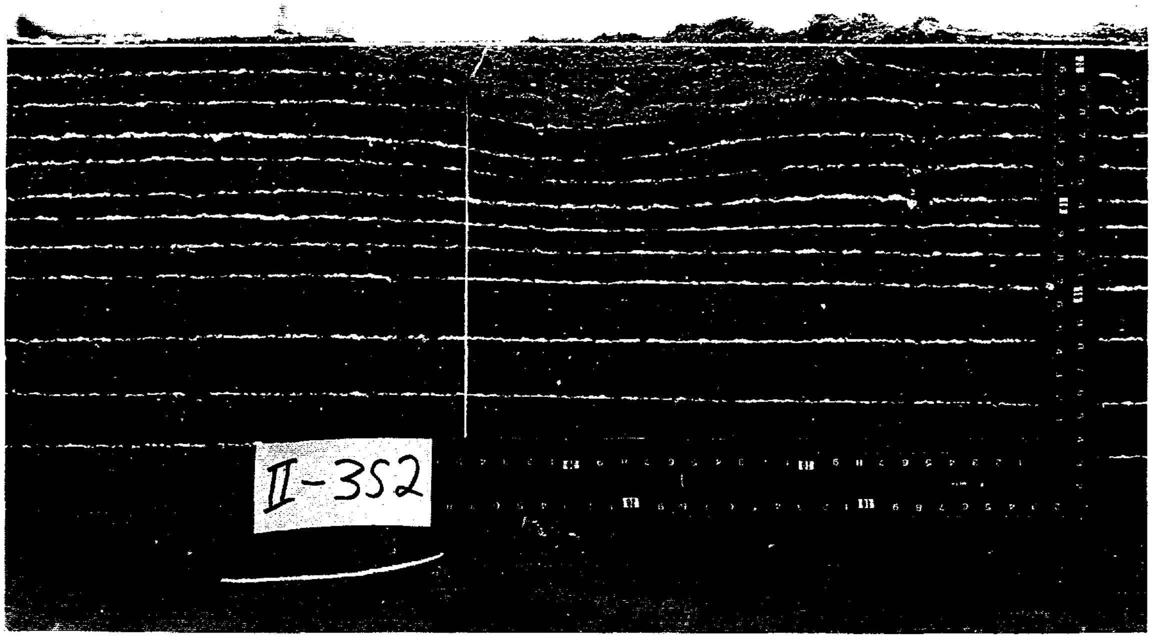

(c)

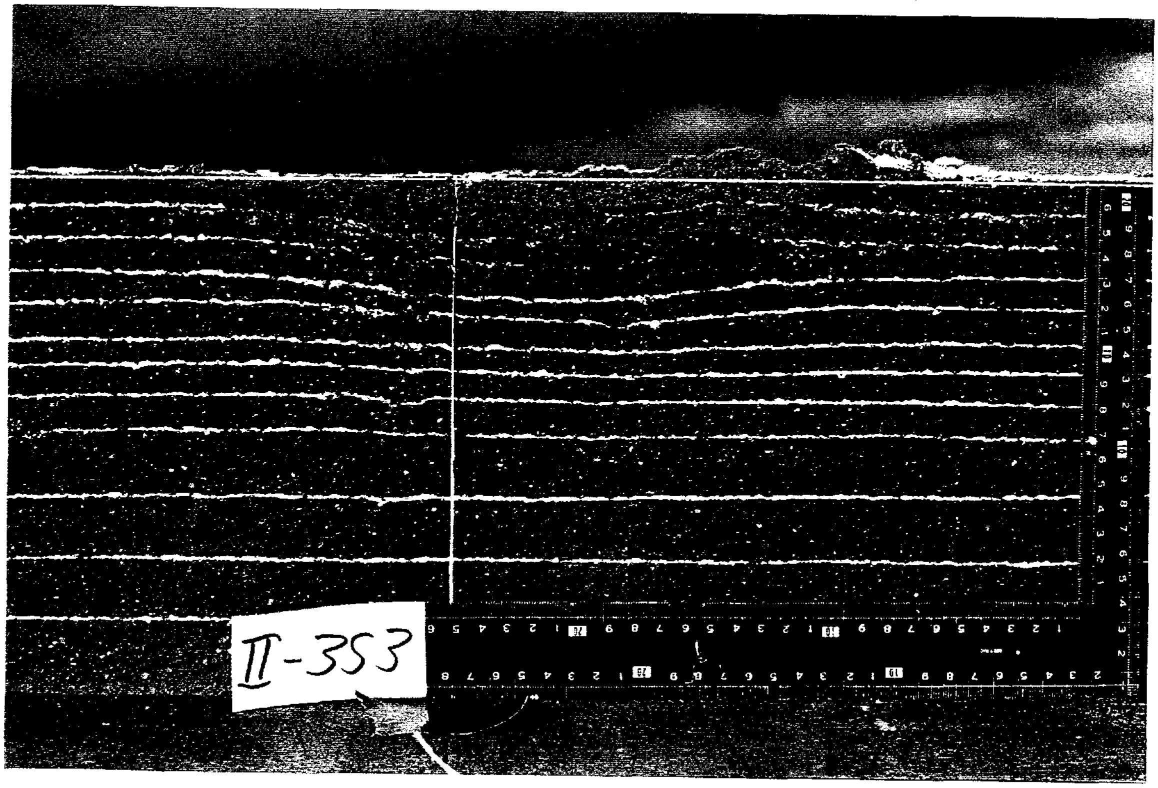

(d)

FIGURE A4(Cont). Views of Soil Sections for Test #3. (c)Section 2. (d)Section 3.

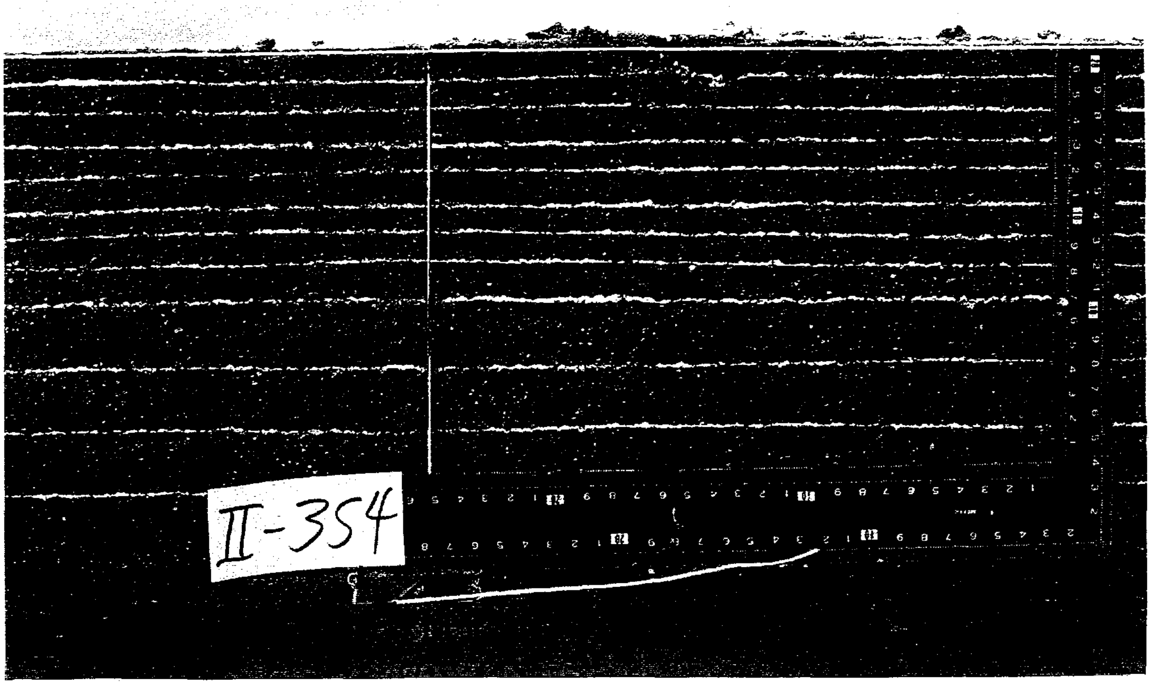

(e)

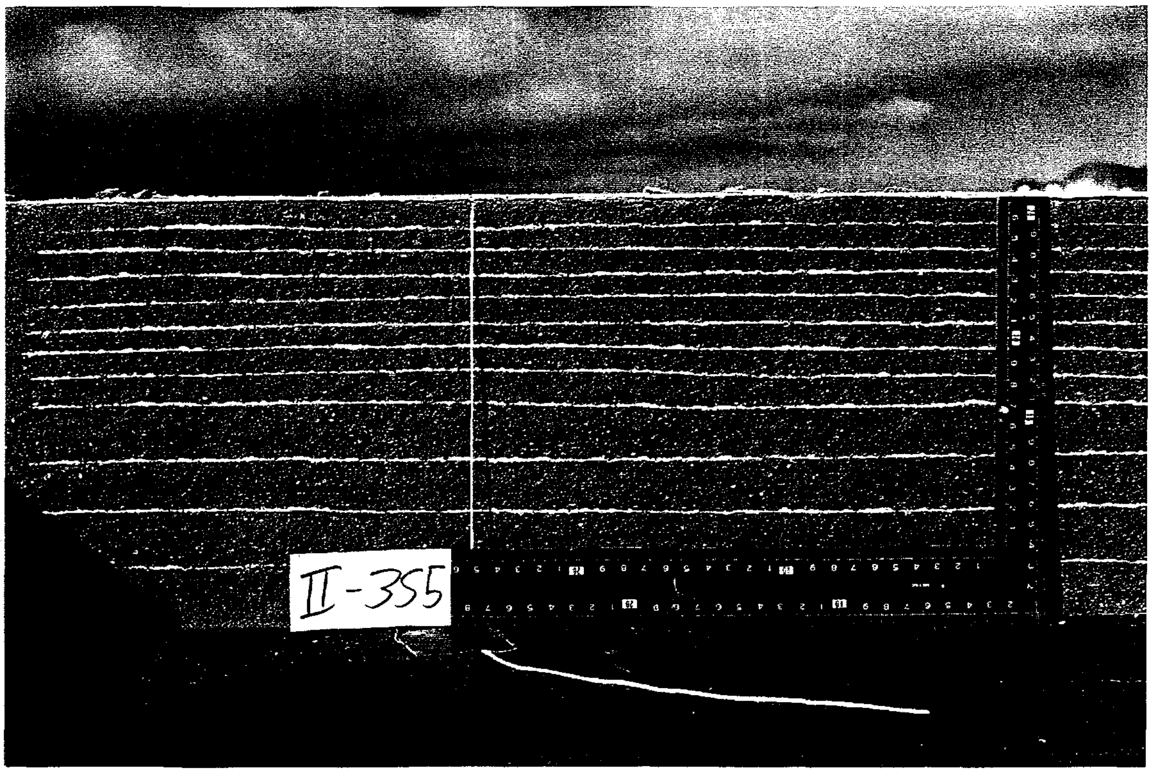

(f)

FIGURE A4(Cont). Views of Soil Sections for Test #3. (e)Section 4. (f)Section 5.

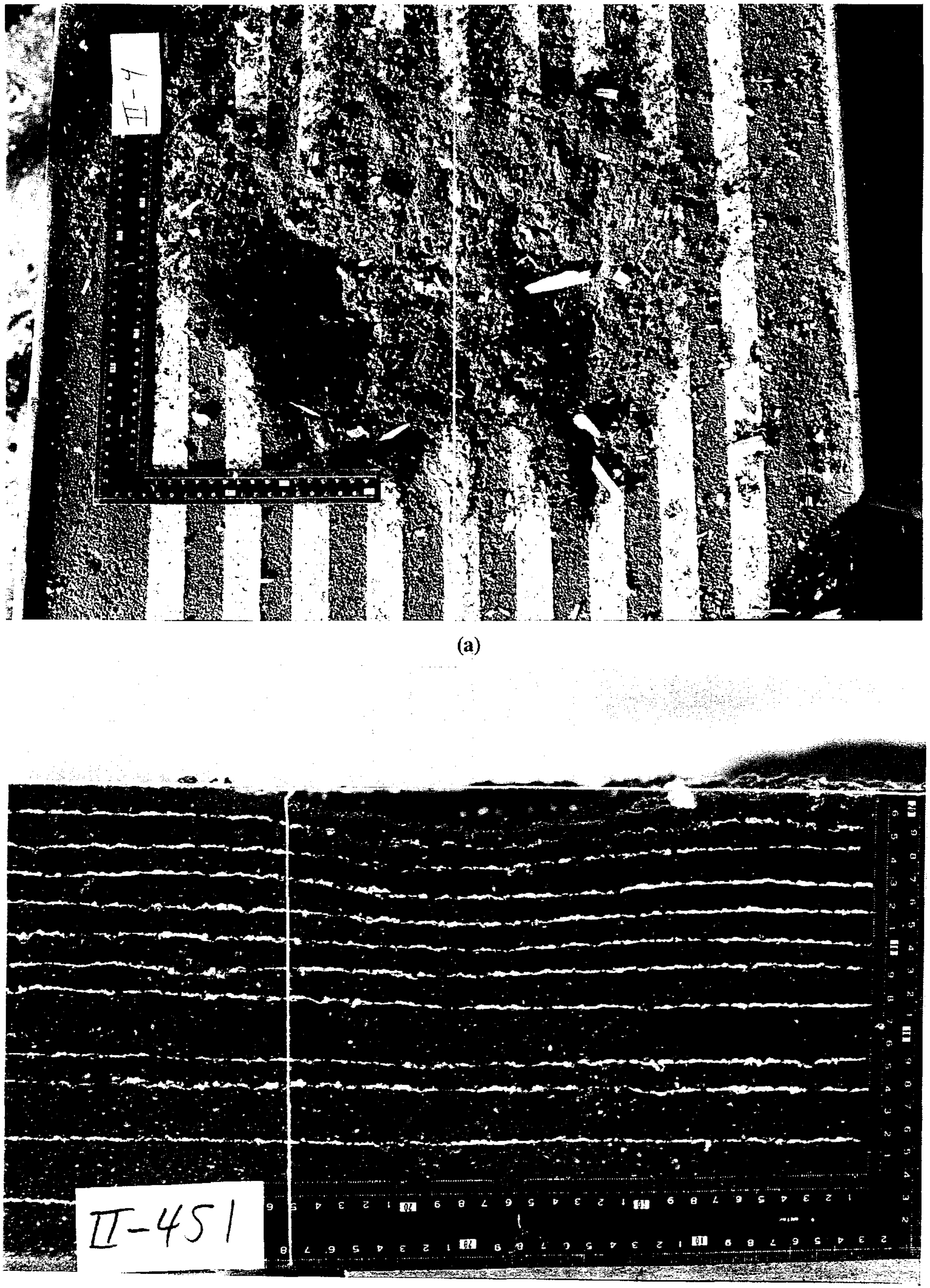

(a)

(b)

FIGURE A5. Views of Soil Sections for Test #4. (a)Overhead. (b)Section 1.

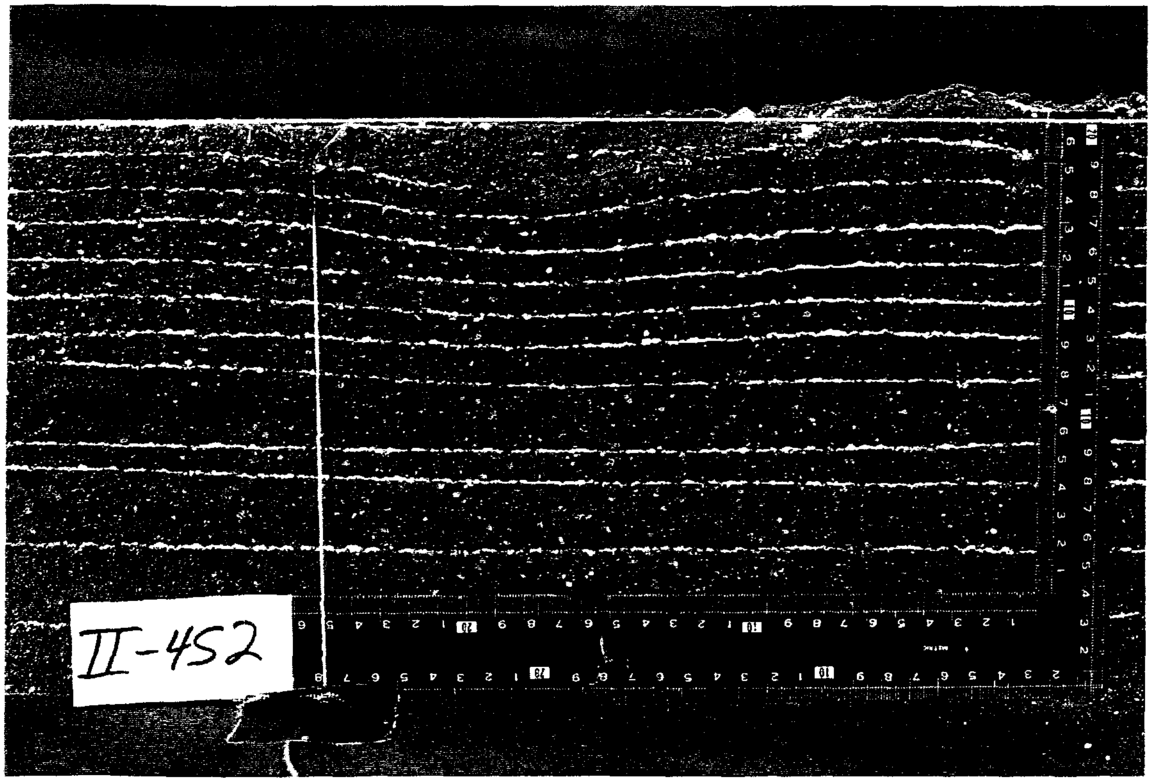

(c)

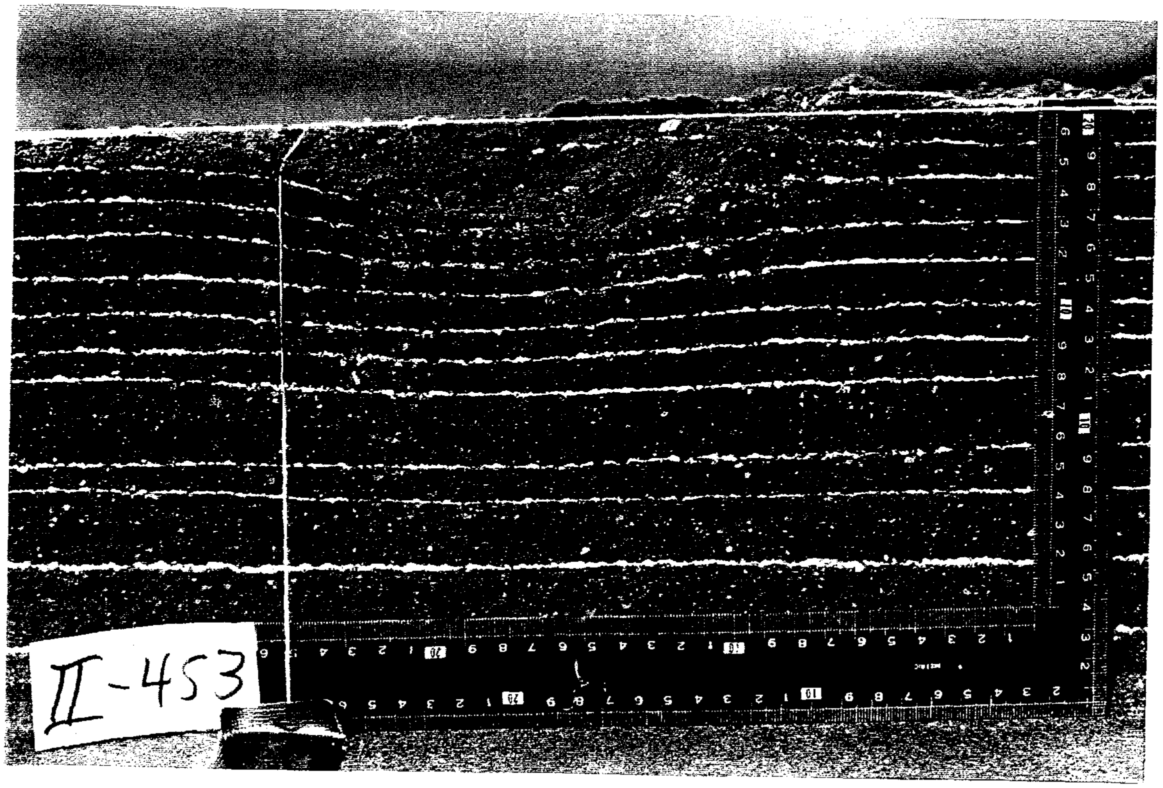

(d)

FIGURE A5(Cont). Views of Soil Sections for Test #4. (c)Section 2. (d)Section 3.

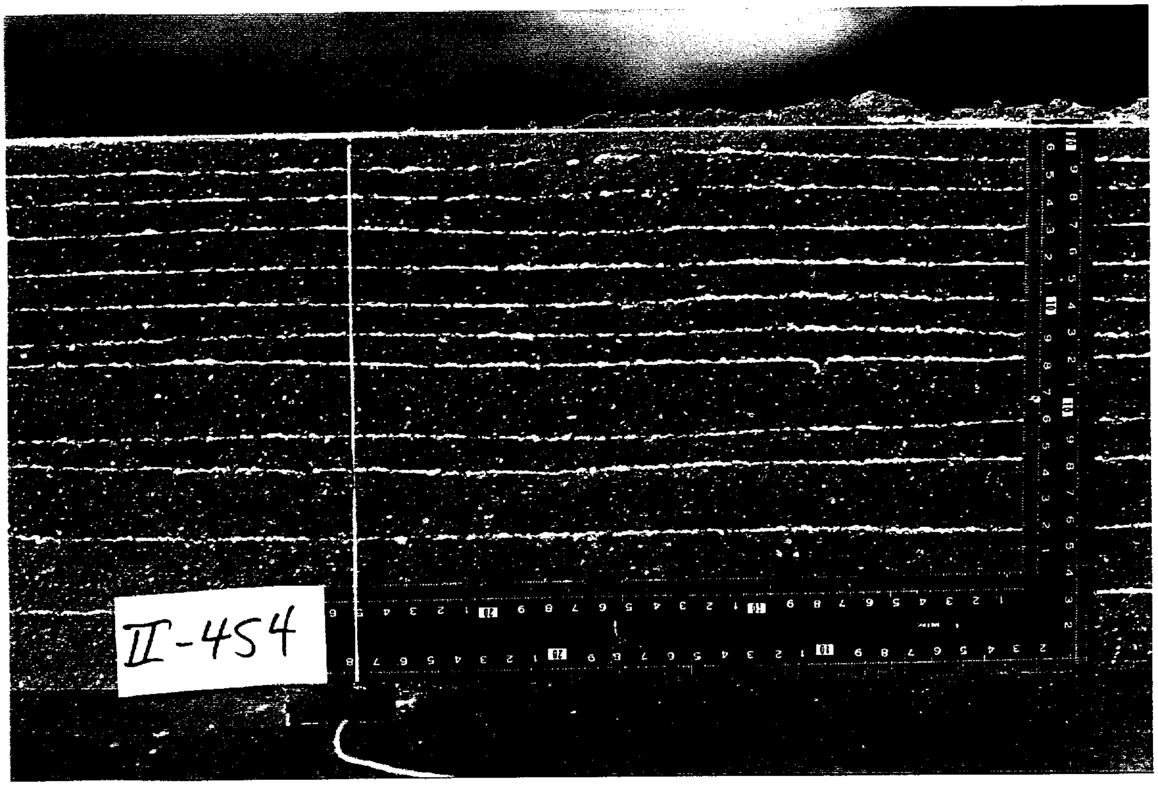

(e)

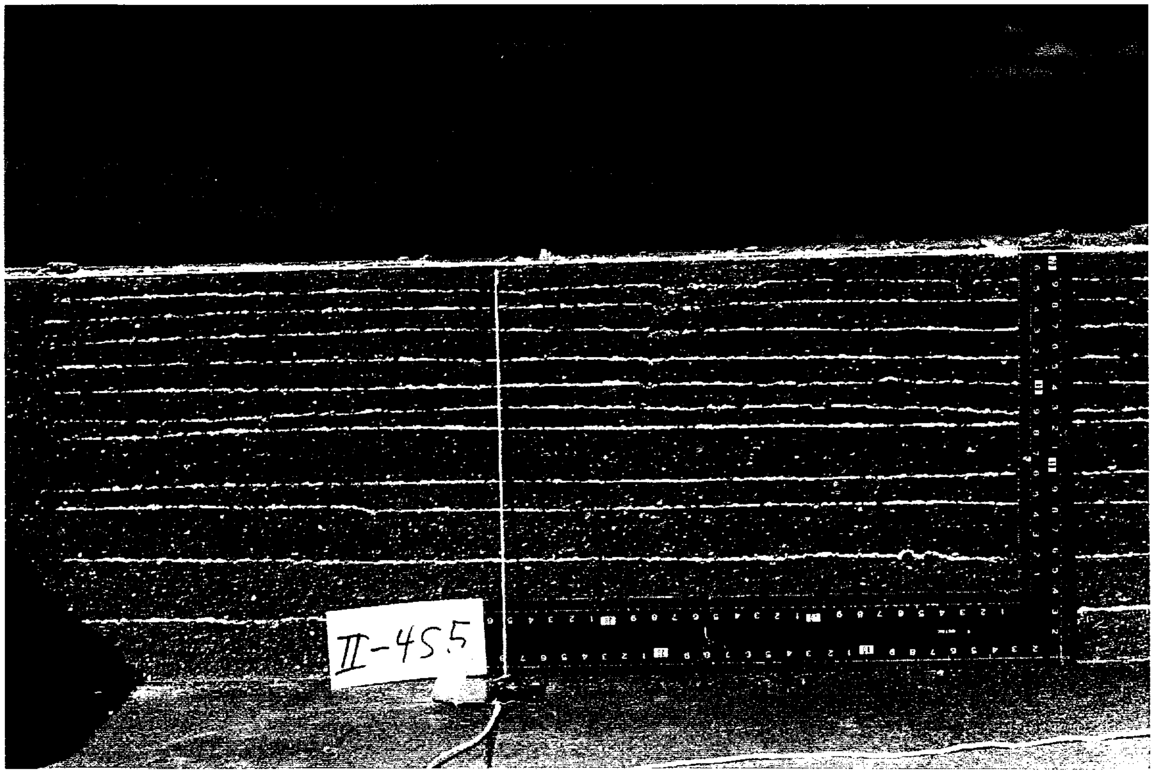

(f)

FIGURE A5(Cont). Views of Soil Sections for Test #4. (e)Section 4. (f)Section 5.

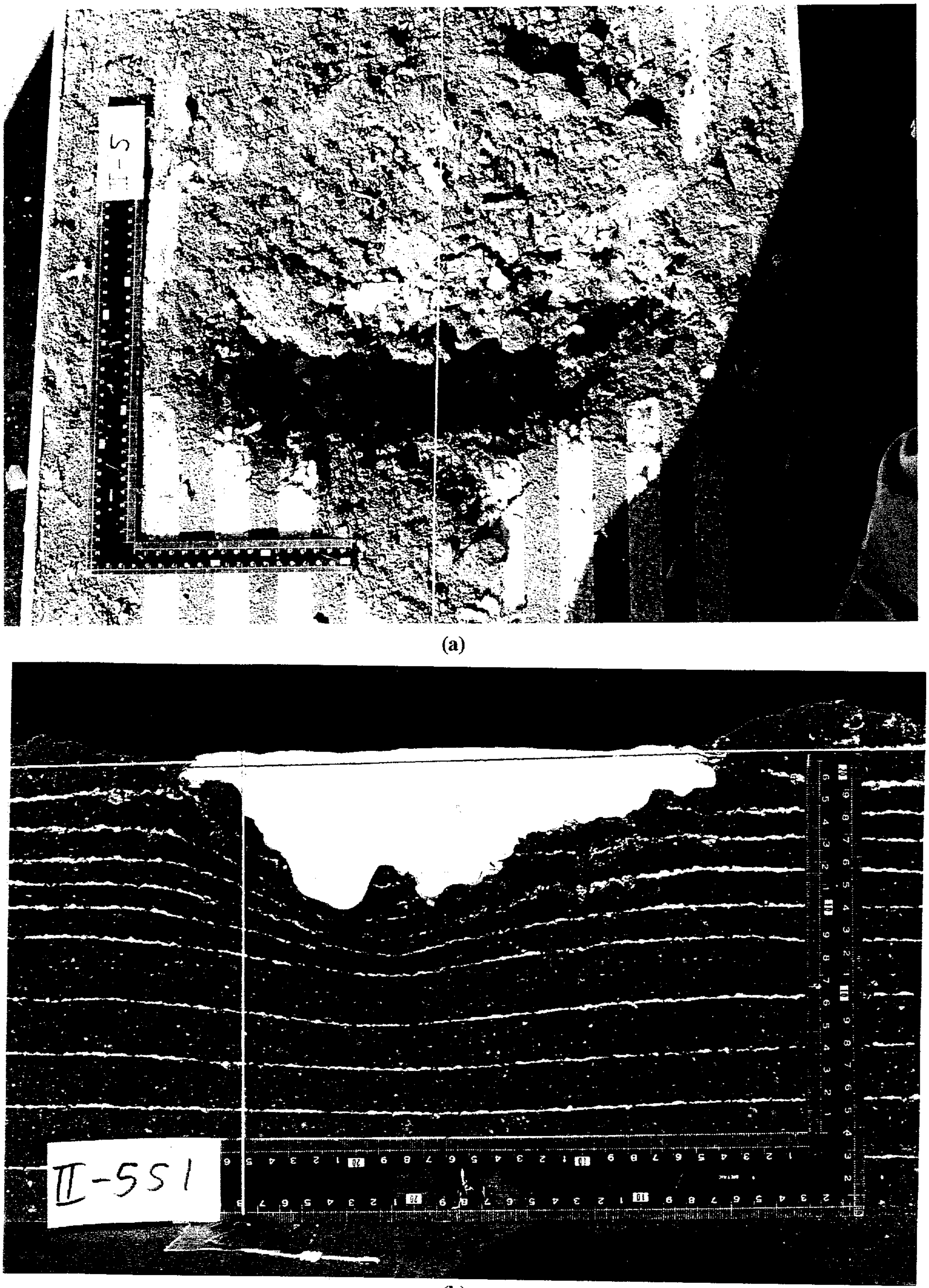

(a)

(b)

FIGURE A6. Views of Soil Sections for Test #5. (a)Overhead. (b)Section 1.

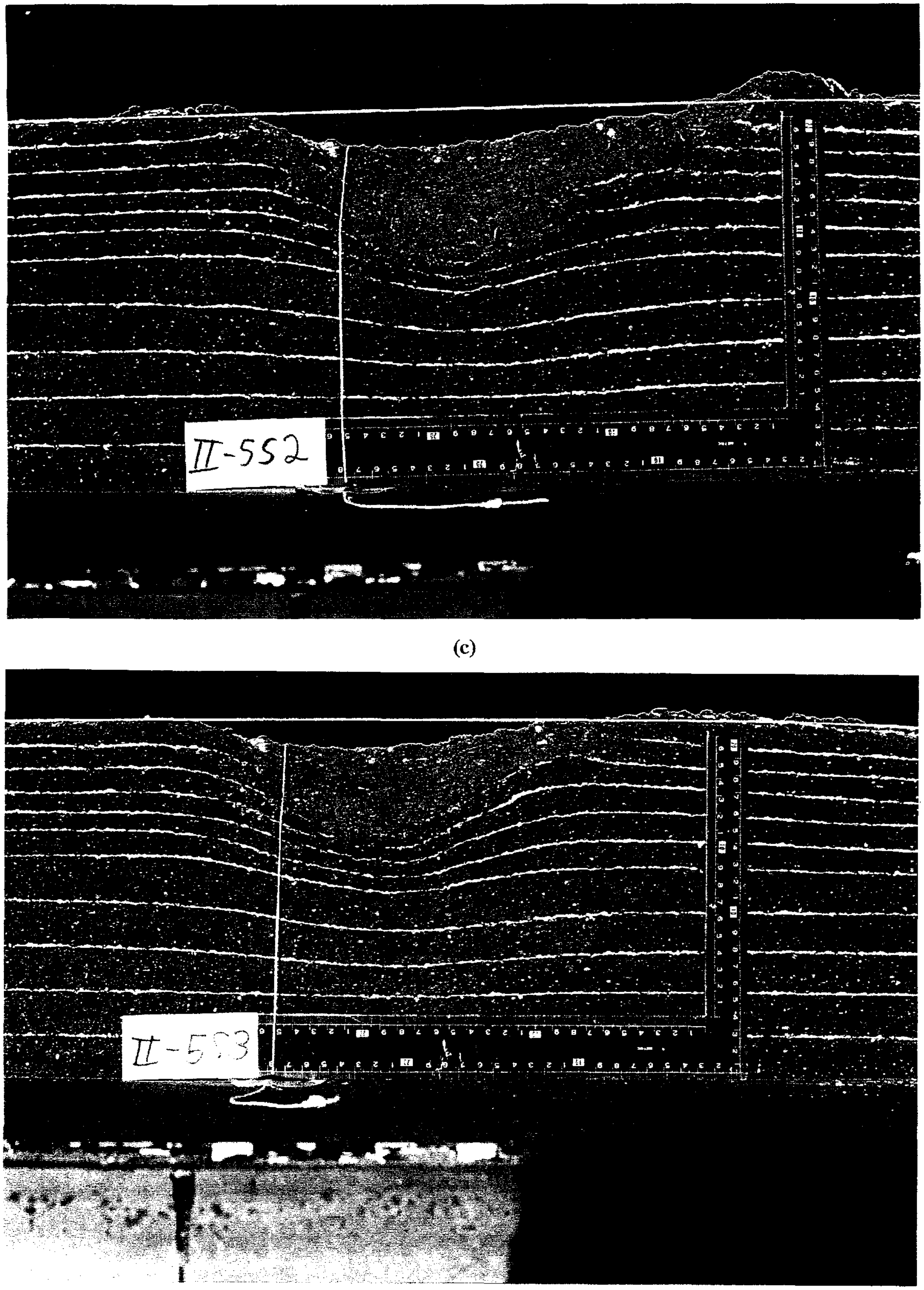

(c)

(d)

FIGURE A6(Cont). Views of Soil Sections for Test #5. (c)Section 2. (d)Section 3.

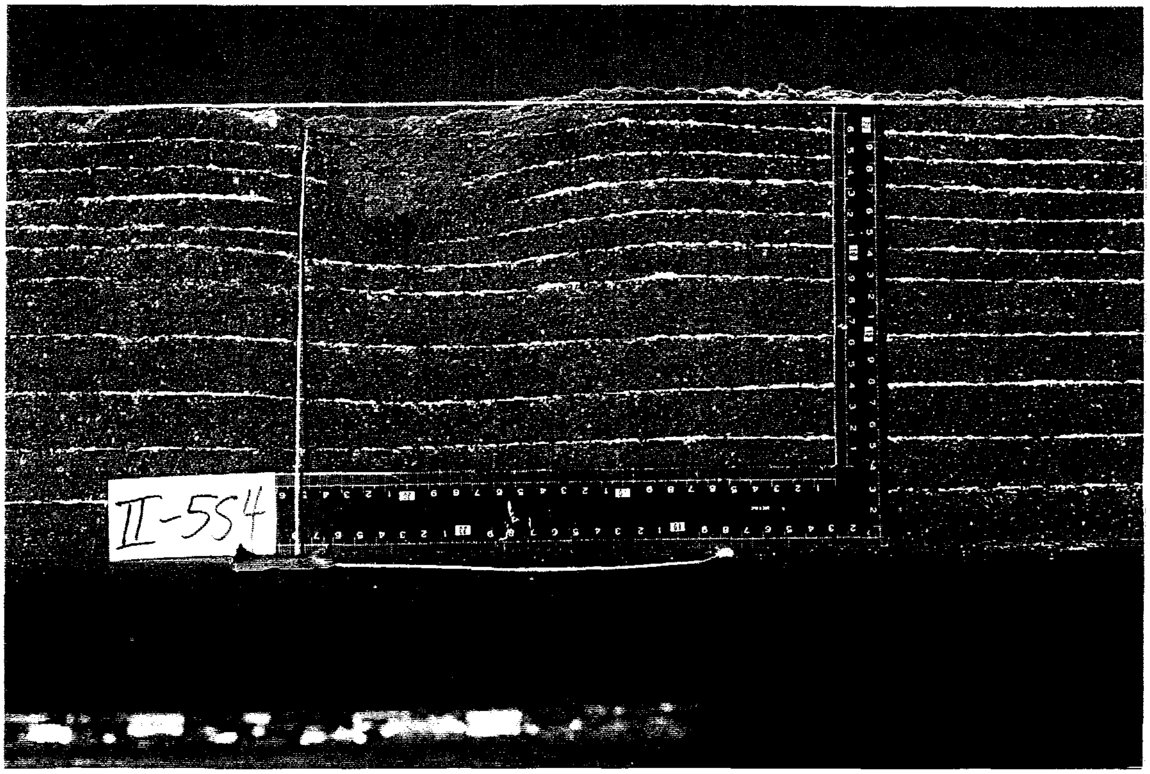

(e)

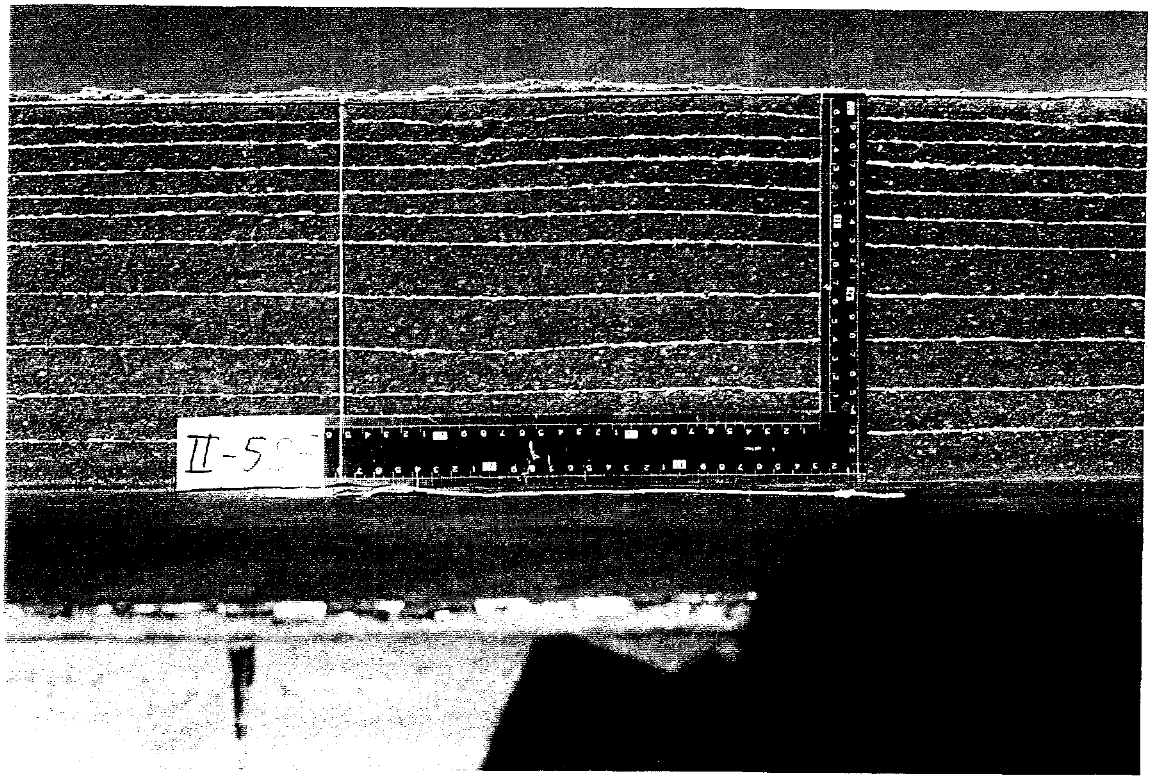

(f)

FIGURE A6(Cont). Views of Soil Sections for Test #5. (e)Section 4. (f)Section 5.

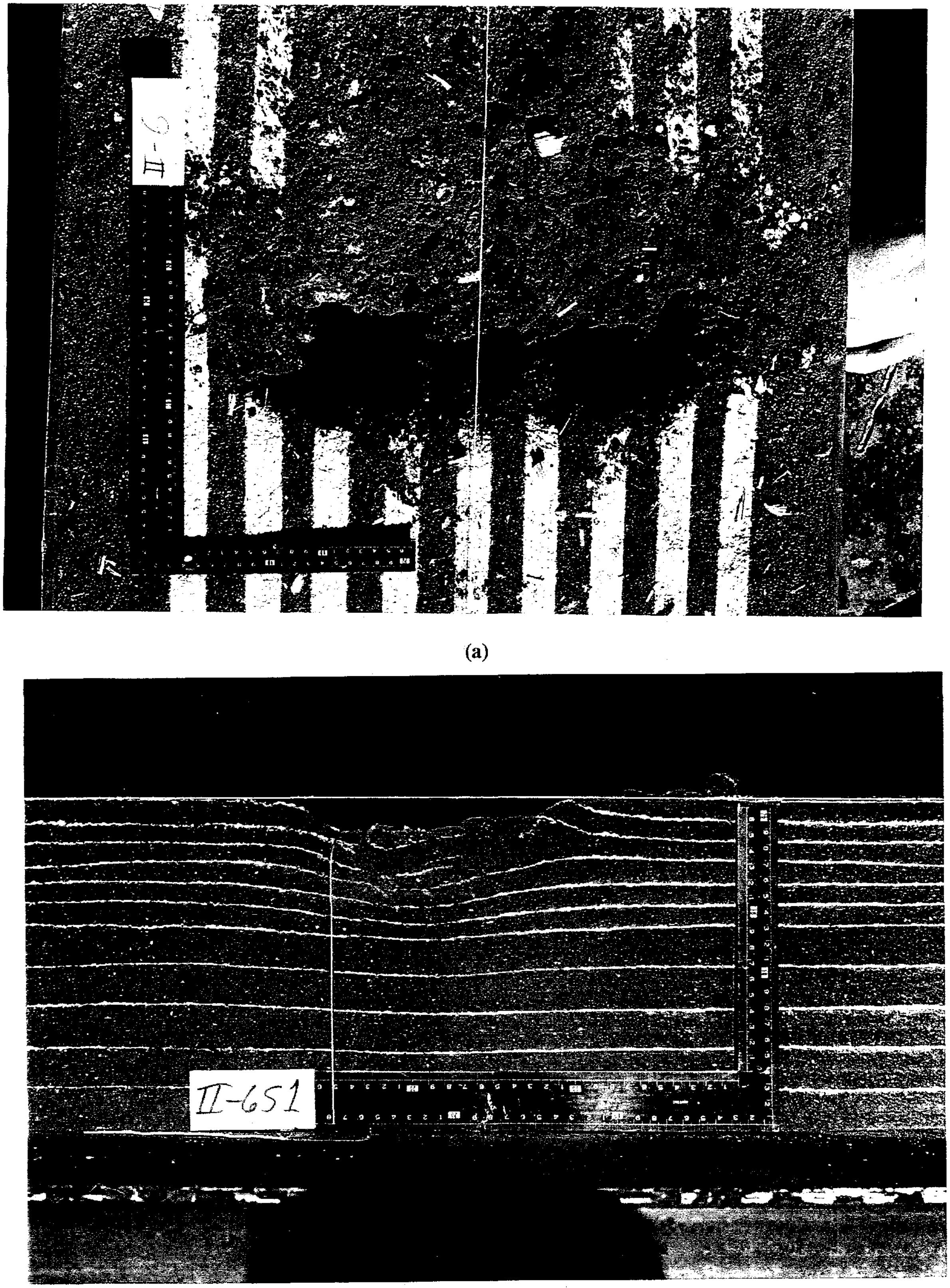

(a)

(b)

FIGURE A7. Views of Soil Sections for Test #6. (a)Overhead. (b)Section 1.

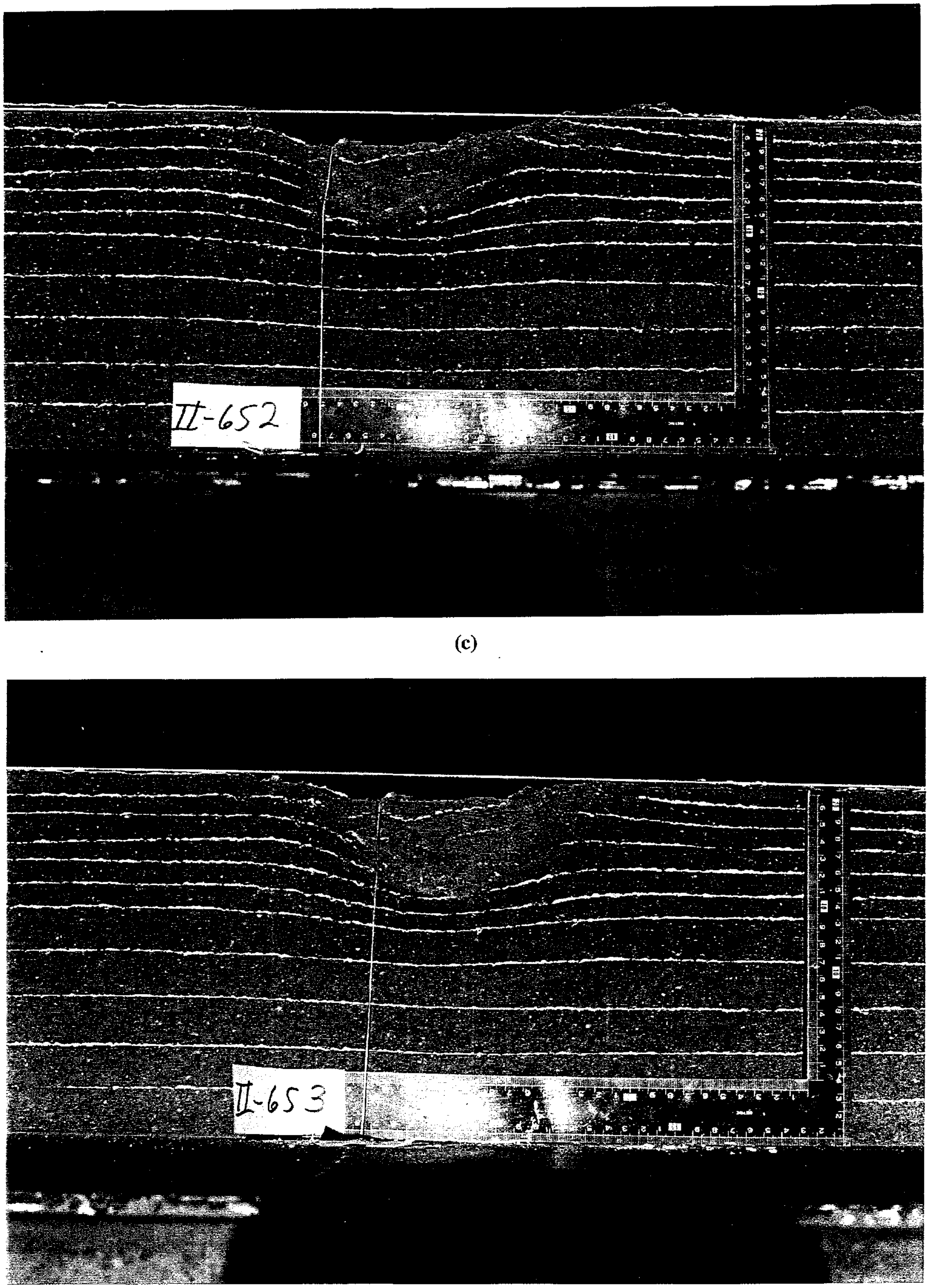

(c)

(d)

FIGURE A7(Cont). Views of Soil Sections for Test #6. (c)Section 2. (d)Section 3.

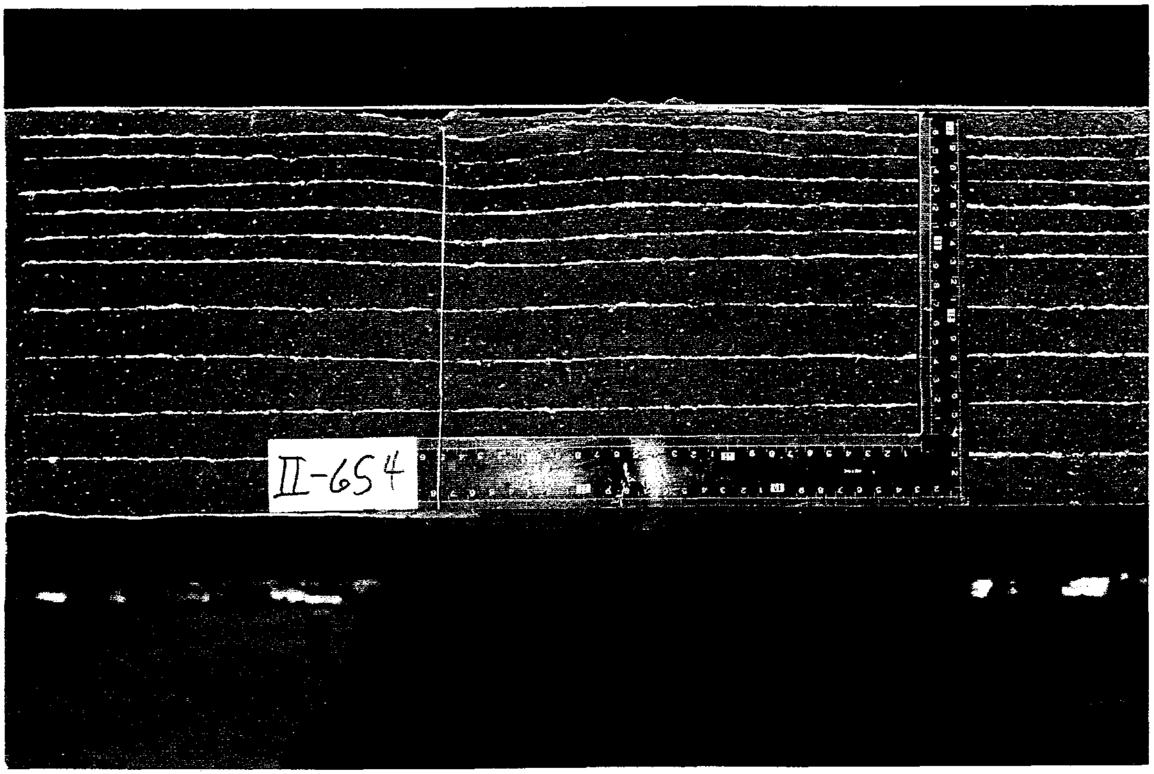

(e)

(f)

FIGURE A7(Cont). Views of Soil Sections for Test #6. (e)Section 4. (f)Section 5.

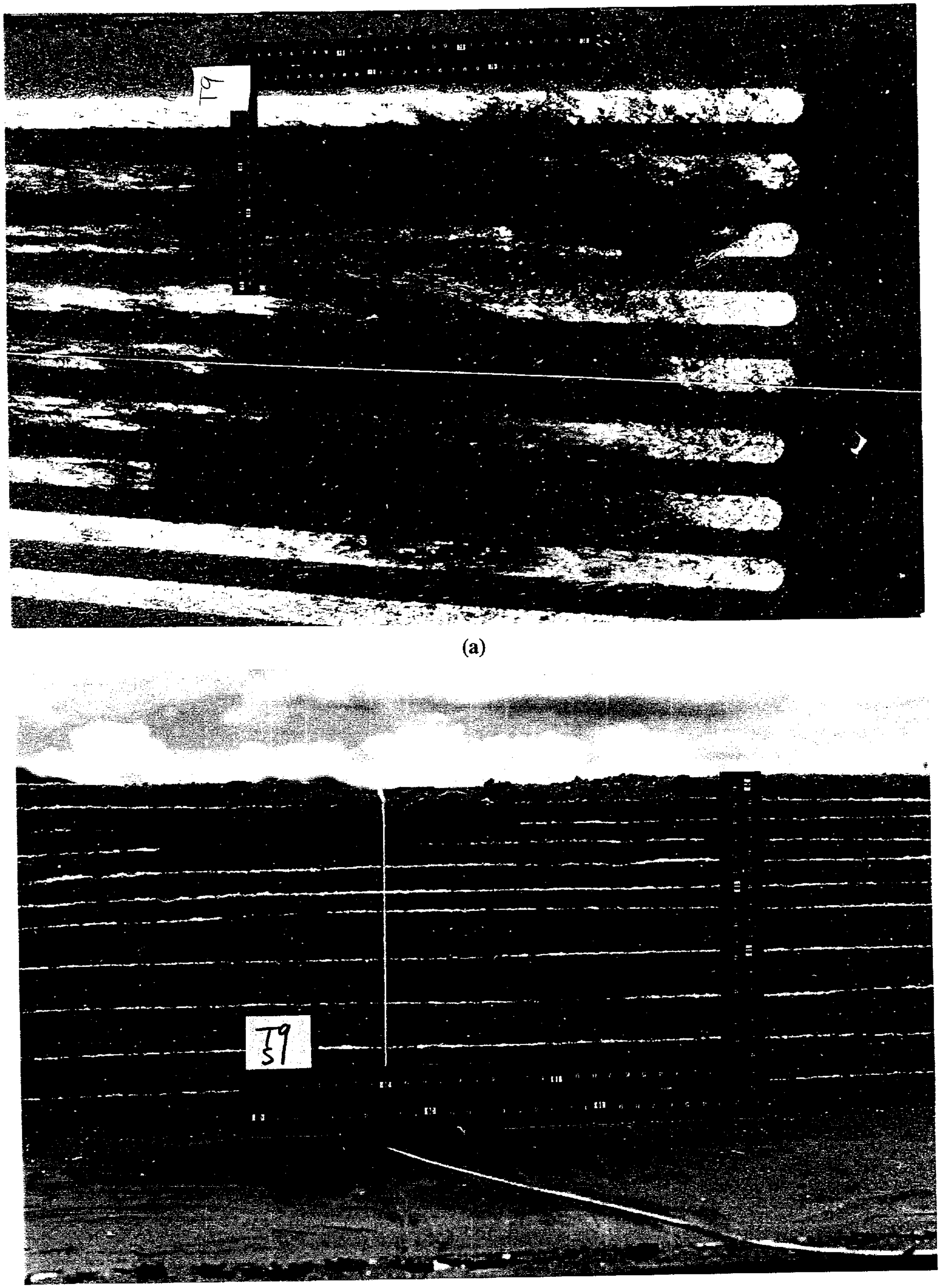

FIGURE A8. Views of Soil Sections for Test #9. (a)Overhead. (b)Section 1.

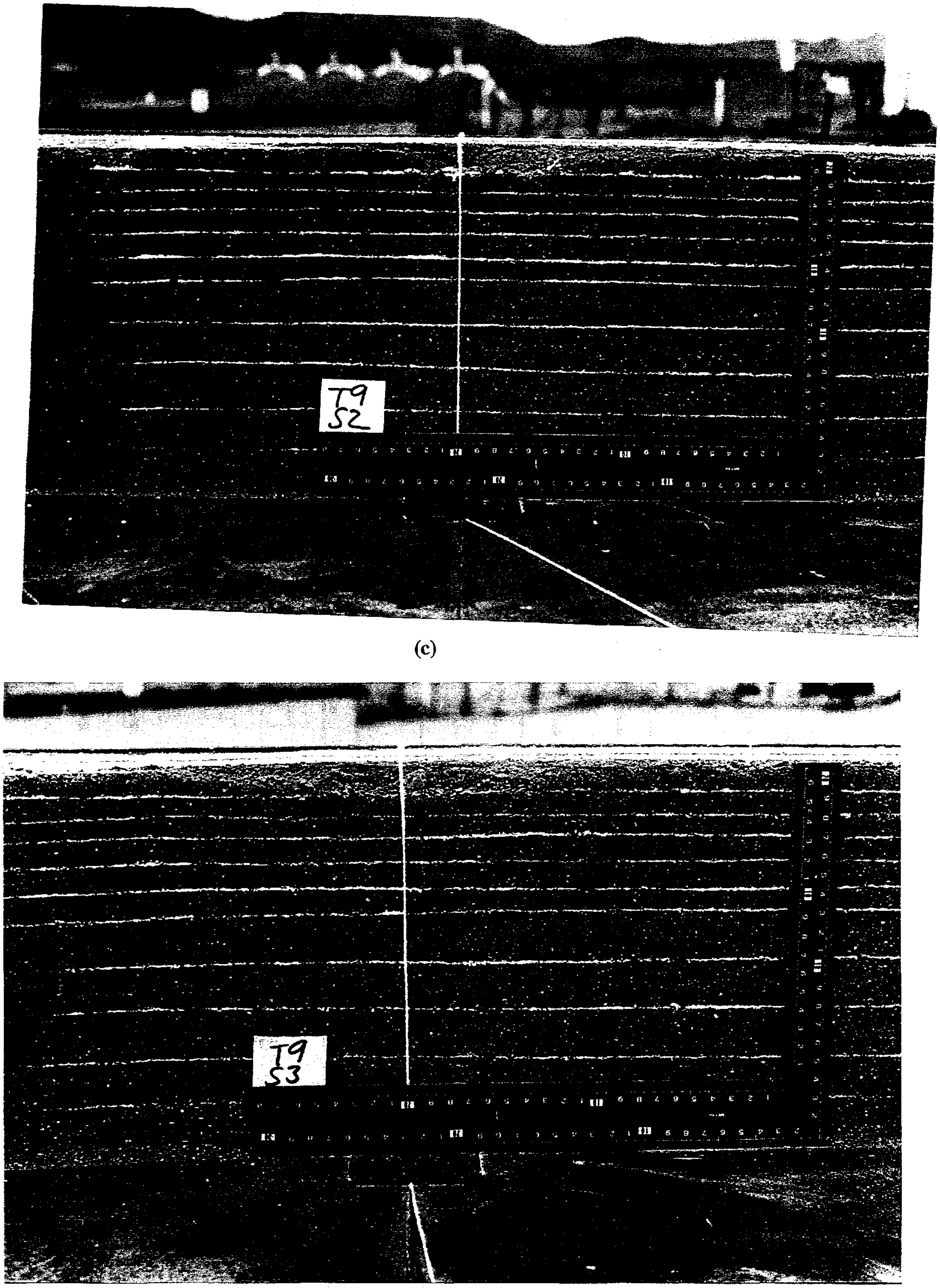

(c)

(d)

FIGURE A8(Cont). Views of Soil Sections for Test #9. (c)Section 2. (d)Section 3.

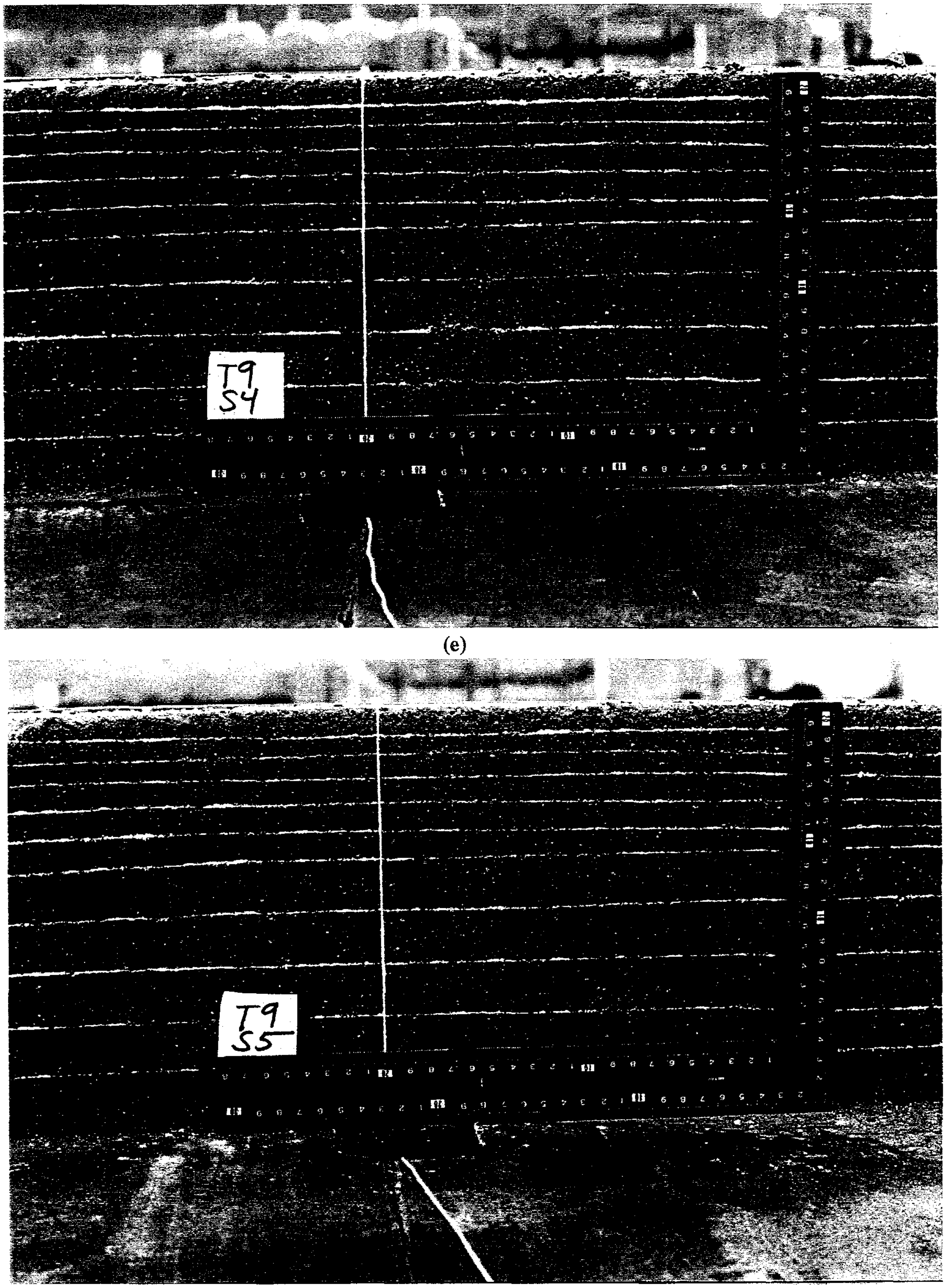

(e)

(f)

FIGURE A8(Cont). Views of Soil Sections for Test #9. (e)Section 4. (f)Section 5.

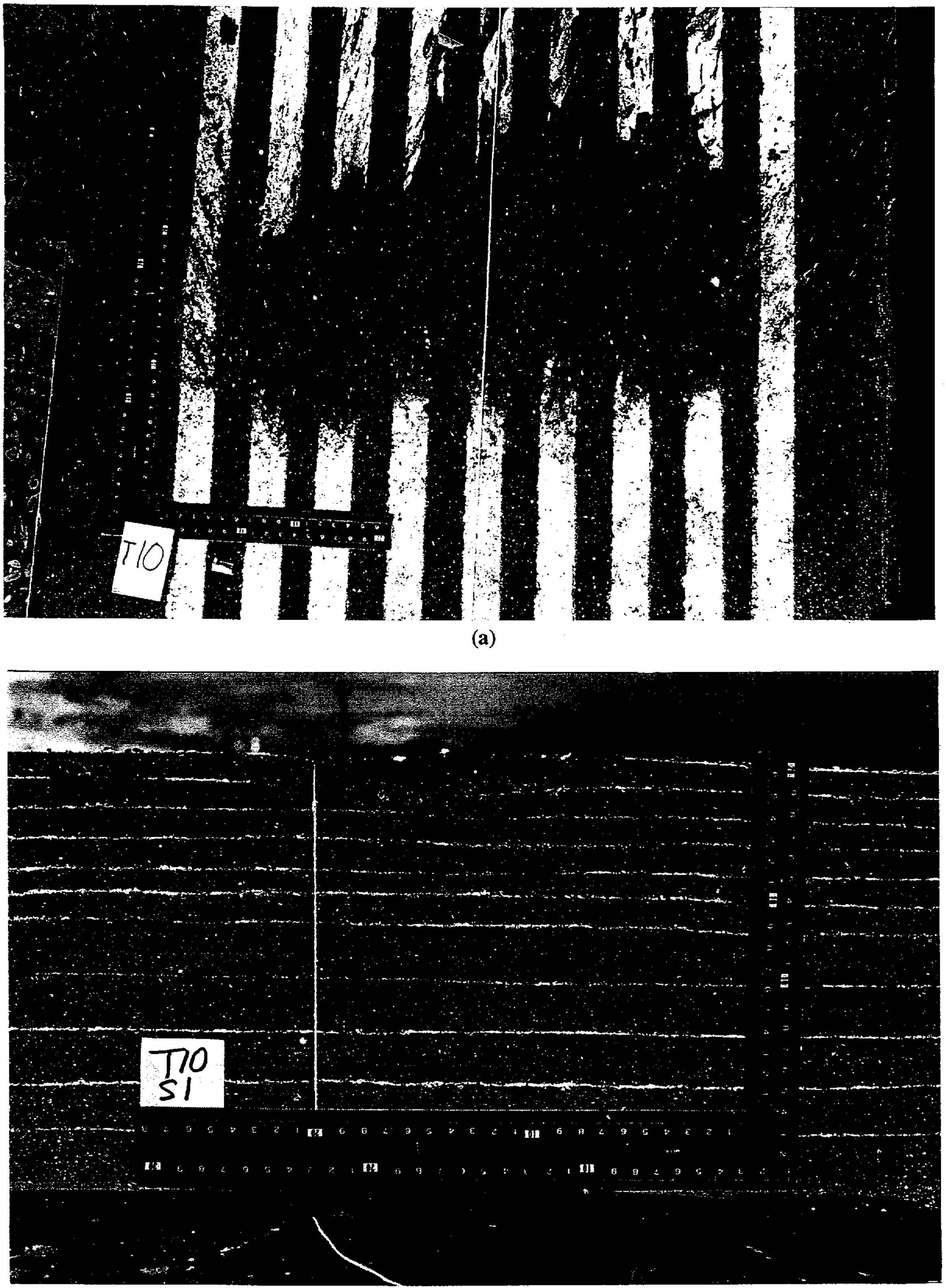

(a)

(b)

FIGURE A9. Views of Soil Sections for Test #10. (a)Overhead. (b)Section 1.

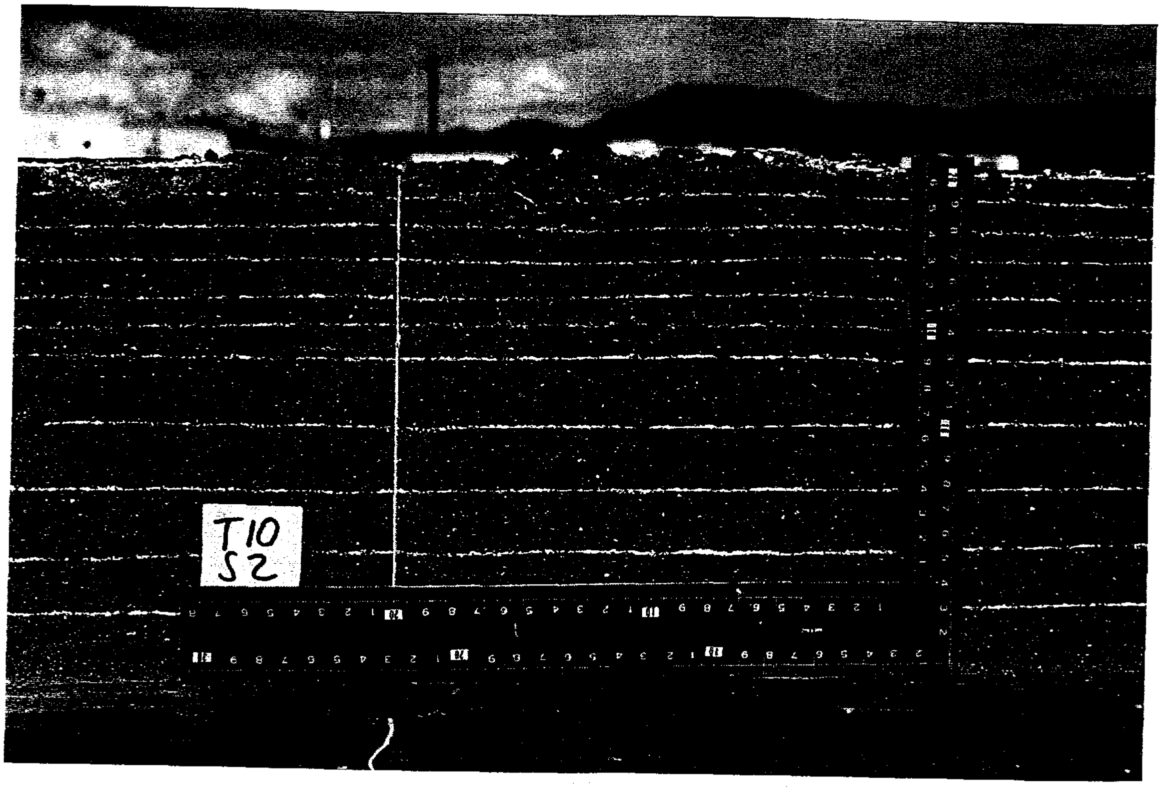

(c)

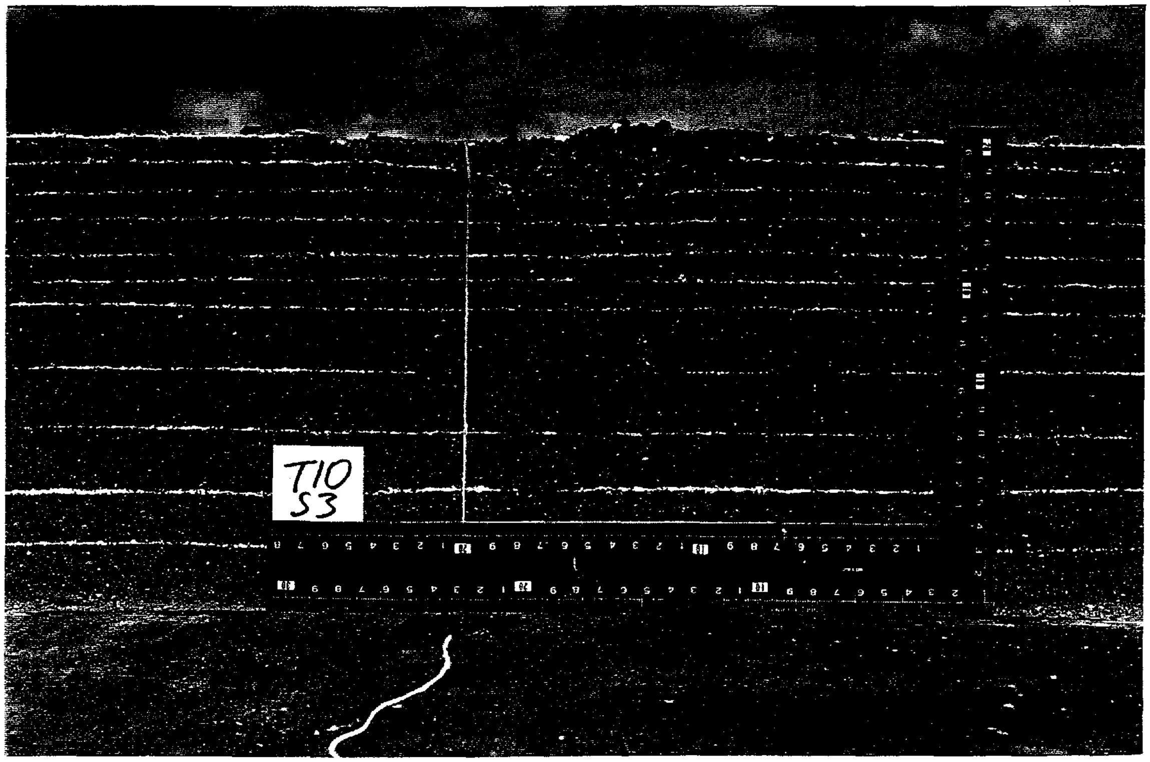

(d)

FIGURE A9(Cont). Views of Soil Sections for Test #10. (c)Section 2. (d)Section 3.

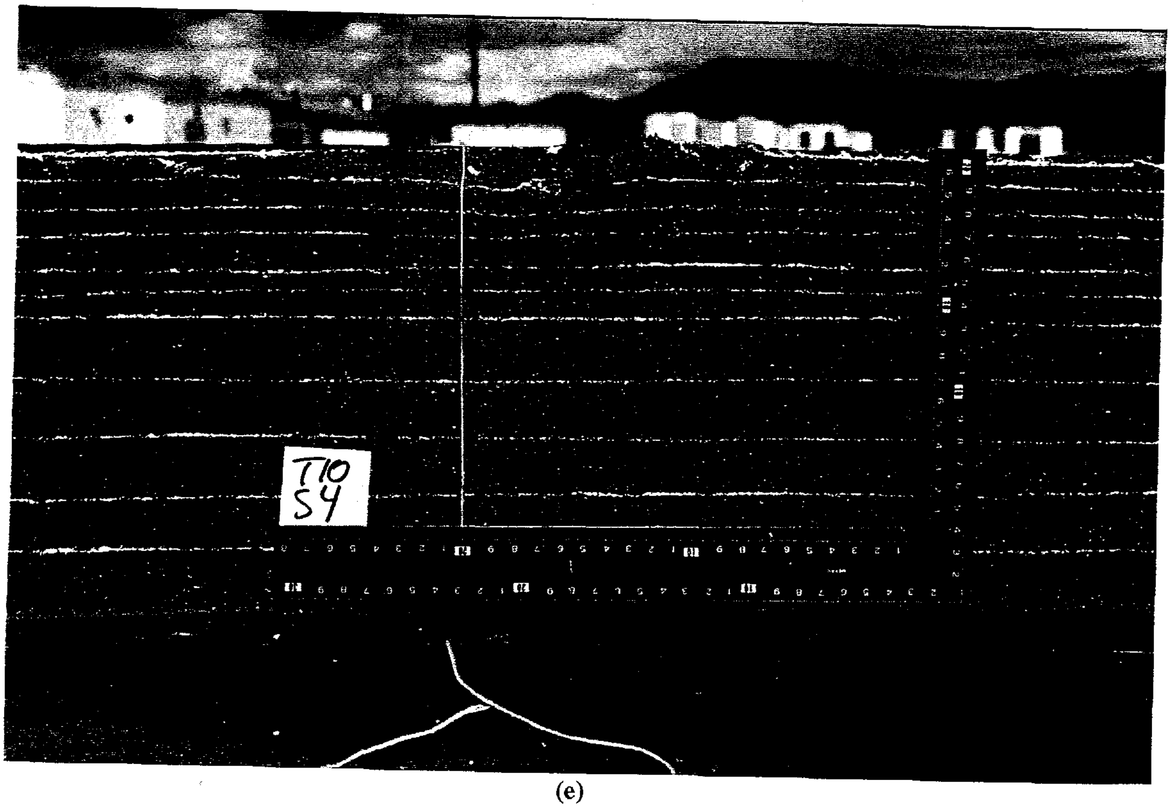

(e)

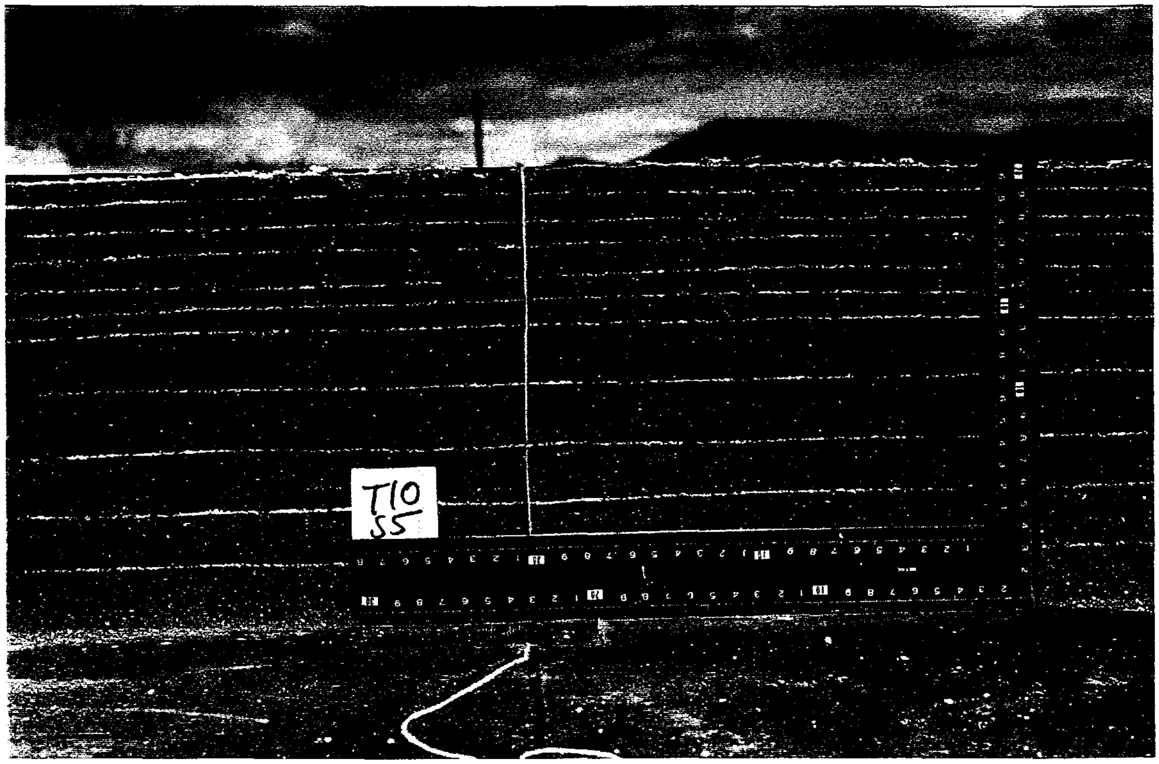

(f)

FIGURE A9(Cont). Views of Soil Sections for Test #10. (e)Section 4. (f)Section 5.

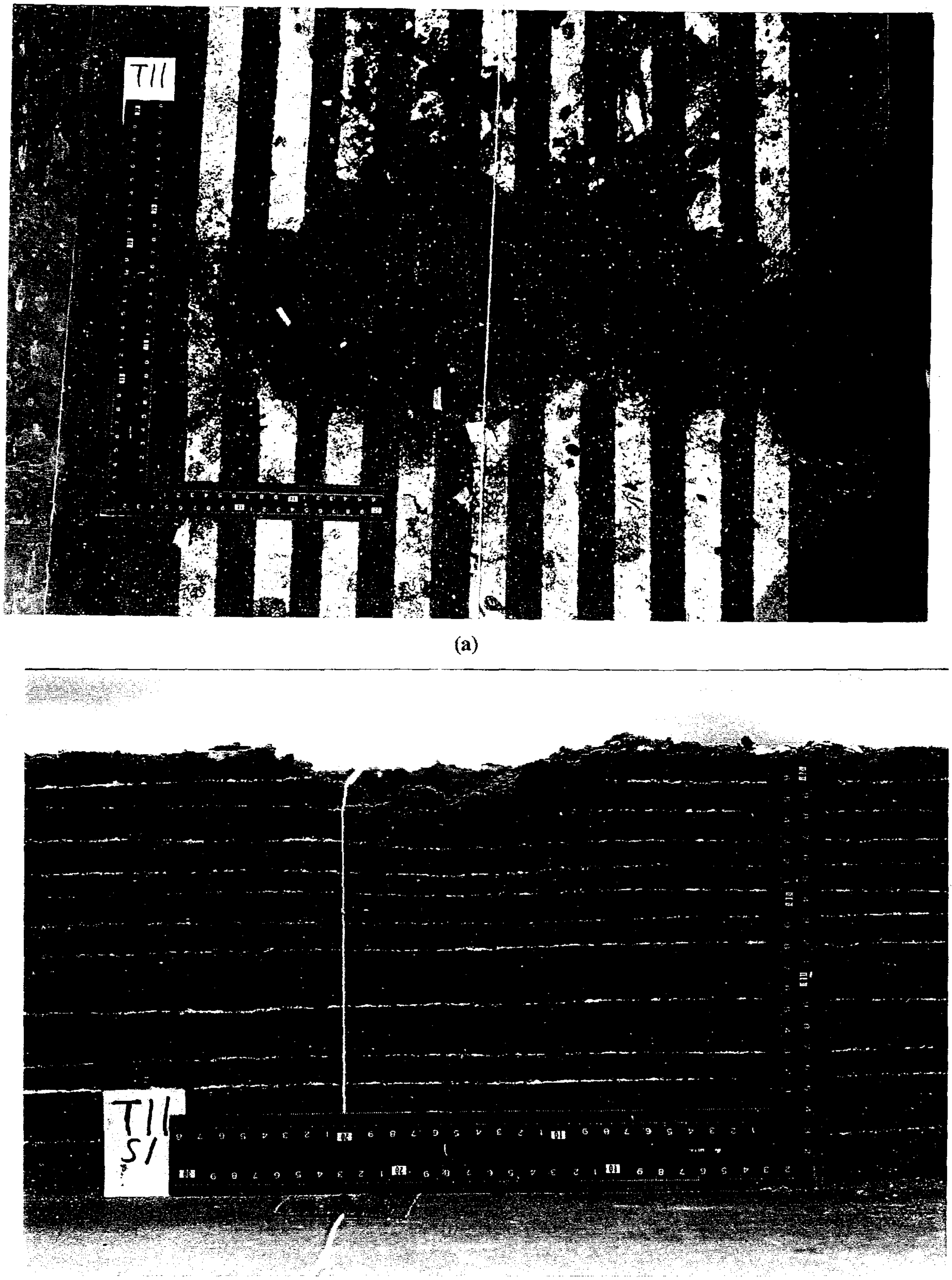

(a)

(b)

FIGURE A10. Views of Soil Sections for Test #11. (a)Overhead. (b)Section 1.

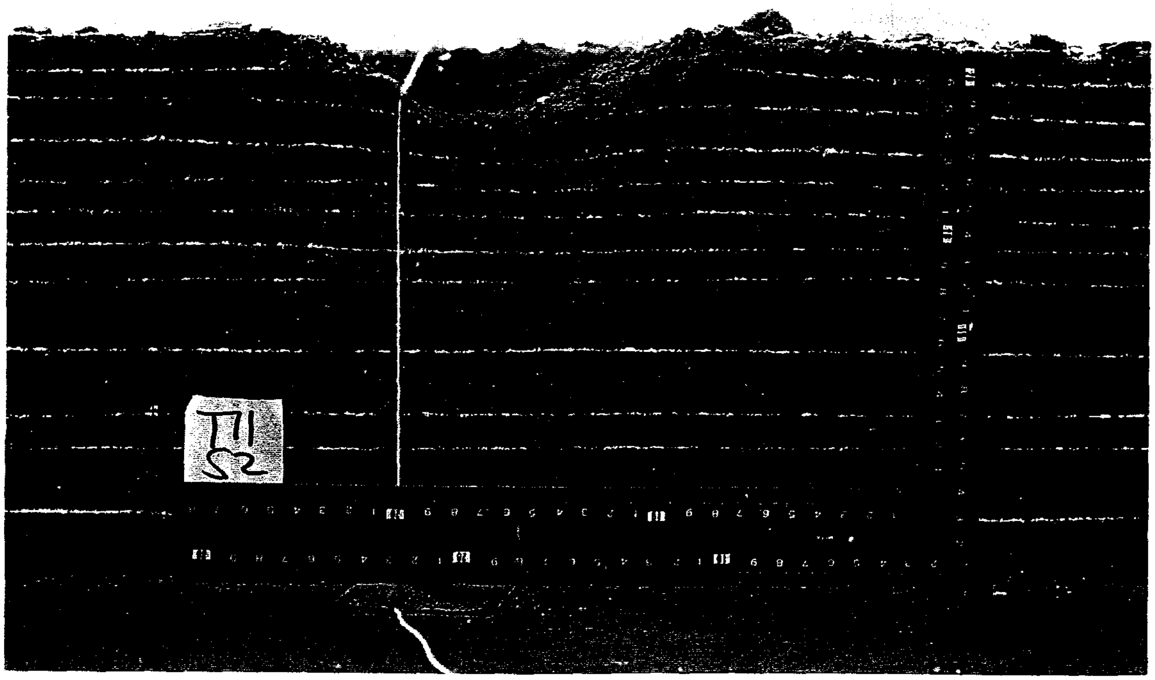

(c)

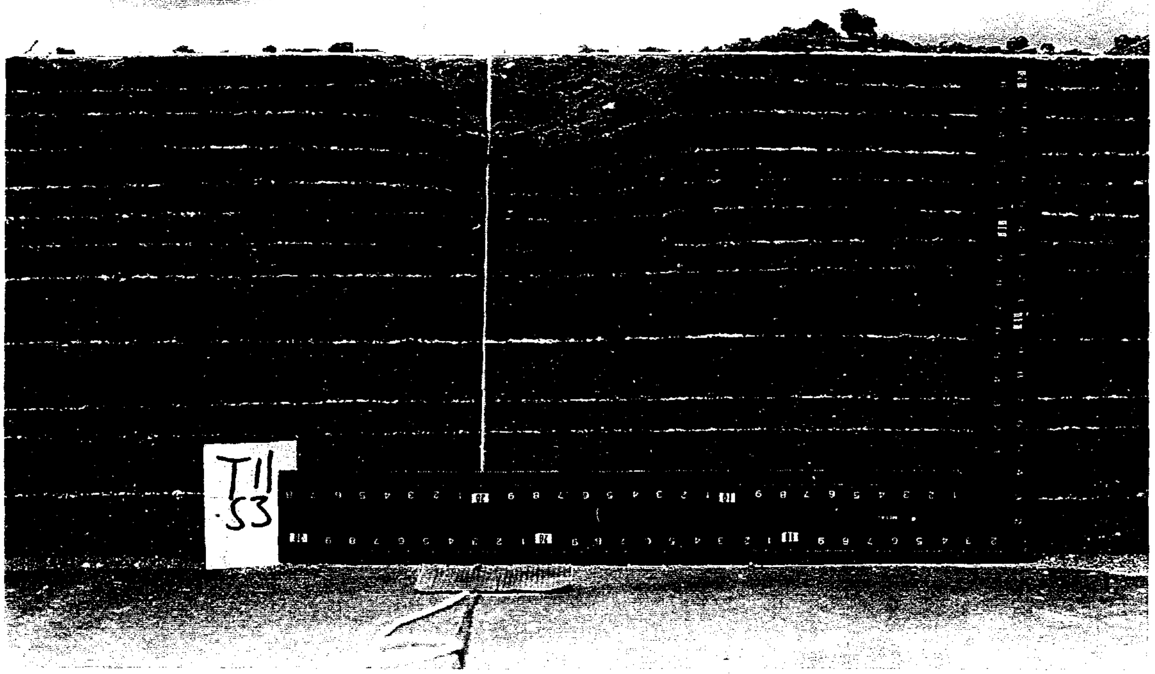

(d)

FIGURE A10(Cont). Views of Soil Sections for Test #11. (c)Section 2. (d)Section 3.

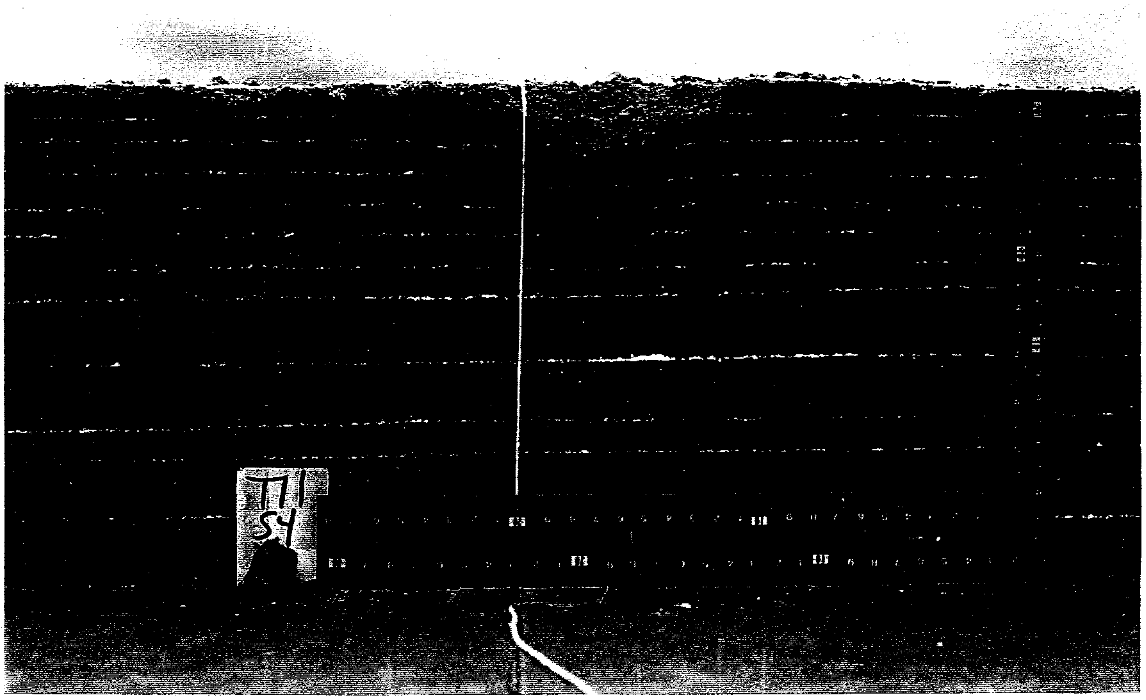

(e)

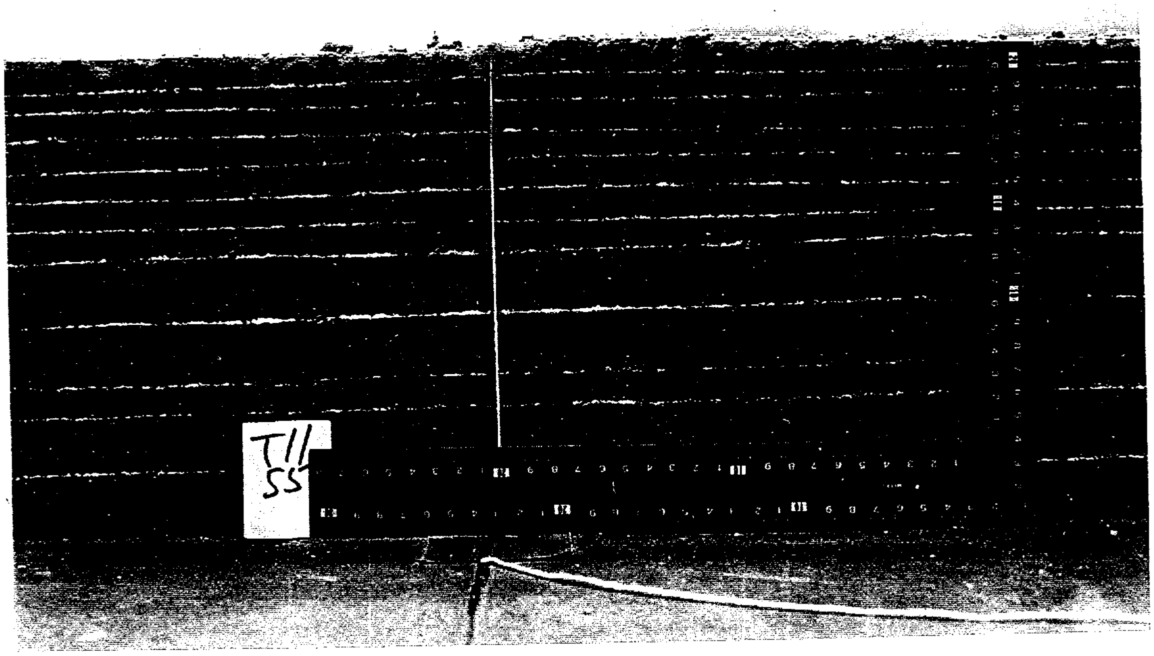

(f)

FIGURE A10(Cont). Views of Soil Sections for Test #11. (e)Section 4. (f)Section 5.

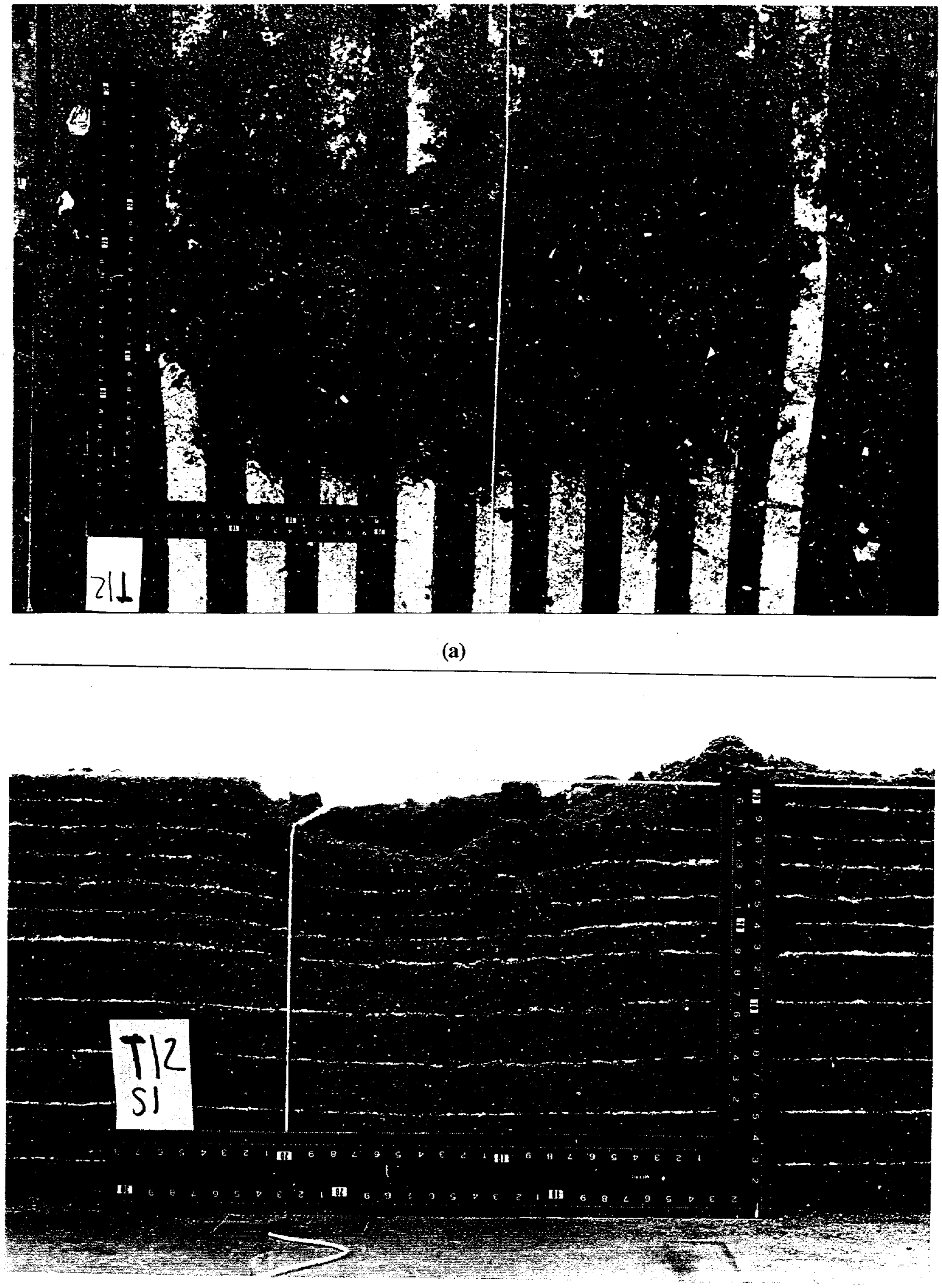

(a)

(b)

FIGURE A11. Views of Soil Sections for Test #12. (a)Overhead. (b)Section 1.

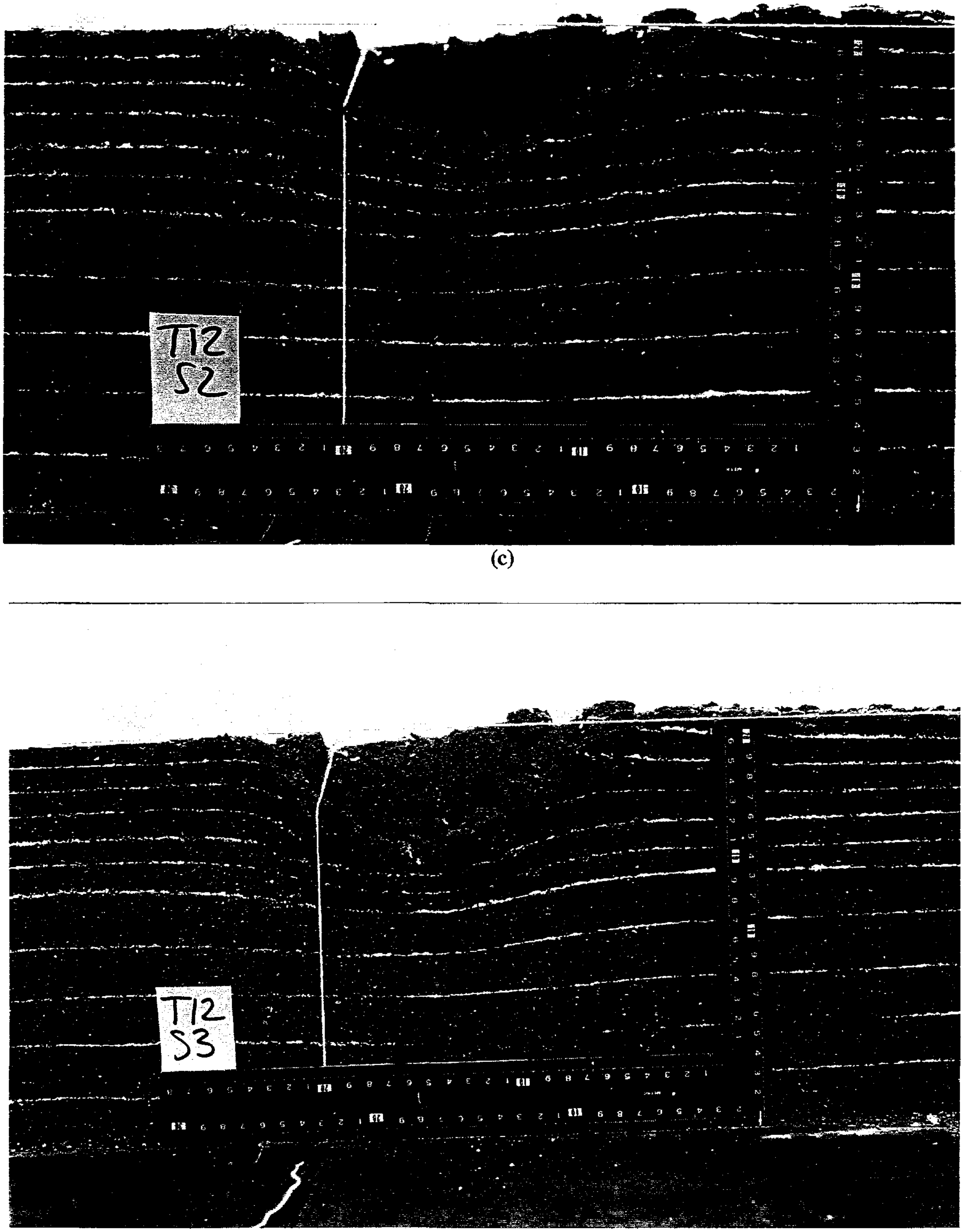

(c)

(d)

FIGURE A11(Cont). Views of Soil Sections for Test #12. (c)Section 2. (d)Section 3.

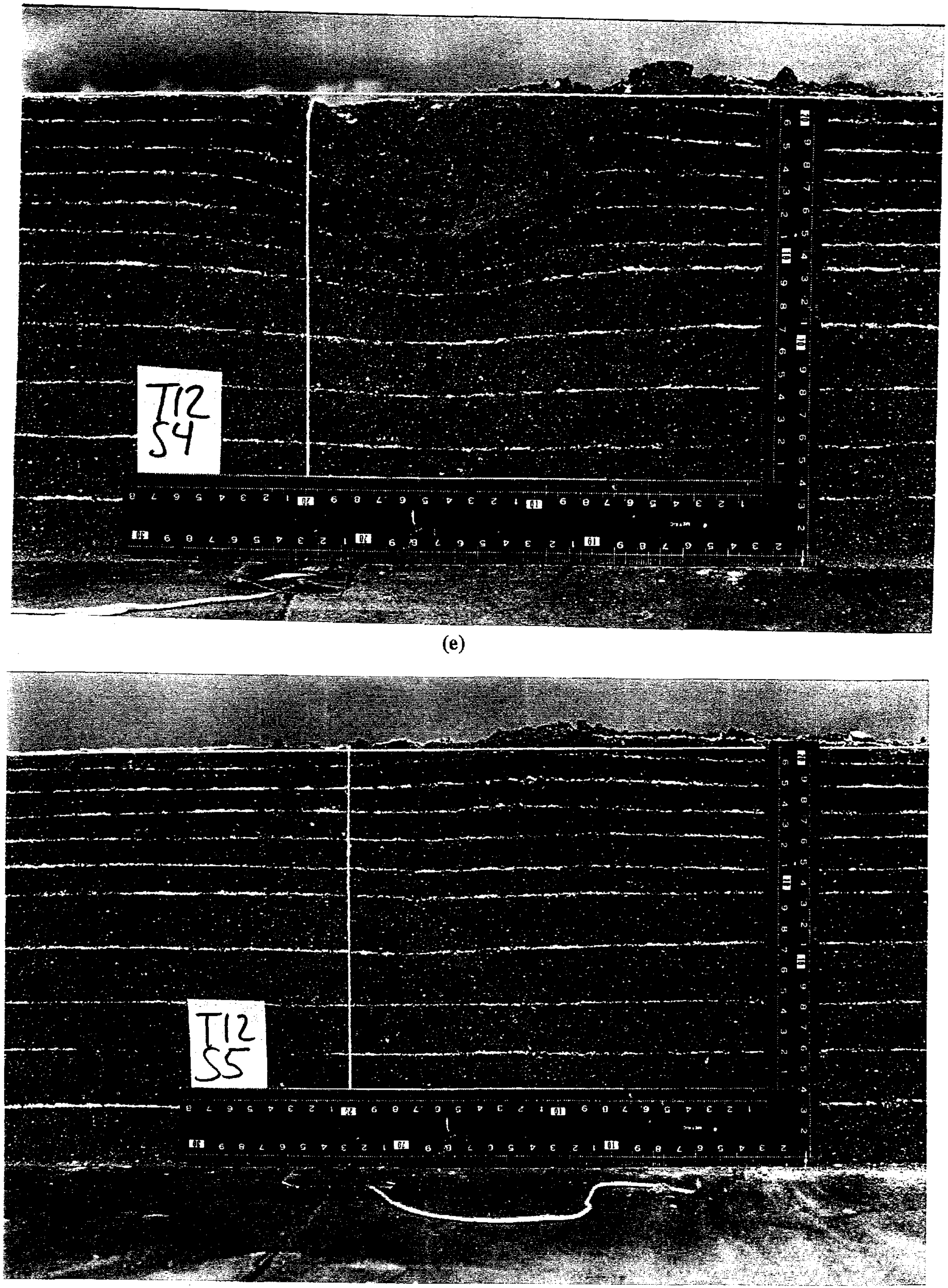

(e)

(f)

FIGURE A11(Cont). Views of Soil Sections for Test #12. (e)Section 4. (f)Section 5.

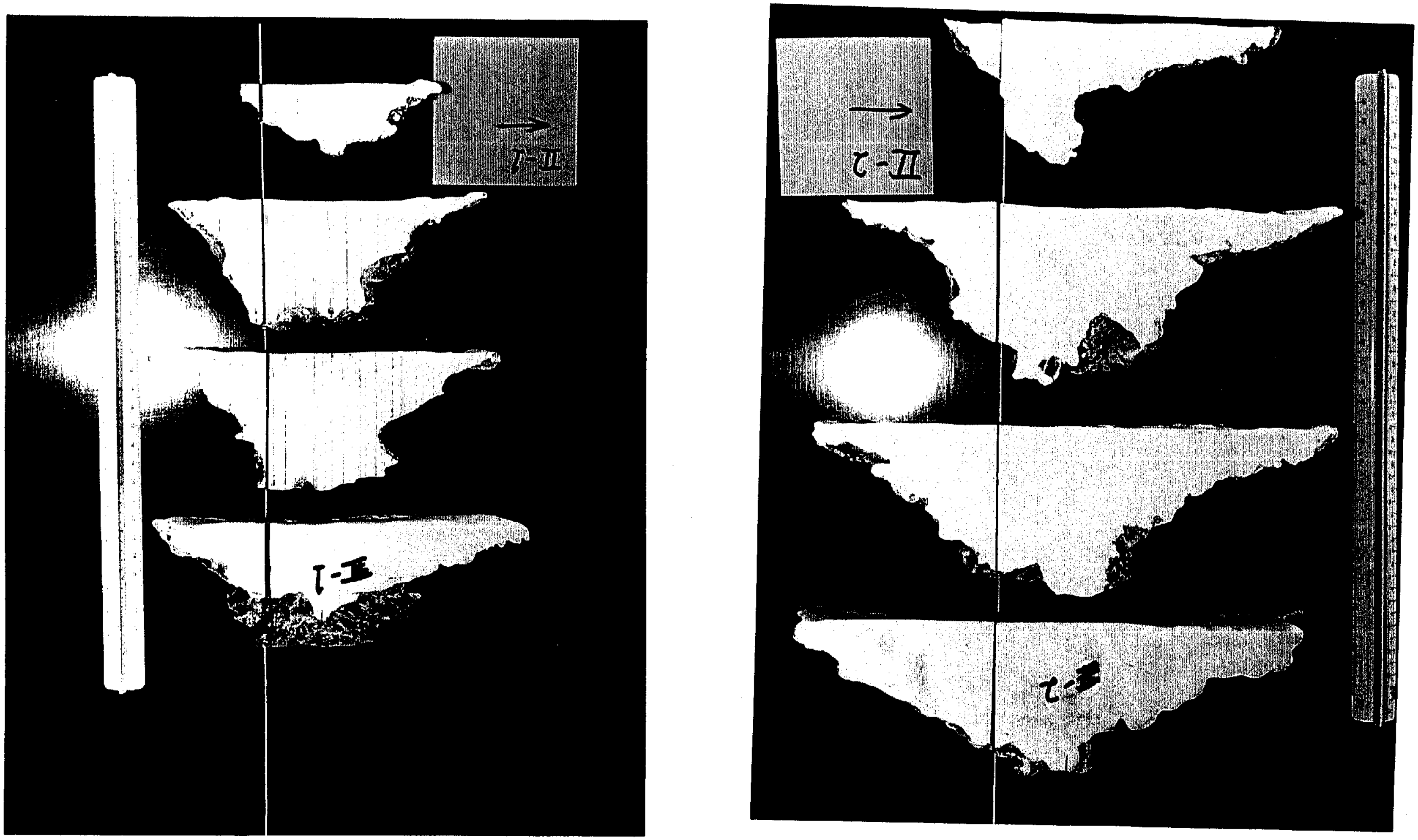

(a)

(b)

FIGURE A12. Crater Cross-sections. (a) Test #1 (b) Test#2

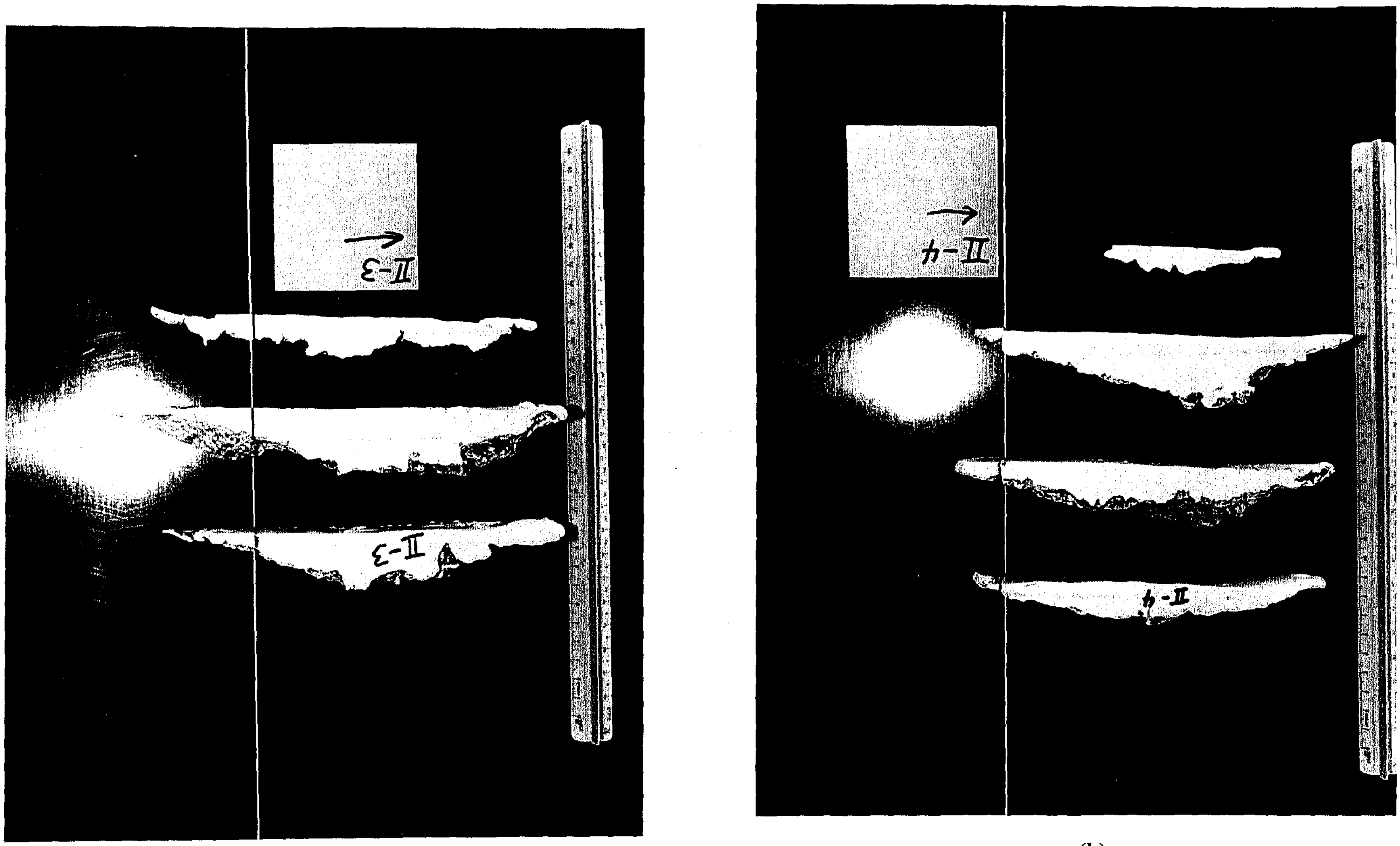

(a) (b)

FIGURE A13. Crater Cross-sections. (a) Test #3 (b) Test#4

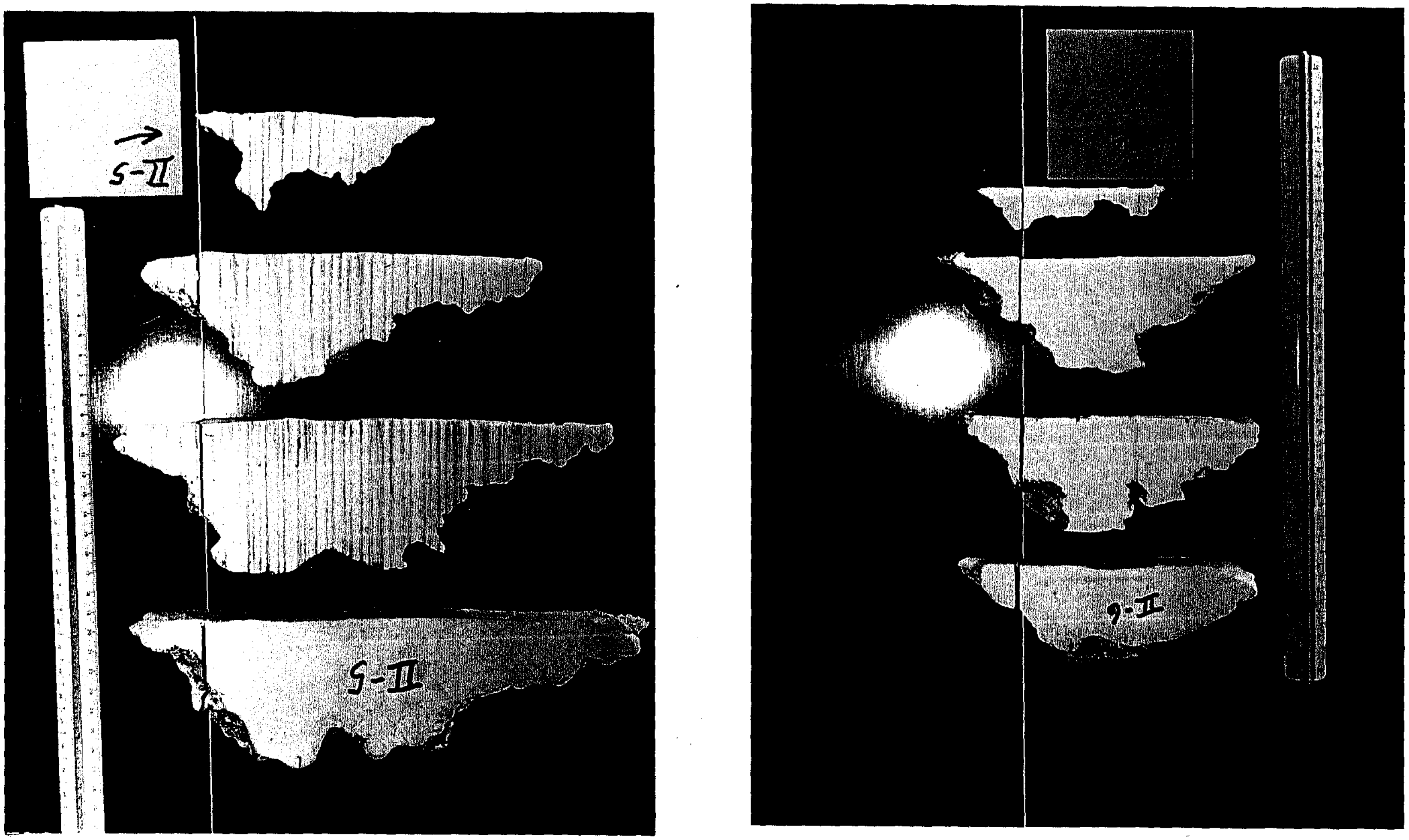

(a)

(b)

FIGURE A14. Crater Cross-sections. (a) Test #5 (b) Test#6

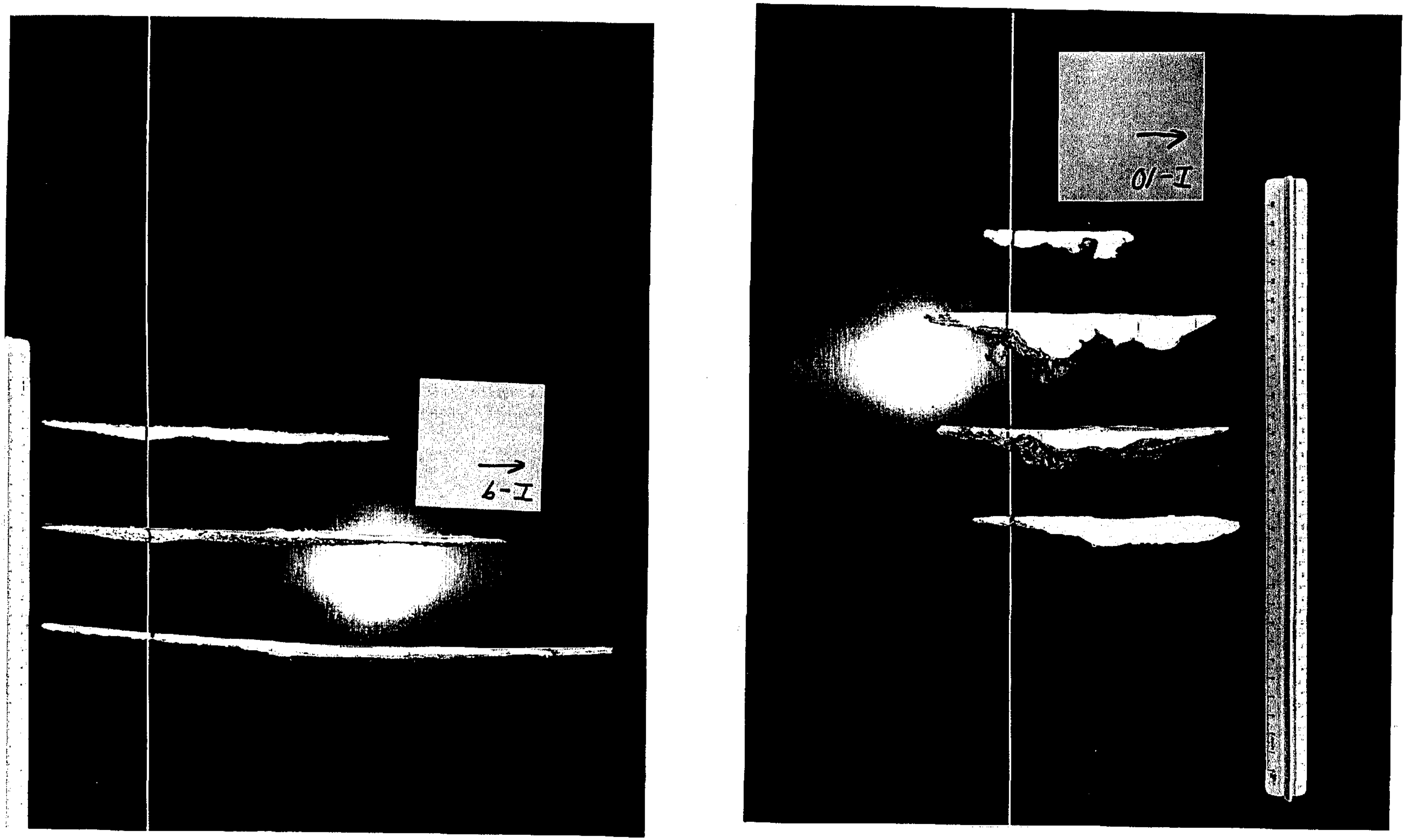

(a) (b)

FIGURE A15. Crater Cross-sections. (a) Test #9 (b) Test#10

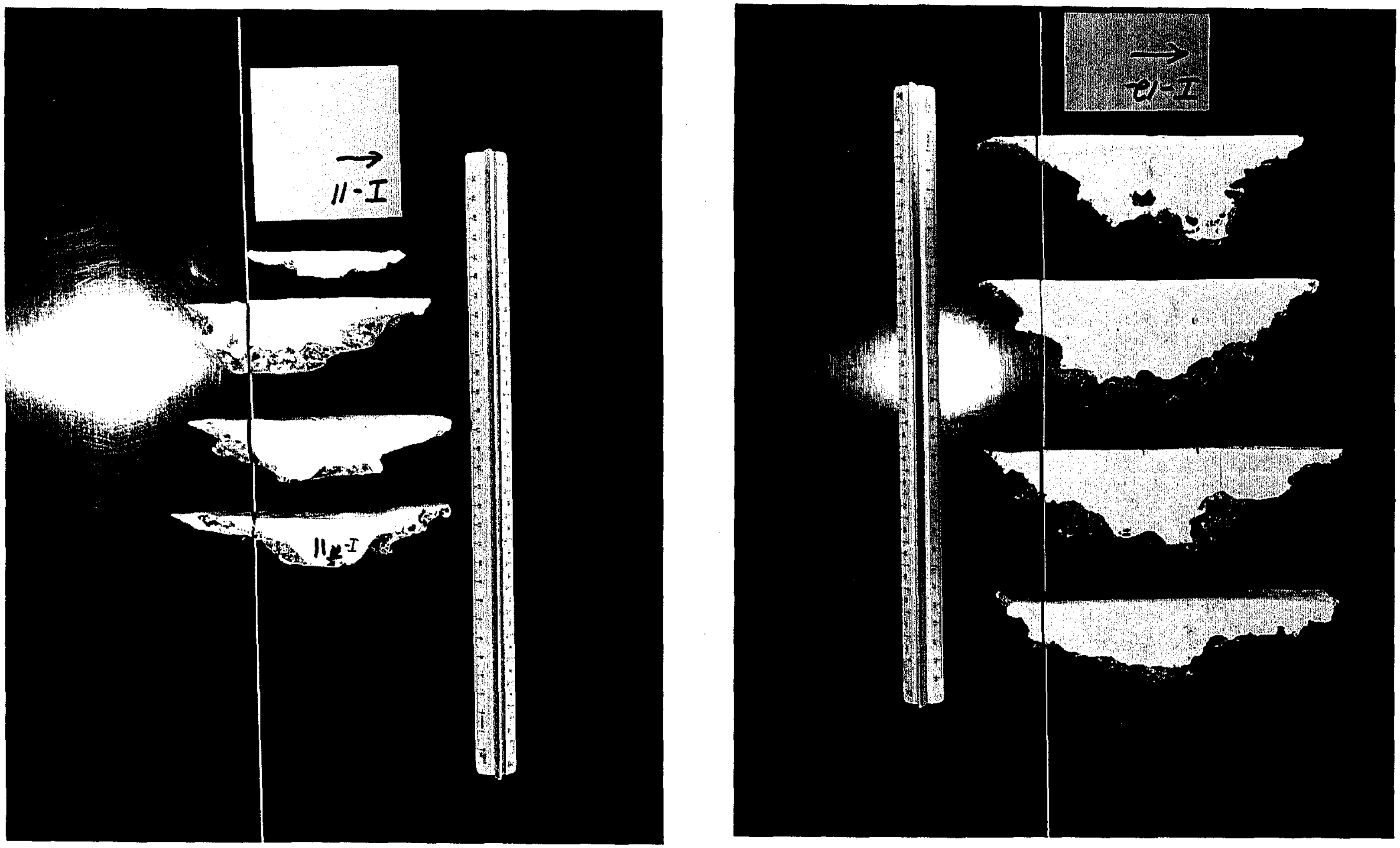

(a)

(b)

FIGURE A16. Crater Cross-sections. (a) Test #11 (b) Test#12

DISTRIBUTION:

1 Boeing Defense and Space Group
Attn: Earl E. Wilhelm
P. O. Box 3707, MS 4C-67
Seattle, WA 98124-2207

1 Director, Defense Nuclear Agency
Attn: CSTI
6801 Telegraph Road
Alexandria, VA 22310-3398

1 Director, Defense Nuclear Agency
Attn: Major Joe Crews
6801 Telegraph Road
Alexandria, VA 22310-3398

1 Director, Defense Nuclear Agency
Attn: LCDR William A. Gott
6801 Telegraph Road
Alexandria, VA 22310-3398

1 Director, Defense Nuclear Agency
Attn: James V. Brackett
6801 Telegraph Road
Alexandria, VA 22310-3398

1 U. S. Department of Energy
Albuquerque Operations Office
Albuquerque Headquarters
Attn: H. T. Season
P. O. Box 5400
Albuquerque, NM 87115

1 U. S. Department of Energy
Albuquerque Operations Office
Albuquerque Headquarters
Attn: R. O. Gergen,
P. O. Box 5400
Albuquerque, NM 87115

1 U. S. Department of Energy
Albuquerque Operations Office
Albuquerque Headquarters
Attn: Roger Cartee
P. O. Box 5400

Albuquerque, NM 87115

1 U. S. Department of Energy
Albuquerque Operations Office
Albuquerque Headquarters
Attn: Karl Rueb
P. O. Box 5400
Albuquerque, NM 87115

1 FAA Technical Center
Attn: Thor Eklund
ADC-250, Building 204
Atlantic City International Airport
Atlantic City, NJ 08405

1 Geo Test, Inc.
Attn: Tim Byres
8904 Washington NE
Albuquerque, NM 87113

1 Kaman Sciences
Attn: Wayne Young
P. O. Box 7463
Colorado Springs, CO 80933

4 Lawrence Livermore National Laboratories
Attn: Doug Stevens
P. O. Box 808, L-85
Livermore, CA 94550

2 Logicon RDA
Attn: Steve Woodford & Art Barondes
6940 South Kings Highway, Suite 210
Alexandria, VA 22310

3 Los Alamos National Laboratories
Attn: Ron Flurry
P. O. Box 1663, MSC931
Los Alamos, NM 87545

1 Los Alamos Technical Associates
Attn: Lou Reidl
2400 Louisiana Blvd. NE
Building 1, Suite 400
Albuquerque, NM 87110

1 NWI
Attn: Col. John Curry, Technical Director
1651 First Street SE
Kirtland AFB, NM 87117

1 NWI
Attn: Dr. Dermod Kelleher, Technical Director
1651 First Street SE
Kirtland AFB, NM 87117

1 NWIE
Attn: Micheal Martinez
1651 First Street SE
Kirtland AFB, NM 87117

1 PLG Inc.
Attn: David Johnson
4590 MacArthur Blvd. Suite 400
Newport Beach, CA 92660

1 TRW Inc.
Attn: Kiran Magiawala
Space and Technology Division, MS R1-1062
One Space Park
Redondo Beach, CA 90278

1 Weidlinger Associates
Attn: H. Levine
4410 El Camino Real, Suite 110
Los Altos, CA 94022

1 Wright Laboratories
Attn: M. Bennett
FIVS Bldg. 63
1901 Tenth Street
Wright Patterson Air Force Base, Ohio 45433-7605

1	MS 0429	W. C. Nickell, 2300
1	MS 0715	C. E. Olson, 6606
1	MS 0828	R. D. Skocypec, 9102
1	MS 0835	Carl Peterson, 9116
10	MS 0835	S. R. Tieszen, 9116
1	MS0835	R. W. Oliver, 9116
1	MS 0437	E. P. Chen, 9118
2	MS 0437	S. W. Attaway, 9118
3	MS 0865	J. L. Moya, 9735

1	MS 0492	P. E. D'Antonio, 12324
1	MS 0492	G. A. Sanders, 12332
1	MS 0405	D. D. Carlson, 12333
1	MS 0405	M. K. Fuentes, 12333
1	MS 0405	T. R. Jones, 12333

1	MS 9018	Central Technical Files, 8523-2
5	MS 0899	Technical Library, 4414
1	MS 0619	Print Media, 12615
2	MS 0100	Document Processing, 7613-2 For DOE/OSTI

Org.	Bldg.	Name	Rec'd by	Org.	Bldg.	Name	Rec'd by

Sandia National Laboratories